Vibration Damping of Coiled Structures Through Frictional Slip

Thesis by
Alexander Wen

In Partial Fulfillment of the Requirements for the
Degree of
Doctor of Philosophy

Caltech

CALIFORNIA INSTITUTE OF TECHNOLOGY
Pasadena, California

2024
Defended March 25, 2024

© 2024

Alexander Wen
ORCID: 0009-0008-9038-3039

ACKNOWLEDGEMENTS

In addition, I want to highlight the GALCIT staff, in particular: Petros Arakleian, Liza Bradulina, Kate Jackson, Ali Kiani, Brandon Nilles, Paula Mark, Jamie Meighen-Sei, Christine Ramirez. These are the people who support the department and make everything we do here possible.

I'd also like to thank my friends and colleagues at Caltech. Notably, the cohort I came into Caltech with who helped me survive the 1st year and beyond. And also, all past and present members of the Space Structures Lab for their innumerable contributions and support, from words of encouragement to helpful discussions and feedback both inside and outside the lab: Brayden Aller, Federico Benazzo, Dr. Gianfranco Canales, Meital Carmi, Dr. Luke Chen, Sahangi Dassanayake, Dr. Charles Dorn, Dr. Serena Ferraro, Dr. Terry Gdoutos, Dr. Armanj Hasanyan, Dr. Wilfried Jahn, Maria Kechri, Dr. Christophe Leclerc, Dr. Andrew Lee, Dr. Yang Li, Dr. Wen Luo, Dr. Michael Marshall, John Pederson, Dr. Antonio Pedivellano, George Popov, Dr. Harsha Reddy, Dr. Fabien Royer, Dr. Maria Sakovsky, Dr. Daniel Scharf, Charles Sommer, Divesh Soni, Dr. Jaden Suh, Dr. Thibaud Talon, Alan Truong, Dr. Kanthasamy Ubamanyu, Dr. Yuchen Wei. Sergio has a talent for finding and building a team of remarkable individuals who are not only great to work with but also continue to foster an enduring lab culture that I am honored to be a part of.

Specific recognition goes to the DOLCE team, which was part of a collaboration that last year successfully completed what I believe to be Caltech's first space mission entirely designed, built, and operated solely by the university.

I'd also like to acknowledge my friends from various other places: particularly from undergrad at Berkeley as well as my old coworkers at Planet. As the years pass, I am increasingly appreciative that the lasting friendships and connections fostered in previous stages of my life are something special to be cherished. It's always been difficult for me to say there's one exact reason for wanting to do go back to do a Ph.D, but definitely a major part of it was being inspired and supported by these people

And finally I'd like to thank my family: my four siblings, my new brother in law, and my parents, who have supported me not only during my Ph.D, but for my entire life. Their encouragement and understanding have always been the cornerstone of my journey. And finally, a special shoutout to my older sister Jessica, who played a major role in making this possible by convincing me to apply to Caltech when I never thought I would be accepted.

ABSTRACT

Vibration management is important for the survivability of structures. The response of a structure under vibration is dependent upon interaction between the excitation environment and the properties of the structure. If the input excitation cannot be adjusted, then the structure must be engineered to survive. One approach to engineering structures to reduce vibration response is through damping, which is achieved by adding damping devices or materials to covert kinetic energy into heat, where removing energy from the system reduces the amplitude of response. There are a variety of existing vibration damping concepts and techniques, however, conventional methods of these approaches are subject to limitations such as compromising stiffness for increased damping and performance that is excitation profile dependent.

This research proposes a novel, passive vibration damping concept which is motivated by recent deployable structures for space that use coiling as a packaging architecture. The proposed concept, referred to as *wound roll damping*, is a friction-based damping scheme for coiled structures, where the structure is wound around a mandrel with tension that allows interlayer slip during vibration. The friction between slipping layers provides an energy dissipation mechanism, which reduces the overall level of response. The concept was developed with the challenges of mitigating spacecraft launch vibration and the limitations of conventional damping techniques in mind.

Understanding of the working principle and performance of this damping concept is achieved using a combination of experiments, analysis, and FEA. A method for determining the locations of slip within a wound roll under vibration is presented. This consists of modeling the interlayer friction forces, using analytical expressions for the stress fields that arise during tension winding of wound rolls, and comparing these values against loading estimates obtained from analysis and FEA. The locations of slip for wound rolls supported by a cantilevered mandrel with bending vibration modes are towards the root of the wound roll structure, near the inner layers.

Experimental studies that demonstrate the performance and properties of this damping concept are presented in this work. A wound roll test sample is subjected to a range of excitation profiles including: sine sweep, sine dwell, random, and shock with varying levels of sample winding tension and excitation amplitude. Using

these experiments, this concept is demonstrated to not be subject to the limitations of conventional damping schemes. This scheme is observed to be capable of significantly increasing the overall stiffness while providing elevated damping levels, with a performance that is tunable with winding tension, independent of excitation profile, and scales with excitation amplitude. The locations of slip are observed to be consistent with predictions from FEA and analysis.

Two approaches to simulate and model the wound roll damper are developed to both better understand the physical mechanism of this concept and provide analysis tools. The first method is an FEA model, consisting of the base vibration of concentric shells and solids that have frictional contact interactions. The second method is a 2-DoF reduced order model that simulates the frictional contact between two mass-spring-damper systems. Both methods are demonstrated to have good correlation with experimental measurements.

A majority of this work demonstrates the performance of this concept, using both experiments and simulation at lab scales. This work also presents simulation studies that demonstrate the viability of this concept at realistic scales. Using simulations scaled to recent coilable space structures, both implemented and proposed, the wound roll damping concept is demonstrated to provide significant stiffness and damping.

PUBLISHED CONTENT AND CONTRIBUTIONS

[1]   A. Wen and S. Pellegrino. "Performance and Scaling Metrics for Launch Vibration of Coiled Space Structures with Embedded Friction Damping". In: Jan. 2024. DOI: `10.2514/6.2024-2438`. URL: `https://arc.aiaa.org/doi/abs/10.2514/6.2024-2438`.
A.W. developed and performed all experimental and simulation work, and wrote the manuscript.

[2]   A. Wen and S. Pellegrino. "Launch Vibration Damping Using Slip in Pre-tensioned Coils". In: AIAA SCITECH 2023 Forum. 2023. URL: `https://arc.aiaa.org/doi/abs/10.2514/6.2023-2066`.
A.W. developed and performed all experimental and simulation work, and wrote the manuscript.

[3]   A. Wen and S. Pellegrino. "Launch Vibration of Pre-Tensioned Coiled Structures". In: 2022. DOI: `10.2514/6.2022-1883`. URL: `https://arc.aiaa.org/doi/abs/10.2514/6.2022-1883`.
A.W. developed and performed all experimental and simulation work, and wrote the manuscript.

TABLE OF CONTENTS

LIST OF ILLUSTRATIONS

LIST OF TABLES

Chapter 1

INTRODUCTION

1.1 Importance of Vibration Mitigation: Case Studies of Engineering Failures and Disasters

Vibration management is crucial for the survival and longevity of structures. Neglecting this aspect can have severe ramifications, as evidenced by several infamous engineering failures across a wide spectrum of applications, ranging from terrestrial structures to aerospace systems (Fig. 1.1). Vibration induced failures can manifest in various ways. The loading spectrum can contain frequencies that excite a resonant mode of the structure, or structure-environment interactions can result in self-oscillation. These conditions can lead to dynamic amplification, where the structure's response exceeds material limits (Fig. 1.1a). Even in cases where the instantaneous failure limit is not reached, repetitive motion can induce vibration fatigue (Fig. 1.1b), local contact welding or wear (Fig. 1.1c), or unexpected system interactions, which can confuse sensors and inadvertently trigger unintended states (Fig. 1.1d, Fig. 1.1e). These examples underscore the critical significance of effectively managing the interaction between structures and their loading environments. If the loading conditions cannot be reduced or adjusted, the structure needs to be engineered to survive by mitigating the vibration response.

1.2 Vibration Mitigation Approaches

There are two primary approaches for designing structures to reduce vibration response. The result of each approach can be demonstrated using the transmissibility of a 1-DoF mass-spring-damper (m, k, ζ) system, as shown in Fig. 1.2.

The first approach involves modifying the structure's stiffness with the goal of moving the system response away from forcing. With the stiffness modification approach, vibration response reduction can be achieved by either stiffness reduction or by stiffness increase (Fig. 1.2a). A common technique that employs the stiffness reduction technique is base isolation, where the system stiffness is intentionally reduced to shift the resonant frequency lower, resulting in attenuation at frequencies higher than the new resonant frequency.

Alternatively, increasing stiffness reduces deformation under a given load, thereby

(a) Tacoma Narrows Bridge: wind-induced self oscillation amplified until supporting cables failed, resulting in bridge collapse [1–3].

(b) Kegworth Air Disaster: untested engine upgrade resulted in high vibrations, leading to fatigue fracture of turbine fan blades and engine failure [4].

(c) Galileo Orbiter: lubricants worn away during transport vibration resulted in antenna deployment failure [5].

(d) Mars Polar Lander: vibrations during descent triggered touchdown sensor, causing premature landing thruster shutdown and loss of lander [6].

(e) ISRO Small Satellite Launch Vehicle D1: vibrations during stage separation triggered safe mode, preventing rocket from reaching intended orbit [7].

Figure 1.1: Notable engineering failures and disasters due to vibration issues.
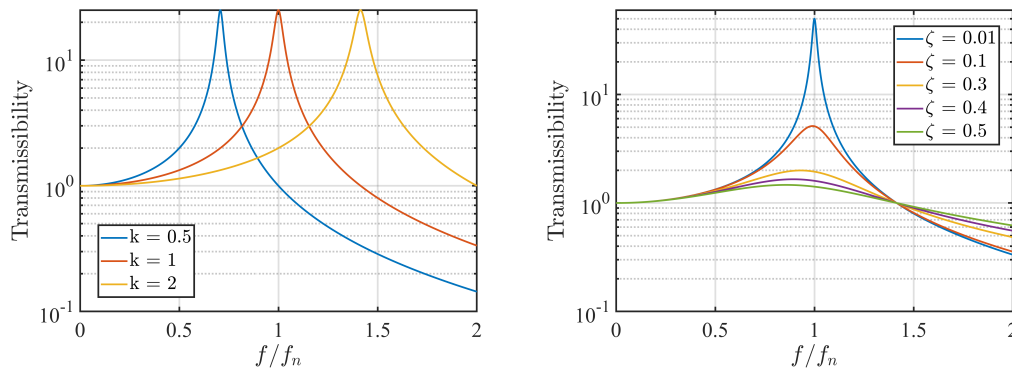
(a) Stiffness modification approach to vibration mitigation: resonant frequency shifts. $(m, k, \zeta) = (1, k, 0.02)$

(b) Damping approach to vibration mitigation: resonant amplitude reduction. $(m, k, \zeta) = (1, 1, \zeta)$

Figure 1.2: Vibration mitigation approaches demonstrated on 1-DoF mass-spring-damper system.

increasing the resonant frequency, where the vibration response tends towards no amplification for frequencies below the new resonant frequency. This can be achieved by utilizing more rigid materials or by changing the geometry to increase the second moment of area.

The second approach is through adding damping, where movement is allowed, and kinetic energy is converted into heat through dissipation mechanisms such as anelastic deformation, viscous dissipation, or friction. Removing energy from the system reduces the amplitude of response (Fig. 1.2b). In general, this is achieved by incorporating damping devices or materials to the original structure to enhance survivability.

1.3 Challenges Posed by Space Environment for Vibration Mitigation

This work studies vibration mitigation motivated by the challenge of vibration management, which is particularly relevant for deployable spacecraft structures. Presently, rockets stand as the sole means for launching large payloads into space and, as a consequence, every spacecraft must contend with the excitation loading inherent to rocket launches. The dynamic loading experienced by a payload during launch and flight originates from a variety of sources, each presenting a range of spectra and degrees of severity. These sources include the unsteady combustion of the engine(s), turbulent atmospheric interactions along the rocket body or arising from exhaust gases, and shocks induced by explosive devices during stage separation (Fig. 1.3) [8, 9]. Previous studies estimated that launch vibration accounts for up to

60% of first-day space failures [10].
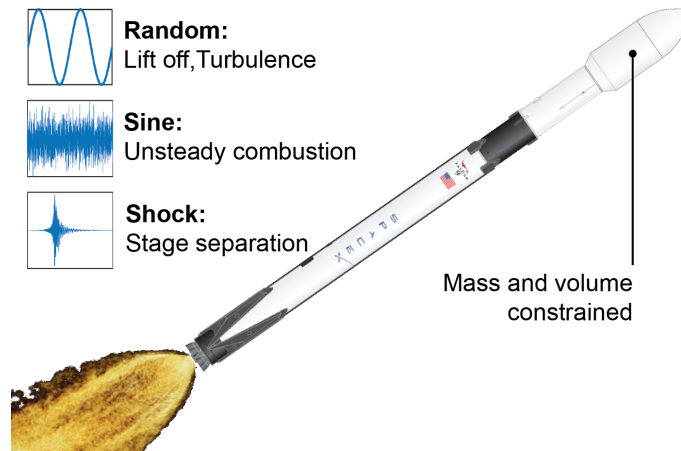
Figure 1.3: Sources and spectra of vibration during launch (Credit: SpaceX).

Rockets not only provide the source of excitation but also impose additional constraints to the problem-solving approach of reducing vibration response. The finite dimensions of rocket fairings imposes volumetric limitations on payload size (Fig. 1.3). Moreover, heavier payloads reduce launch capabilities and orbital range, ultimately resulting in elevated launch costs.

As a result of these volume and mass considerations, applying the stiffness approach for response mitigation for spacecraft launch vibrations has strict limits. Structure size, including any support elements, can only be increased up to the volume limit of the rocket fairing. Here, adding dedicated supporting elements restricts useful payload size and raises the proportion of the payload that becomes non-functional, 'dead mass' on orbit.

Reducing stiffness through base isolation can be attempted; however, launch providers typically establish lower limits for the first resonant frequency and generally require an additional frequency separation buffer to guarantee a sufficient margin. This is done to prevent coupling between the payload and the rocket and also to avoid interaction with GNC systems [11]. Furthermore, the actual usable envelope for a payload within a rocket fairing is further limited by the dynamic envelope of the payload during vibration. This means that throughout launch, the deflection of the payload due to vibrations must stay within this designated envelope. The increased compliance from base isolation could result in impact between the payload and the rocket [12]. For these reasons, base isolation tends not to scale well within the limited confines of a rocket fairing as the size and mass of the payload increases.

Shifting to a stiffer, higher modulus material is an alternative, but typically results in a corresponding increase in the mass of the system. Furthermore, existing materials impose a maximum limit on achievable stiffness (Fig. 1.4).
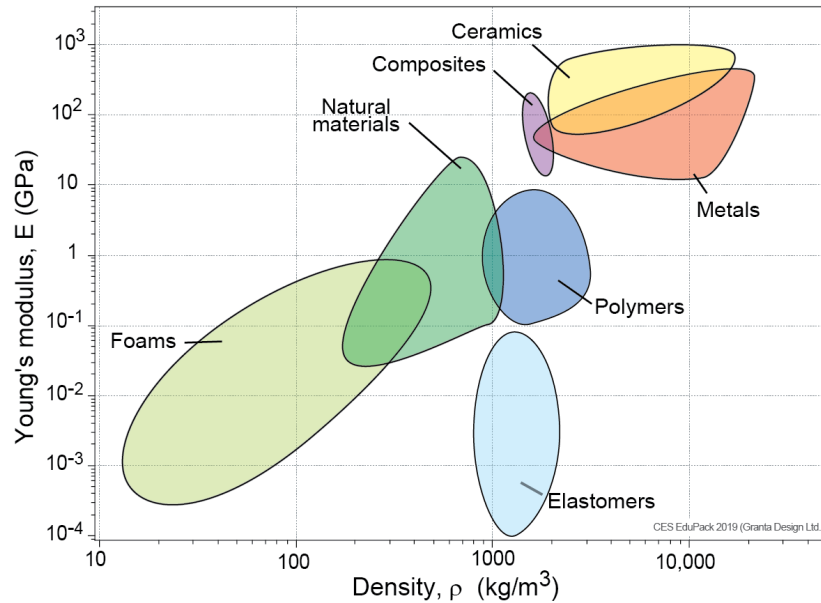
Figure 1.4: Material stiffness vs. density.
(Chart created using CES EduPack 2019, ANSYS Granta © 2020 Granta Design)

More fundamentally, the core issue with relying solely on stiffness modification as a vibration reduction approach depends on the condition that the shifted resonant frequency is out of band of the excitation spectrum. If the excitation loading encompasses a broad range of frequencies, the resonant mode may still be excited, leading to amplification if there is insufficient damping. For these reasons, damping is a necessary consideration in launch vibration mitigation, particularly after pushing the stiffness design knob to its limits.

1.4 Vibration Damping State of Practice and Limitations

There are a variety of vibration damping concepts and techniques, each operating with different working principles and implemented on a spectrum structure scales (Fig. 1.5). Here, there is a specific emphasis on passive dampers because active dampers are generally variations derived from the base, passive design. These include: tuned mass dampers (TMD) (1.5a), tuned liquid sloshing dampers (TLD) (1.5b), friction-based (1.5c), piezoelectric (1.5d), magnetic (1.5e), viscoelastic (1.5f), viscous (1.5g), and particle dampers (1.5h).

(a) Tuned Mass Damper (TMD): secondary mass moving out of phase with primary structure [13]. Ex: vibration mitigation: Taipei 101, Taipei.

(b) Tuned Liquid Damper (TLD): secondary mass moving out of phase with primary structure [14]. Ex: vibration mitigation: One Rincon Hill, San Francisco.
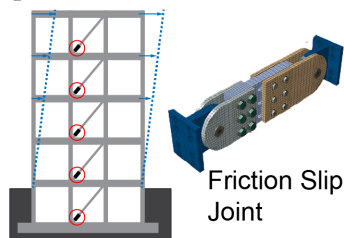
(c) Friction Damper: converts kinetic energy into heat energy through frictional resistance generated between surfaces in contact [15]. Ex: vibration mitigation in buildings.
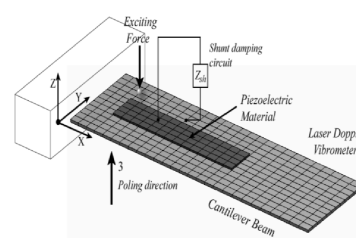
(d) Piezoelectric Damper: applied mechanical stress on piezoelectric material generates electric charge that is dissipated as heat [16].
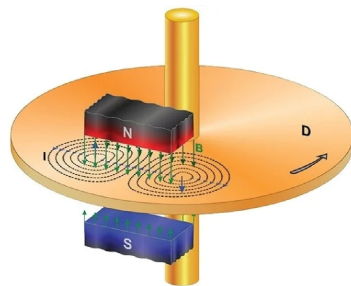
(e) Magnetic Damper: currents induced in conductive material moving within a magnetic field opposes motion [17]. Ex: magnetic braking.

(f) Viscoelastic Damper: dissipates energy through deformation of viscoelastic material. Ex: vibration reduction in sport (archery).

(g) Viscous Damper: dissipates energy through resistance of viscous fluid. Ex: car suspensions.
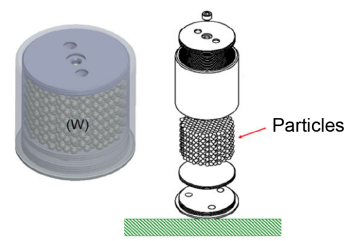
(h) Particle Impact Damper (PID): collision of particles absorb and dissipate energy [18]. Ex: vibration mitigation in circuit boards.

Figure 1.5: Damping devices and typical applications.

While these dampers are commonly used in practice, each of these dampers are subject to one or several of the following limitations:

Trade off Between Stiffness and Damping; Scalability Issues

In general, many of the damping concepts in Fig. 1.5 result in either added mass or increased compliance, which leads to a reduction in stiffness. In this respect, stiffness must be traded off for increased damping. Decreased stiffness results in greater deflection under a given load and also decreases a structure's resonant frequency, which can make it easier to excite a resonant mode. These issues are amplified when considering scalability as the structure size or excitation levels increase. To maintain or increase damping levels, the mass, size, as well as space or stroke requirements of most conventional dampers correspondingly increases as well [19–21].

Excitation Profile Dependence

The damping performance of a number of these concepts is dependent on the profile of the excitation, such as the frequency content, excitation amplitude, and loading rate. Several of these concepts are only effective for particular frequencies or waveforms. This is applicable to the TMD and TLD as well as other damping devices that need to be tuned or otherwise have frequency dependent responses, like the piezo damper [13, 21, 22]. An additional issue with the tuned dampers is robustness to uncertainty, where the performance of the damper depends on the characterization and stability of both the damper and structure properties in order to achieve accurate frequency tuning [19, 21–24].

Under non-harmonic excitation, such as random and shock, a number of these concepts exhibit limited effectiveness in vibration response reduction and may even result in amplification under certain conditions. These issues are common with the concepts whose working principle employs an inertial secondary mass due to the response lag of the secondary mass and corresponding inability to achieve resonance under non-harmonic or impulsive forcing [19, 25, 26].

Apart from the spectra of the waveform, the performance of certain dampers is influenced by factors such as excitation amplitude and loading rate. Sensitivity to both of these factors is commonly seen in viscous type dampers such as air or hydraulic shocks used in base isolation applications. For these damper types, low excitation amplitudes may result in inadequate stroke, which doesn't generate the necessary pressure in the working fluid for effective dissipation. In addition, viscous

dampers are rate dependent, where the damping force is proportional to velocity. Under high frequencies or loading rates, the limiting behavior of these damping elements tends towards that of a rigid link, which transmits loads directly to the structure as opposed to attenuating them [27, 28].

While there are evident challenges associated with the damping performance dependence on excitation profiles, profile independence may introduce its own set of difficulties. Certain damper types, like common implementations of coulomb-friction based dampers, exhibit relatively low sensitivity to variations in loading rate or frequency content [29]. This characteristic could be seen as an additional scaling concern, as the damping remains fixed and does not scale with the applied load or does not discriminate between loading spectra.

Environment Dependence: Space Environment

In addition to the aforementioned issues, dampers designed for use in Earth's atmosphere face significant challenges when applied in the unique conditions of space, characterized by microgravity and vacuum. The conventional form of common damper types that are effective on Earth may exhibit reduced performance and reliability in the harsh conditions of outer space, requiring careful evaluation and redesign.

Devices that rely on gravity may not operate or perform as expected in a zero-gravity environment. Furthermore, devices with fixed or preferred operational orientations face the challenge of constantly changing orientations relative to the gravity vector during launch.

Additionally, careful material selection is crucial to prevent contamination due to low pressure in a vacuum, leading to outgassing and boiling of liquids. Liquid-based dampers therefore need special pressurization or the use of more exotic working fluids [28].

Dampers Are Not Intrinsic to the Structure

Although many of these dampers can be generically implemented in a wide range of contexts and arbitrary structures, the concept of *adding* damping, underscores that these types of dampers are not intrinsic to the original structure. Therefore, their addition results in an increase in mass and complexity of the system.

Particularly in structures for space applications, these added dampers generally result in an increased fraction of the launch mass that becomes 'dead mass', since

they have no other function after reaching space where the vibration environment subsides.

Given these challenges, we pose the question: Is there a category of structures where the vibration mitigation solution is intrinsic to the structure itself? Here, the aim is to find a configuration that not only makes use of existing structural elements to create a damping concept, but also avoids the limitations found in other conventionally used damper types.

1.5 Motivation

Motivation for this work looks to state of the art deployable structures for space such as the Redwire Roll-Out-Solar Array (ROSA), JPL Starshade, and the Caltech Space Solar Power Project (SSPP) [30–33] (Fig. 1.6).

(a) Redwire ISS Roll Out Solar Array (iROSA)

(b) Habitable Exo Planet Class Star Shade (HabEX)

(c) Caltech Space Solar Power Project (SSPP)
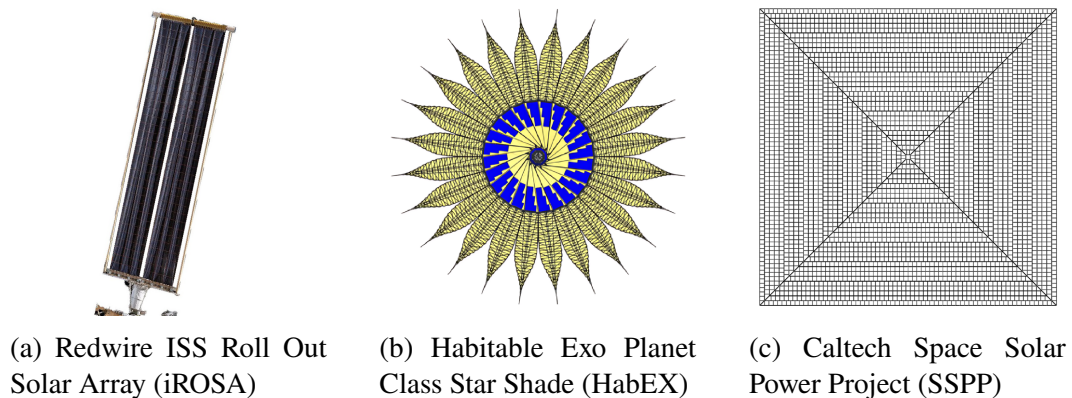
Figure 1.6: Recent state-of-the-art deployable space structures: deployed state (not to scale).

Notably, each of these structure concepts utilize coiling as a packaging architecture in order to stow these structures to fit within launch fairings (Fig. 1.7).
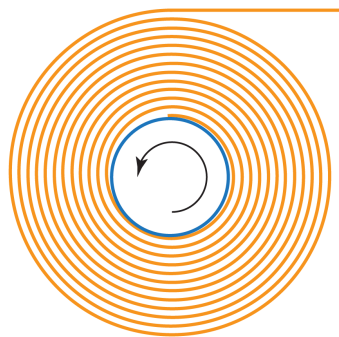
Figure 1.7: Schematic of coiling as a packaging architecture.

Here, looking at these structures in the coiled configuration when they are stowed for launch, we ask whether it is possible to make use of the existing mass and re-purpose it as multi-functional, by having the coil itself provide an energy dissipation mechanism for damping (Fig. 1.8).
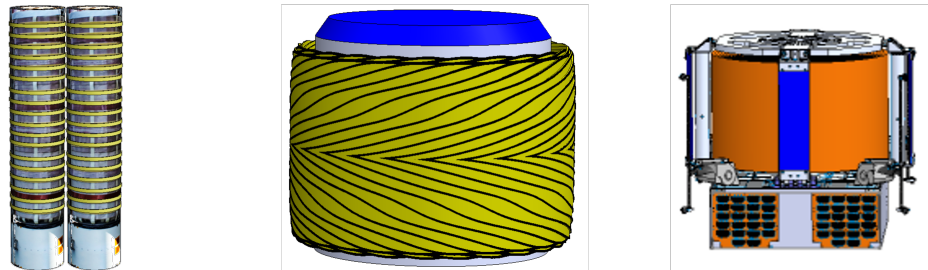
(a) Redwire ISS Roll Out Solar Array (iROSA)

(b) Habitable Exo Planet Class Star Shade (HabEX)

(c) Caltech Space Solar Power Project (SSPP)

Figure 1.8: Recent state of the art deployable space structures: stowed, coiled state (not to scale).

In general, coils are tightly wound with a pretension in order to promote good packing efficiency and prevent coiling defects such as wrinkling, blossoming, and buckling [34, 35]. Additionally, winding tension also keeps the layers of the wound roll restrained when subjected to loads, where previous studies have indicated that varying winding tension affects the degree of interlayer slip observed in a wound rolls subjected to dynamic loading (Fig. 1.9) [36, 37]. This occurs because winding tension controls the magnitude of friction forces between each layer (Fig. 1.10).

Interlayer slip is generally perceived as a defect, and rolls of material are wound tightly during the coiling process to prevent interlayer slip. However, friction, a non-conservative force, transforms mechanical energy into thermal energy and extracts mechanical energy from a system. This energy conversion mechanism of frictional interlayer slip implies the potential to exploit this perceived drawback for practical purposes in vibration response reduction. Hence, interlayer slip emerges as a potential, embedded means of providing vibration damping for coiled structures.

In this research, a variant of friction damping that uses a pretensioned, wound roll, which is referred to as the *wound roll damping concept*, is proposed. Under this approach, the roll is wound around a mandrel or spool with a tension that allows some degree of interlayer slip during vibration. The friction between slipping layers provides the energy dissipation mechanism, which provides damping to the system undergoing vibration, thereby reducing the overall level of excitation (Fig. 1.10).
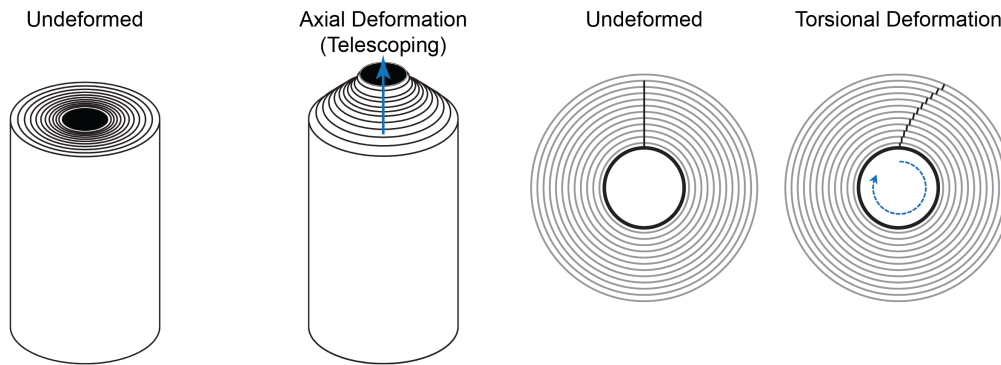
(a) Axial slip (telescoping) in wound rolls.   (b) Torsional slip in wound rolls.

Figure 1.9: Extent of slipping deformations due to dynamic loading controlled by winding tension.
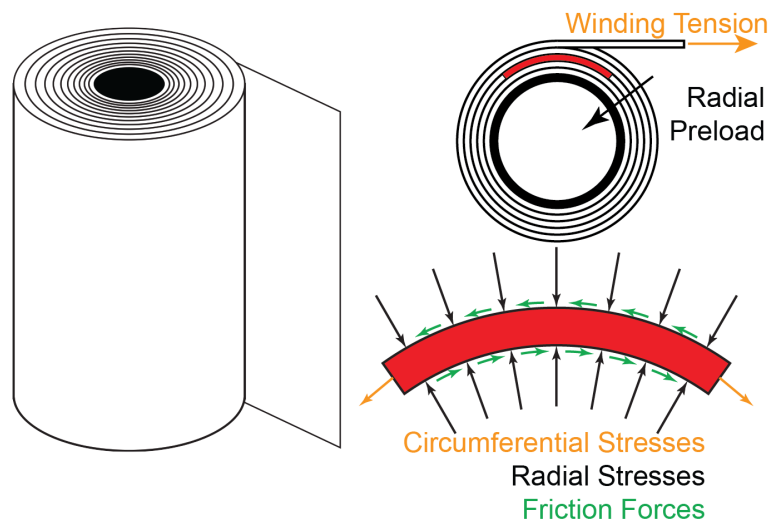
Figure 1.10: Schematic of Wound Roll Damping concept. Coiling pretension applies radial preload to wound layers. Radial stresses support interlayer friction forces that can be used to dissipate energy during vibration.

1.6 Objectives

The goal of this research is to investigate how a wound roll may be used as a passive, vibration damping device, which utilizes friction as the energy dissipation mechanism. Here, the aim is to understand not only how this concept works, but also to assess its efficacy in practical applications. In order to achieve this goal, there is a set of four research objectives.

The first objective is to understand the physical mechanism of this concept by identifying conditions where slip is or is not expected. This is important to understanding the behavior regimes of this damping concept. For conditions where slip does occur,

the locations within the coil that are most likely to slip during vibration need to be identified. Pinpointing these locations enhances comprehension of the behaviors of the wound roll damping concept by indicating regions that play a pivotal role in the damping of energy dissipation. Additionally, determining which regions contribute most significantly to energy dissipation indicates the specific areas to concentrate on for experimental measurements.

The second objective of this study is to experimentally assess the effectiveness of this concept in reducing vibration responses. Here, the goal is to understand how the vibration behavior of this damping concept varies with different winding tensions and excitation profiles. The metrics used to compare the vibration responses are resonant frequency, f_n, and the corresponding damping ratio, ζ.

The third objective is to discover how to model and simulate the behavior of this damping concept. Developing simple models that are capable of capturing experimentally observed behaviors will confirm understanding of the underlying physics.

The fourth and final objective is to assess whether this damping concept addresses the issues identified with other types of dampers. It is crucial to comprehend how its response varies, considering factors like excitation profiles and scalability. The outcomes of this objective provide insights into versatility, performance, and robustness of the damping concept.

1.7 Outline

The organization of this thesis is as follows.

This study begins in Chapter 2 with a theoretical framework for predicting slip locations in a wound roll under vibration. Analytical expressions are employed to assess the stress state within the round roll that supports interlayer friction forces. These stresses are used to determine the friction capacity at each interlayer interface, which estimates the amount of stress an interface can support before slip occurs. The estimates of interlayer slip stress thresholds are combined with numerical simulations of a simplified wound roll under vibration. Initially assuming no slip (coiled-stiff assumption), the coil is modeled as a continuous solid, using simulations to identify shear stresses in the coil during excitation. Comparing shear stress magnitudes obtained from simulation with the friction capacity determines the incidence and location of slip, allowing identification of configurations with slip (violating the non-slip assumption) and configurations without slip (validating the coiled-stiff assumption). The findings of this study inform the design of experiments

in subsequent chapters.

Chapter 3 presents experimental studies of the wound roll damping concept. These experiments are performed on a test sample designed using the results of Chapter 2. The sample is wound under a range of winding tensions and subjected to base vibration using several excitation profiles. The performance of this damping concept is characterized by measuring the resonant frequency and corresponding damping ratio for each configuration. The damping measurements are also correlated with direct measurements of interlayer slip, measured with tracking targets using a high speed camera, and compared with the predicted locations.

Chapter 4 presents FEA simulation techniques for modeling the vibration of wound roll damper. The nonlinear, time domain simulations are performed in ABAQUS dynamic implicit and model frictional slipping interfaces. The frequency response results from FEA are compared to those obtained from experiments for model validation.

Chapter 5 presents a numerical approach for modeling the behaviors of the wound roll damping concept using a reduced order 1D, 2-DoF model. Similar to the FEA model, the primary damping mechanism in this model is friction contact between two mass-spring-damper systems. The results of the numerical model are likewise compared to experiments of the structure for model validation.

Chapter 6 uses the FEA model developed in Chapter 4 to study the performance of the wound roll damping concept in realistic contexts. Here, the model properties and geometries are scaled to recent state-of-the-art deployable space structures.

Finally, Chapter 7 concludes this study and discusses potential avenues for future research.

Chapter 2

PREDICTING SLIP FOR VIBRATIONS OF COILED STRUCTURES

2.1   Introduction

Predicting slip within a layered solid, like a wound roll subjected to vibration, presents a challenge. Depending on the number of wound layers in a coiled structure, there exists multiple interfaces—ranging from dozens to hundreds—where slip may potentially occur. Furthermore, a cylindrical object undergoing vibration is unlikely to have a uniform stress state; the interplay of factors such as the coiled structure's effective stiffness and excitation determines the distribution of the applied loading stresses. As a result, the extent of slip occurrence, both layerwise and axially, is determined by the combined influence of interlayer friction capacity and resulting stresses. This can range from no slip to partial slip or full slip.

This spectrum of slip likely results in a range of vibration responses, dependent on the degree of slip within the coil. Consequently, essential questions arise: What loads can a tensioned coil sustain without slipping? For loads that cause slip, at what locations in the roll does slip initiate? How does the vibration response change with the state of tension or state of slip in the wound roll? Exploring these questions provides insight on the diverse behaviors of the vibration response of a tensioned coil under different conditions.

To address these question, the approach is to start with estimating the frictional shear capacity, which is the maximum stress a frictional interface can withstand before experiencing slip. The shear capacity in a wound roll is determined by the combination of contact properties and the radial state of stress applied by the tension winding process. Thus, this approach requires a model that determines the applied interlayer stresses as a function of the coiling pretension and the number of windings.

In this research, the structure that undergoes coiling is assumed to be a continuous sheet with homogeneous properties and uniform thickness. This simplification allows leveraging existing studies performed in the roll winding industry, which have created analytical models for the radial stresses at any position inside the coil that result from tension winding. There exist a number of advanced stress-field models, that have been validated using experimental measurements of the interlayer stresses

using compression tests or pressure gauges for a number of materials, which account for a variety of effects, such as: complex winding tension profiles, residual stresses, gravity loading, large deformation, finite dimension, and the bending stiffness of the material undergoing coiling [38–43]. However, in this work, the focus is on the foundational models, from which all subsequent models are developed from, which considers the tension winding of a material with negligible bending stiffness [44, 45].

The utility of these stress models in slip estimation in the context of dynamic loading has been demonstrated experimentally using torsional and vibration loading [36, 37]. However, these studies were primarily concerned with preventing slip, and not characterizing the vibration response or damping when slip is allowed. As such, a comprehensive, experimentally-verified approach to predict the slip and vibration response of coiled structures under vibration loading is not yet available.

The proposed methodology for predicting the interlayer slip and response of a wound roll under vibration utilizing the interlayer state of stress from winding is as follows. From a stress-field based analytical model, the interlayer stresses from coiling pre-tension values are generated and used in conjunction with a Coulomb friction model to estimate the interlayer friction capacity. Next, the frictional capacity is evaluated against the shear stresses observed under vibration loads. This is used to determine what loads can a tensioned coil support without slip and the locations of slip for loads where slip is expected.

The stresses applied to a wound roll due to vibration loading can be estimated from analysis and simulation. From structural analysis, estimates of locations of high stresses can be obtained, which will indicate areas where slip is most likely to initiate from. These results are compared with simulation studies, where the model begins with the assumption that the coil has been sufficiently pretensioned so that the no-slip occurs, and therefore behaves as a continuous solid. This *coiled-stiff assumption* allows finite-element analyses (FEA) to be performed using a homogenized solid representation of a coil, as opposed to modeling the individual layers in the coil, which is computationally expensive. This approach has seen effectiveness in simulating slip in dynamic roll hardness impact tests [46], and here it is extended to vibration loading. For now, this assumption provides no information about the damping capabilities of this concept, but would show the vibration response in the limit of no slip.

For the coiled stiff assumption, a natural question arises: what are the effective

material properties of a homogenized solid coil? Coiling is a process that creates an object with orthotropic properties. In cylindrical coordinates, the axial and circumferential stiffnesses as well as the axial-circumferential shear stiffness, $G_{z\theta}$, are related to the in-plane properties of the material undergoing coiling. The other two components of shear stiffness, $(G_{rz}, G_{r\theta})$, and the radial stack modulus, E_r, are affected by the coiling tension and not known a priori.

Experiments and roll quality measurements that quantify a wound roll's ability to resist interlayer slip when an external torque or axial loading indicate that the shear stiffness of the coil varies with location in the roll and with winding tension [36, 47]. While an exact relation between winding tension and the overall effective shear stiffness of the final wound roll is difficult to obtain, a straightforward approach simply involves simulating a range of shear stiffnesses.

Because the effective shear stiffness of the roll is expected to vary with winding tension, even in the absence of slip, it is reasonable to anticipate different vibration responses between a loosely wound roll and a tightly wound roll. As such, comparing the simulation results between shear stiffness configurations illustrates how the vibration response is influenced by winding tension variations.

The proposed slip prediction approach is demonstrated with a case study using the geometry and properties of a notional structure. First, the state of stress is calculated for a constant tension winding process, and the friction capacity is estimated. Next, a simulation is performed where a homogenized solid, which represents the coil, is attached to an elastic mandrel that is subjected to sinusoidal base excitation. The output of this model are the stresses in the coil solid, and the directions of interest are the shear stresses that can induce interlayer slip. If at any point in the coil, the resultant of the shear stresses is below the frictional shear capacity, then no slip can occur and the homogenized solid model may be considered as correct. Conversely, this can also be used to determine at what locations a coil slips when the applied load exceeds the frictional capacity and the solid assumption no longer applies.

The results of this chapter are used to design a lab-scale wound roll test sample used in vibration experiments described later in this work.

2.2 Approach for Quantifying Slip Resistance

Interlayer Stresses in Wound Rolls

To determine the interlayer stresses in a wound roll, a nonlinear stress-field model that accounts for the anisotropy of the coiling process, where the effective radial

modulus of a layered solid varies with stack compression, is used. This section will begin with a brief restatement of the derivation of the stress model as specified in previous studies [45, 48, 49].

In this model, the wound roll, which in reality is geometrically a spiral, is approximated as a series of concentric cylinders which represent different coiled layers in order to study the winding process using an axisymmetric approach. Assuming that stresses within the wound roll are solely dependent on radial position and remain invariant with respect to axial or circumferential position, the problem is further simplified by adopting the assumption of plane stress. This allows modeling the coiling process as adding a series of tensioned rings in 2D. (Fig. 2.1).
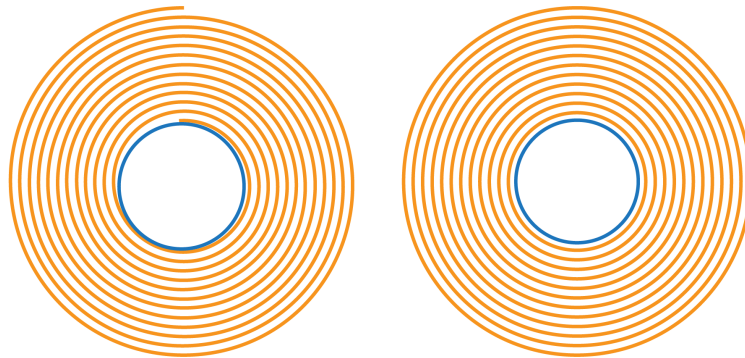
Figure 2.1: Approximation of a 2D spiral coil (left) as a series of concentric circles (right) for axisymmetric analytical treatment.

Examining a segment of a coil wrap allows for the consideration of a free body diagram in order to illustrate the forces acting on a segment (Fig. 2.2).
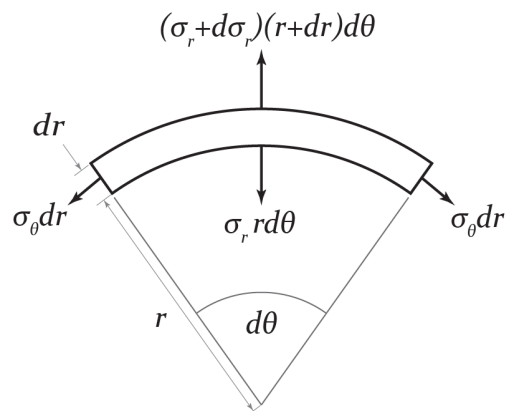
Figure 2.2: Coil segment free body diagram.

Equilibrium of this segment requires that the net forces in the radial and circumferential directions are balanced. Because of circular symmetry, circumferential equilibrium is automatically satisfied, and only the radial direction needs to be considered.

The radial equilibrium of the segment couples the radial and circumferential stresses and is given by:

$$r\frac{d\sigma_r}{dr} + \sigma_r - \sigma_\theta = 0 \tag{2.1}$$

Similarly, strain compatibility in cylindrical coordinates to ensure no gaps or overlaps is given by:

$$r\frac{d\epsilon_\theta}{dr} + \epsilon_\theta - \epsilon_r = 0 \tag{2.2}$$

The stress-strain constitutive relations for linear orthotropic materials are equations relating the strain, ϵ, stress, σ, moduli, E, and Poisson's ratio, ν, in the radial and circumferential directions and are given by:

$$\text{Radial Direction:} \quad \epsilon_r = \frac{\sigma_r}{E_r} - \nu_\theta \frac{\sigma_\theta}{E_\theta} \tag{2.3a}$$

$$\text{Circumferential direction:} \quad \epsilon_\theta = \frac{\sigma_\theta}{E_\theta} - \nu_r \frac{\sigma_r}{E_r} \tag{2.3b}$$

Combining relations 2.1, 2.2, and 2.3 results in the winding equation:

$$r^2\frac{d^2\sigma_r}{dr^2} + 3r\frac{d\sigma_r}{dr} + \left(1 - \frac{E_\theta}{E_r}\right)\sigma_r = 0 \tag{2.4}$$

Fig. 2.3 shows the geometry for the model of the winding problem under consideration. The state of stress of the coil during the winding process changes with each additional winding. As such, if $\delta\sigma_r(r)$ is the increment in interlayer pressure inside a roll, which currently has n layers and outer radius, $r = r_n$, due to an additional $n + 1$ winding, Eq. 2.4 can be rewritten as:

$$r^2\frac{d^2\delta\sigma_r}{dr^2} + 3r\frac{d\delta\sigma_r}{dr} + \left(1 - \frac{E_\theta}{E_r}\right)\delta\sigma_r = 0 \tag{2.5}$$

Eq. 2.5 is a second-order boundary value problem subject to two boundary conditions. The first boundary condition states that the radial stress at the current roll outer radius, $r = r_n$, due to an additional wrapping, is determined by the winding tension through the hoop stress relation. For a continuous sheet of constant thickness, h, and negligible bending stiffness, wound with tension that generates an in-line winding
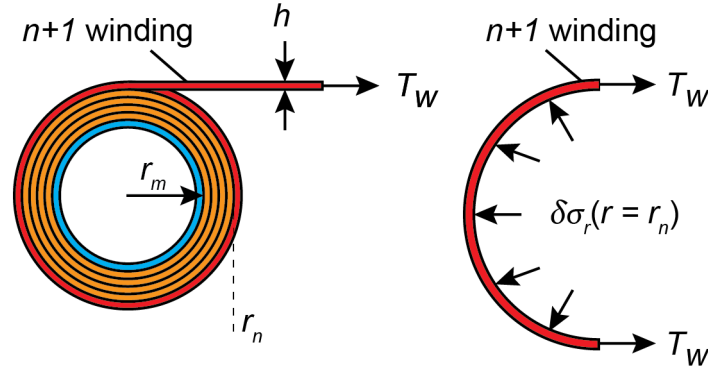
Figure 2.3: Winding geometry of a roll with current radius, r_n, with an additional $n + 1$ layer wound with a winding stress, T_w.

stress, T_w, the incremental interlayer stress, $\delta\sigma_r$, of an additional winding is given by:

$$\delta\sigma_r = \left[\frac{T_w}{r}\right] h \quad \text{at} \quad r = r_n \quad \text{(current outer radius of roll)} \tag{2.6}$$

In principle, this model is general enough to take any arbitrary winding stress profile, $T_w = T_w(r)$, but a constant tension stress profile is assumed here for simplicity.

The second boundary condition is an additional statement of strain continuity between the radial deflections of both the mandrel and the roll at the interface of the first winding:

$$r_m \frac{\mathrm{d}\delta\sigma_r}{\mathrm{d}r} = \left(\frac{E_r}{K_m} - 1 + \nu_\theta\right)\delta\sigma_r \quad \text{at} \, r = r_m \quad \text{(outer radius of the mandrel)} \tag{2.7}$$

Here, K_m is the mandrel stiffness, which relates the applied radial stresses to the corresponding radial deflection, and is a function of the mandrel material and geometry. For an isotropic mandrel with material modulus, E_m, Poisson ratio, ν_m, outer radius, r_m, and inner radius, r_i, the mandrel stiffness is given by [49]:

$$K_m = \frac{E_m}{\frac{(r_m/r_i)^2+1}{(r_m/r_i)^2-1} - \nu_m} \tag{2.8}$$

In this analytical model for winding stress, the majority of the material properties are assumed to remain constant during the winding process. However, the radial modulus of the coiled material, E_r, is typically assumed to vary with the interlayer pressure. In experimental settings, the stack modulus of a layered solid is observed to depend on the number of layers and applied preload, exhibiting distinctive behaviors

compared to an equivalently sized continuous solid or even a standalone layer [50, 51].

The stress-strain curves of layered solids exhibit nonlinearity, possibly due to variations in layer-to-layer contact induced by factors such as asperities, air entrapment, thickness fluctuations, and the bending stiffness of the material. A typical expression for the radial modulus as a function of the interlayer stresses is derived from taking the derivative of experimentally measured stress-strain curves, and is given by [48, 52]:

$$E_r(r) = K_1 K_2 + K_2 \sigma_r(r) \tag{2.9}$$

The constants K_1 and K_2 can be determined through experimental measurements or obtained from materials that have already been characterized.

Because the boundary value problem depends on terms that are functions of radial position, r, this problem must be solved numerically. Here, the finite difference approach described in [45] is used, where a center difference approximation of the derivatives in Eq. 2.5 is used to generate the incremental winding equation for the nth winding:

$$\delta\sigma_{r,n+1}[A_n] + \delta\sigma_{r,n}[B_n] + \delta\sigma_{r,n-1}[C_n] = 0 \tag{2.10}$$

for:

$$A_n \equiv 1 + (3h/2r_n)$$

$$B_n \equiv (h^2/r_n^2)(1 - E_\theta/E_r) - 2$$

$$C_n \equiv 1 - (3h/2r_n)$$

For a coil consisting of N windings, Eq. 2.10 can be expressed iteratively to obtain a system of $N-1$ equations with $N+1$ unknown interlayer stresses, $\delta\sigma_{r,1}, \delta\sigma_{r,2}, ...\delta\sigma_{r,N}, \delta\sigma_{r,N+1}$:

$$\delta\sigma_{r,N+1}[A_N] + \delta\sigma_{r,N}[B_N] + \delta\sigma_{r,N-1}[C_N] = 0$$

$$\delta\sigma_{r,N}[A_{N-1}] + \delta\sigma_{r,N-1}[B_{N-1}] + \delta\sigma_{r,N-2}[C_{N-1}] = 0$$

$$\vdots$$

$$\delta\sigma_{r,3}[A_2] + \delta\sigma_{r,2}[B_2] + \delta\sigma_{r,1}[C_2] = 0$$

Here, $\delta\sigma_{r,N}$ is the incremental radial pressure on the outside of layer $N - 1$.

The boundary conditions in Eq. 2.6 and Eq. 2.7 provide the necessary additional relations to solve this system of equations, but must be expressed in discrete form. Eq. 2.6 can be rewritten directly as:

$$\delta \sigma_{r,N+1} = \frac{T_{w,N+1}}{r_{N+1}} h \tag{2.11}$$

Since there is no layer beneath the mandrel, Eq. 2.7 uses a forward difference approximation for the derivative instead of a center difference scheme:

$$r_m \frac{\delta \sigma_{r,2} - \delta \sigma_{r,1}}{h} = \left(\frac{E_\theta}{K_m} - 1 + \nu_\theta \right) \delta \sigma_{r,1} \tag{2.12}$$

Eqs. 2.11 and 2.12, in conjunction with the $N-1$ equations written from Eq. 2.10, form a linear system of $N+1$ equations with $N+1$ unknowns that can be represented as a matrix:

$$\mathbf{Ax} = \mathbf{B} \tag{2.13}$$

where $\mathbf{A}$ is a tri-daigonal matrix containing the coefficients of the center difference approximation of the winding equation derivatives, $\mathbf{x}$ is a column matrix of the unknown interlayer stresses $\delta \sigma_{r,1}, ...\delta \sigma_{r,N+1}$ to be solved for, and $\mathbf{B}$ is a sparse column matrix containing the boundary conditions. Eq. 2.13 can simply be inverted to find the interlayer stresses that arise due to the additional layer.

For a known number of layers and a given winding setup, this stress field model can be recursively applied, starting from the first layer until the last, to get the incremental radial stresses at each winding step. If the discrete stresses, found by solving the system for the nth winding, $\mathbf{x}_n = [\delta \sigma_{r,1}, \delta \sigma_{r,2}, ..., \delta \sigma_{r,n}, \delta \sigma_{r,n+1}]$, can be interpolated and represented as a continuous function of r as $[\delta \sigma_r(r)]_n$, the summation of the contributions of incremental radial stress for each layer gives the total stress distribution:

$$\sigma_r(r) = \sum_{n=1}^{N} [\delta \sigma_r(r)]_n \tag{2.14}$$

This provides the methodology necessary to determine the interlayer stresses at any location within a wound roll that result from the winding process.

The shape of the stress field distribution through the coil is sensitive to the moduli of the material being coiled. Fig. 2.4 shows a notional comparison between a 'soft' roll ($E_\theta \gg E_r$), where the material is much stiffer in tension than in radial, through thickness compression, vs. a hard roll ($E_\theta \approx E_r$), where the radial and tangential properties are comparable. Regardless, since the additional winding compresses the other layers beneath it, the radial stress field in generally will be maximum at the mandrel interface and tapers outwards for subsequent layers.

(a) 'Soft' Roll ($E_\theta \gg E_r$)   (b) 'Hard' Roll ($E_\theta \approx E_r$)
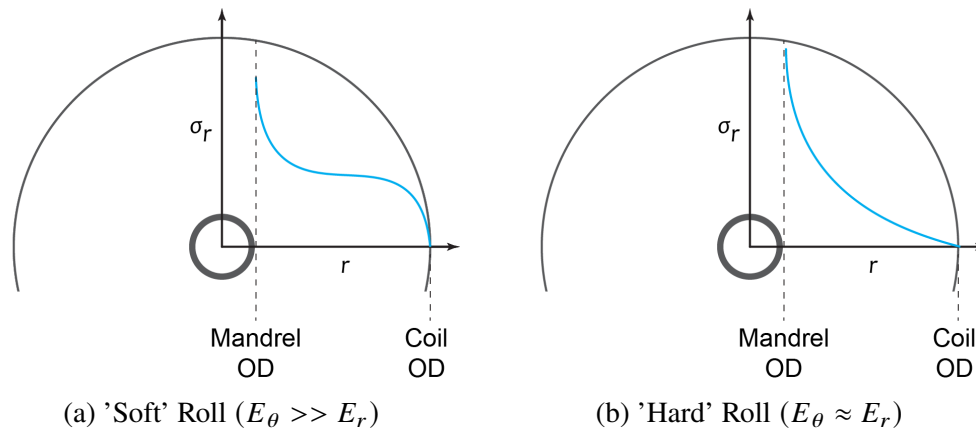
Figure 2.4: Interlayer radial stress profiles in wound rolls.

Interlayer Friction Capacity of Wound Rolls

The previous section enables the estimation of the state of stress in a wound roll that arises due to a tension winding process. The compressive interlayer stresses, σ_r, provides the normal reactions which are necessary for two surfaces to support friction forces. The next required component is a model to describe how these interlayer normal stresses relate to the friction forces that resist interlayer slip.

Friction is a complex phenomenon, that can demonstrate nonlinear behaviors which are contingent on various factors such as velocity, preload magnitude, time, and temperature [53–55]. However, this work utilizes the Coulomb friction model, which is widely used because it provides a simple way to describe the frictional forces between two surfaces in relative motion and has demonstrated good predictive capability in experiments [56, 57].

For two solid surfaces in contact, the friction force between the surfaces that resists relative motion, F_f, is proportional to the normal preload, F_n:

$$F_f \leq \mu F_n \tag{2.15}$$

The constant of proportionality here is the coefficient of friction, μ, which is typically obtained through empirical measurements.

This relation can be extended to the cylindrical contact surfaces in wound rolls, using stresses rather than forces. The frictional shear capacity, σ_c, is defined as the maximum stress a layer can support without slip. Under the Coulomb model, the shear capacity is proportional to the interlayer stress through the coefficient of friction, μ [36]:

$$\sigma_c = \mu \sigma_r \tag{2.16}$$

Because this model simply linearly scales the stress field model calculated previously, the variation of the friction capacity through layers follows the same shape as the stress-field seen in Fig. 2.4. Therefore, the shear capacity is maximum at the mandrel interface and tapers outwards for subsequent layers.

Shear Resultant Metric

The friction capacity provides the stress threshold that delineates between no-slip and slip conditions. In order to assess against the threshold, the stress directions that can induce slip and determine the loading magnitude are needed. The deformation directions for a wound roll that result in interlayer slip correspond to the out-of-plane axial and in-plane shear directions (Fig. 2.5). The expected interlayer slip mode for axial shear, σ_{rz}, is telescoping (Fig. 1.9a), while in-plane shear, $\sigma_{r\theta}$, can result in torsion (Fig. 1.9b).

In the analytical stress models, it was assumed that there is no circumferential or axial variation of stresses, and hence there is likewise no directional variation in shear capacity at a radial interface. The primary focus here is to determine the occurrence and location of slip, rather than the specific direction of slip. Therefore, it suffices to solely assess the magnitude of the resultant stresses at a given point. As a result, σ_s, the resultant of the out-of-plane and in-plane shear stresses at a point can be calculated from [46]:

$$\sigma_s = \sqrt{\sigma_{rz}{}^2 + \sigma_{r\theta}{}^2} \tag{2.17}$$

The shear resultant at any point in the coil can then be compared against the estimated shear capacity at that layer to determine the state of slip:

$$\text{Slip State} = \begin{cases} \text{no-slip} & \text{if } \sigma_c \geq \sigma_s \\ \text{slip} & \text{if } \sigma_c < \sigma_s \end{cases} \tag{2.18}$$

This criterion can now be used in conjunction with analytical models or FEA to determine where a coiled structure will slip under vibration loading.

2.3 Determining Approximate Locations of Slip Via Analytical Stress Estimates

In order to determine whether slip occurs, the distribution of stresses inside the coil that result from vibration are required. The mounting configuration considered is one where the supporting mandrel is mounted in a cantilevered configuration. Here
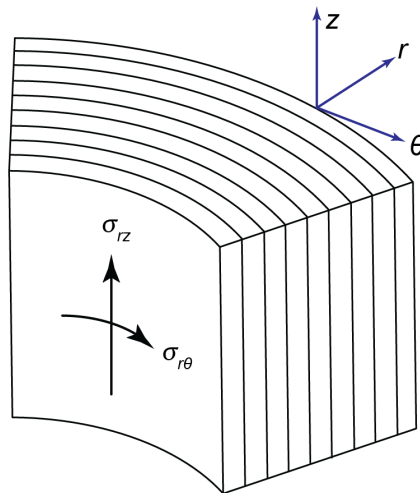
Figure 2.5: Shear components of interest for interlayer slip in wound rolls.

the mandrel is base fixed, but the coil is not and is attached only to the mandrel (Fig. 2.6).
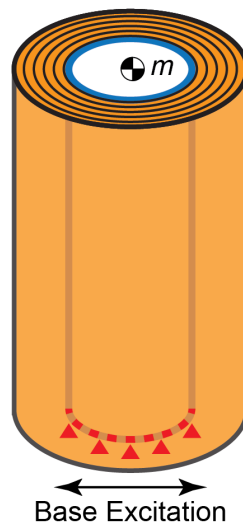
Base Excitation

Figure 2.6: Wound roll configuration of interest: roll attached to cantilevered mandrel, with tip mass, subjected to base excitation.

With the additional constraint that the ends of the mandrel are held to remain circular, and the likelihood that there is some tip mass bias, the vibration mode of wound rolls is expected to be a bending mode for a wide range of configurations. As such, this entire body of work assumes that the primary mode shape of a cantilevered wound roll under vibration is a bending mode. With the loading state of interest defined, simple analytical models can be used to predict locations of high stresses.

Assuming a bending vibration mode, the loading of the wound roll assembly due to base excitation can be approximated as a cantilever beam with under a uniformly distributed load and a tip load (Fig. 2.7). Here the beam considered only accounts for the mandrel, where the stiffness and dimensions of the wound roll are not considered in the beam properties. Only the inertia of the roll is accounted for in the magnitude of the uniform loading.

Using this approximation, there is no direct information given for the stresses inside the wound roll. However, there are closed form analytical expressions for the stress distributions expected inside the base-fixed mandrel. These distributions can be used to estimate the traction that the mandrel would apply on the wound roll during vibration. Since the wound roll boundary conditions are otherwise free, except at the mandrel interface where the roll is attached, the highest stresses are expected to occur at that interface and decay outwards.
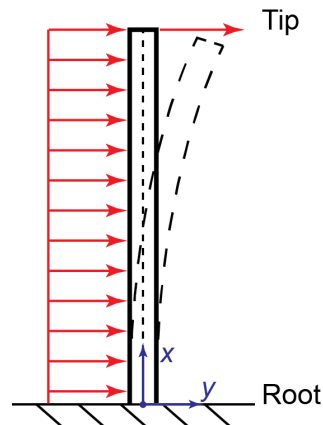
Figure 2.7: Approximation of wound roll vibration as cantilever beam subjected to uniform load and tip load.

This combination of loading for a cantilever beam does not result in pure bending, so shear forces exist. This can be notionally demonstrated in the shear and moment diagram for this loading in Fig. 2.8.

When considering the failure loads of cantilever beams, two metrics to consider are the bending and shear stresses. The relations for the bending and shear stresses as a function of the axial position, x, and the distance from the neutral axis, y, is determined by the distribution of shear forces, V, the moment, M, and the second
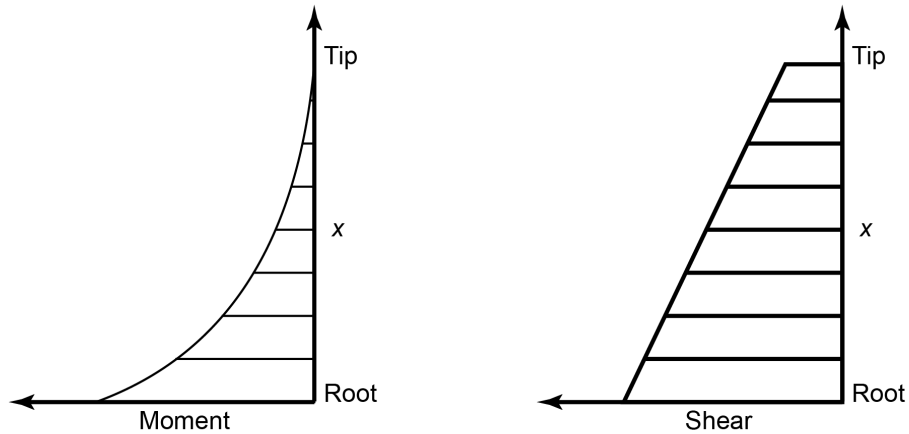
(a) Moment distribution along the length of the cantilever beam.

(b) Shear distribution along the length of cantilever beam.

Figure 2.8: Notional shear and moment diagrams for cantilever beam under uniformly distributed and tip loads. Shear and moment are largest at the root.

moment of area, I. The stresses are given by the expressions in Eq. 2.19 and Eq. 2.20.

$$\sigma(x, y) = \frac{M(x)y}{I} \tag{2.19}$$

$$\tau(x, y) = \frac{V(x)}{It} \int y dA \tag{2.20}$$

In Fig. 2.8a and Fig. 2.8b, the largest shear and moments are located near the root for $x = 0$. This identifies the root cross-section as a location of interest for high stresses. The next step is to determine where, within the root cross-section, are the stresses highest.

From the bending stress relation in Eq. 2.19, the stress is linearly proportional to the distance away from the neutral axis through y. Thus, the highest bending stresses are expected at the outer surfaces of the mandrel aligned with the loading axis (Fig. 2.9a). This implies that the interface at the root, between the mandrel and coil, on the surfaces aligned with the vibration axis is likely to be significant for interlayer slip.

From the transverse shear stress relation in Eq. 2.20, the term in the integral is the first moment of area between the location where the shear stress is being calculated and the neutral axis where the shear stress is zero. In the case of a cylinder, this result indicates the maximum transverse shear stress occurs at the neutral axis (Fig. 2.9b).

(a) Locations of highest bending stresses.

(b) Locations of highest transverse shear stresses.
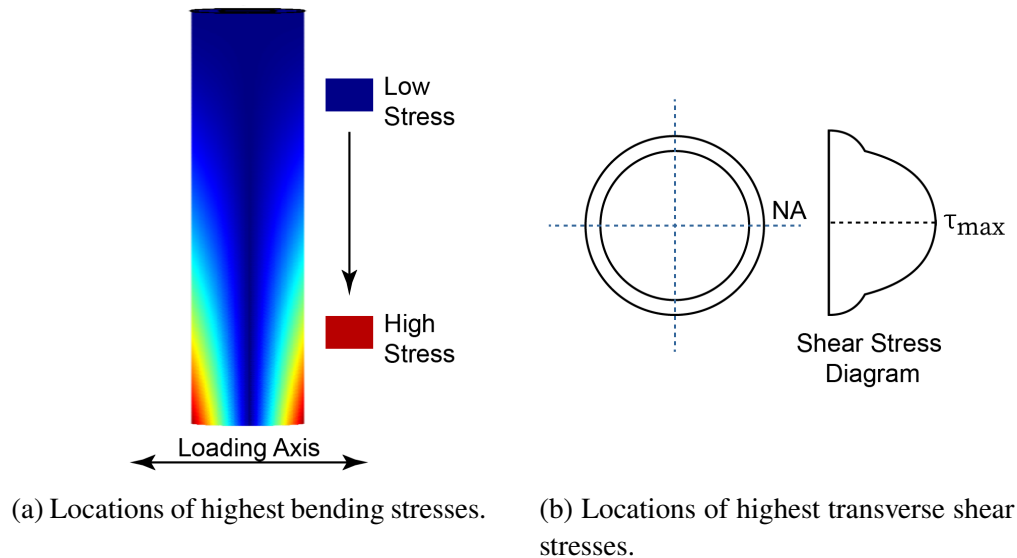
Figure 2.9: Locations of highest stresses for beam bending.

These simple analytical expressions provide an approximate indication of the locations where slip initiation can be anticipated. More detailed predictions of slip can be obtained from FEA where the vibration of a wound roll can be simulated and used to directly compute the stress resultants at every point inside the coil.

2.4 Case Study: FEA Approach to Predict Interlayer Slip

This section, demonstrates the slip prediction approach using FEA by studying the vibration of a notional structure. The material properties are derived from a coilable structure currently under development at Caltech, and the geometry is informed by scaling a portion of the structure to a larger size. First, the friction capacity of the coiled structure is estimated for assumed winding parameters. Then, the capacity is compared to the shear stress resultants obtained from a FEA simulation of the wound roll under vibration loading.

Structure and Mandrel Definition

The structure of interest is a segment of the Caltech Space Solar Power Project (SSPP) structure called a 'strip', which consists of an ultra-thin, sparse carbon fiber structure, with large cutouts, supporting a Kapton membrane (Fig. 2.10) [33, 58].

This study assumes that there is a strip is long enough to form 300 coiled layers around a 300 mm tall, aluminum mandrel with a 2 cm outer diameter and 1 mm wall thickness. The outer diameter of the final packaged coil is expected to be approximately 5 cm (Fig. 2.11).
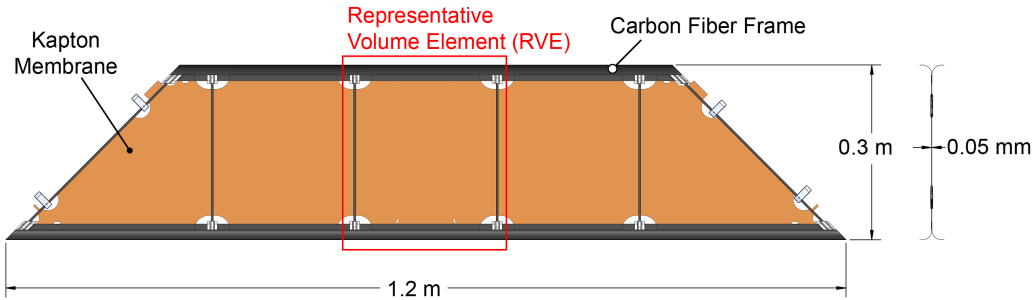
Figure 2.10: Structure of interest: SSPP strip. Representative Volume Element (RVE) pictured containing carbon fiber elements and Kapton membrane.

The dimensions of the mandrel-coil system are shown in Table 2.1.

Table 2.1: Coiled Structure Geometry

r_m (mm)	t_m (mm)	L (mm)	t_s (mm)
10	1	300	15
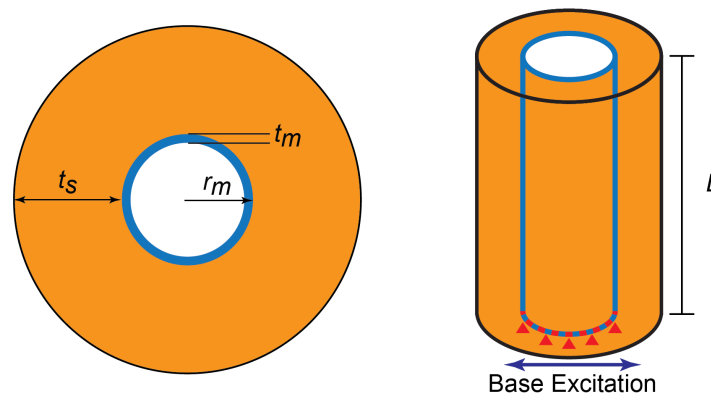
Figure 2.11: Geometry of coiled structure.

Expected Shear Capacity Due to Winding

To determine the shear capacity of the coil using the winding model of interlayer stress, the structure is homogenized during the winding process as a sheet which has a uniform thickness, h, that is coiled with a constant winding stress equal to approximately half the tensile yield stress of Kapton. Additionally, the coefficient of friction between layers corresponds to the reported values of Kapton-Kapton coefficient of friction [59].

The chosen winding parameters are shown in Table 2.2 and the assumed coiled structure material parameters are shown in Table 2.3. Note that the coefficients, K_1

and K_2 for the nonlinear stack modulus in Eq. 2.9 are obtained from [60], assuming Kapton has similar compression behavior as polyester.

With these values, and the geometry in Table 2.1, the interlayer stresses as a function of radial position in the coil are calculated according to the process laid out in Section 2.2 and the capacity is then found by scaling the result by the coefficient of friction as denoted in Eq. 2.16.

Table 2.2: Winding Parameters

Property	Value
Winding stress, $T_w \approx 0.5\sigma_{Y,Kapton}$	40 MPa
Structure thickness, h	0.05 mm
Number of layers, $n = t_s/h$	300
Coeff. friction, μ	0.48

Table 2.3: Coiled Structure Material Parameters

E_θ	E_m	K_1	K_2
10 GPa	70 GPa	1 kPa	40 GPa

The shear capacity as a function of the radial position is shown in Fig. 2.12. Here, the horizontal axis is normalized by the mandrel radius, r_m. Fig. 2.12 indicates as expected, the innermost layers are expected to have the largest shear capacity, and hence resistance to slip is largest at the mandrel-coil interface and reduces radially outward. The shear capacity must now be evaluated against the vibration induced shear stresses from FEA to determine where slip occurs in the coil.

Homogenized Solid Approximation of Coils for FEA

Rather than modeling discrete windings of the wound structure, which is computationally expensive, this effort begins with the coiled-stiff assumption where the coil is assumed to be tensioned sufficiently that no interlayer slip occurs, and it behaves mechanically as a continuous solid. Thus, the model consists of a homogenized solid, with material properties calculated from a representative volume element (RVE) of the structure of interest (Fig. 2.10). The unit cell of the structure consists of carbon fiber framing supporting a Kapton membrane. Where relevant, the material properties are calculated according to the weighted mean of all constituent materials, for example in the case of certain moduli, or determined from the properties of the membrane when its properties are the limiting factor.
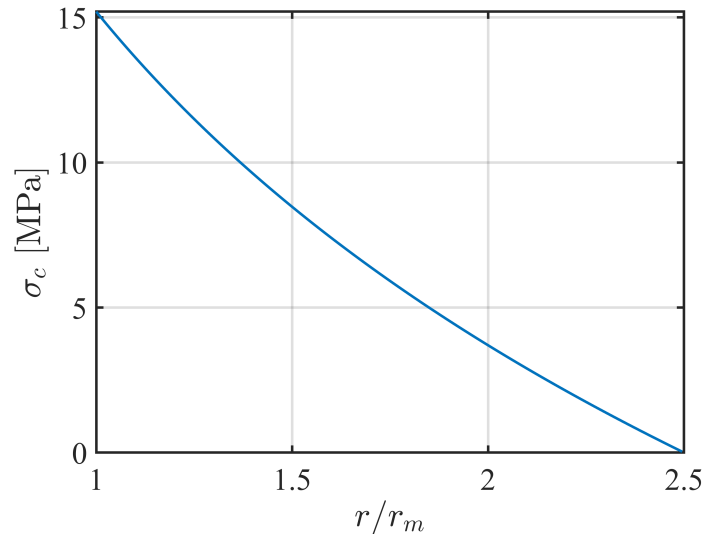
Figure 2.12: Estimated shear capacity of coil wound with constant stress of 40 MPa.

The material properties of this homogenized solid are transversely isotropic to emulate the orthotropy of a wound roll. Using cylindrical coordinates: E_θ, E_z, and $G_{z\theta}$ are defined by the in-plane properties of the structure of interest. The moduli that are directly affected by the coiling process are the radial modulus, E_r, and the shear moduli, G_{rz} and $G_{r\theta}$. As discussed in Section 2.2, E_r is dependent on the number of layers in the stack and increases the more tightly the coil is wound. The value of E_r must be found experimentally through compression testing, however here $E_r = 1\% E_\theta$ is assumed, which is a typical order of magnitude result from stack compression experiments on wound roll materials [60].

The remaining unknown moduli that are impacted by the coiling tension are the shear moduli G_{rz}, and $G_{r\theta}$. As the coiling tension increases, the interlayer frictional shear capacity also increases, and this should result in a measurable increase in the shear stiffness of the wound roll. Variation in the effective stiffness of an object can generally be measured indirectly via vibration testing, as the resonant frequency correlates with moduli. Thus, in this work, rather than directly measuring the effective shear stiffness variation with winding tension, changes are assessed indirectly using the resonant frequency of vibration.

For this study, G_{rz} and $G_{r\theta}$ are assumed to be identical, which is consistent with the assumptions that there is no axial or circumferential variation in shear capacity. Under this assumption, a range of values are studied to determine the vibration response sensitivity to shear stiffness for the first study. Next, to determine the loading stress distribution from vibration for the second study, only one value

of shear stiffness is needed. Here, the maximum shear stiffness from the range considered in the first study is selected, which corresponds to the scenario where the contributions of shear stiffness in this homogenized RVE come from an isotropic material: $G_{z\theta} = G_{r\theta} = G_{rz}$. This condition is considered the maximum theoretical limit of effective shear stiffness, where regardless of winding tension, the stiffness of a wound roll is not expected to exceed that of a continuous solid.

The material properties used in this simulation are found in Table 2.4. While modeling a wound roll as a homogenized solid does not provide information about damping, these simulations indicate the sensitivity of the vibration response of this configuration to winding tension in the no-slip regime.

Table 2.4: Homogenized Structure RVE Material Parameters

E_θ (GPa)	E_z (GPa)	E_r (GPa)	v_{ij}	$G_{z\theta}$ (GPa)	$G_{r\theta}, G_{rz}$ (GPa)	ρ_s (kg/m^3)
10.0	5.0	0.1	0.3	1.0	0.1–1.0	1600

FEA Model Setup and Simulation Procedure

The FEA model studies the configuration where the homogenized coiled structure is supported by an isotropic, aluminum mandrel, fixed in a cantilevered configuration. The mandrel is defined by the wall thickness t_m, length L, and outer radius r_m and is modeled using S4R shell elements. The coiled structure is defined by its thickness t_s and length L and is modeled using C3D20R solid elements. The structure is assumed to be perfectly bonded to the mandrel's outer diameter, but not to the mandrel's base (Fig. 2.11).

The finite element software ABAQUS was used to perform two studies. The first study investigates how the 1st bending mode resonant frequency varies with the shear stiffness of the coiled-solid. The resonant frequency here is used as an indirect gauge of the apparent stiffness of the modeled assembly. Loosely wound rolls are anticipated to demonstrate lower apparent stiffness, which should correlate to lower resonant frequencies compared to tightly wound rolls.

The second study sets $G_{z\theta} = G_{r\theta} = G_{rz}$ to estimate the loads where slip is expected to occur in a coil under transverse vibration loading. First, a linear frequency analysis is performed on the assembly, extracting the first 10 modes. This model is then used in a modal dynamics step, where the transient response is determined using the extracted modes of the system as a basis. In the dynamics step, the structure is subjected to sinusoidal base excitation at the first natural frequency of the system

in order to subject the assembly to the highest loads, using a span of acceleration levels from $1 - 15g$.

In this model, interlayer slip is not accounted for, so there is no damping in this model up to this point. However, some level of damping must be included to have finite acceleration. Here, a modest 2% damping is assumed across all modes. The model is run for a duration sufficiently long for the maximum displacement of the structure to reach a steady state. The observed peak shear stress resultant and corresponding location in the roll during the steady state response is recorded for each acceleration level and is compared against the shear capacity to determine the regions where slip would be expected.

Vibration Response Variation With Shear Stiffness

First, the variation in wound roll vibration response with shear stiffnesses is examined. Fig. 2.13 shows how the 1st bending mode resonant frequency of the wound roll assembly changes with shear stiffness. Note that for low values of shear stiffness, the bending mode is not the fundamental, i.e., the lowest resonant frequency, mode. Usually, the lowest mode for low shear stiffness corresponds to either axial or torsional shear. However, the mass participation factors of these modes is much lower than the bending mode, so they are discarded.

The red line in this plot corresponds to the case where the coiled solid is removed from the model, and instead, its inertia is uniformly distributed along the mandrel as a non-structural mass. This represents the case where the coil is not providing stiffness to the assembly and behaves only as an added mass. The y axis for this plot is normalized by the resonant frequency of the non-structural mass case.

This plot demonstrates that there is a geometric benefit to coiling. For all shear stiffnesses considered, the resonant frequency of the wound roll assembly is higher than that of the non-structural mass case. This result is significant as it indicates the advantage of using the wound roll as a structural element. Taking into account the coil geometry leads to improvements in properties, such as increased cross-sectional area and second moment of area, thereby contributing to enhanced stiffness.

Furthermore, there is a range of low shear stiffnesses, where the variation in response is minimal, as evidenced by a relatively flat curve. Beyond this range, there is a critical threshold of shear stiffness where the assembly response becomes notably more sensitive to increasing shear stiffness. Because shear stiffness is positively correlated with winding tension, this suggests that vibration response of wound
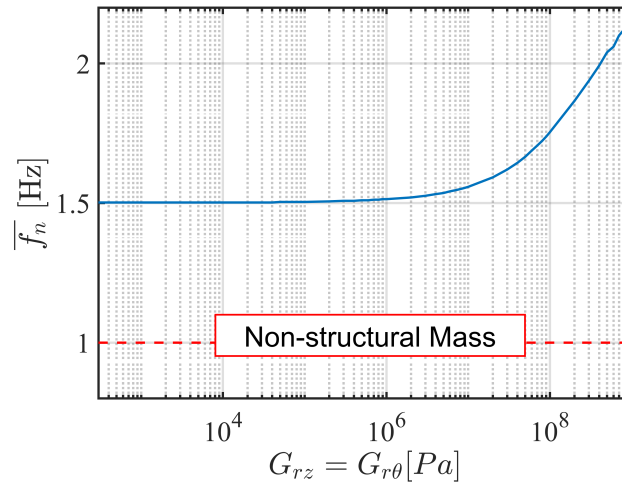
Figure 2.13: Variation in bending mode resonant frequency with effective shear stiffness of coil.

rolls can vary significantly with winding tension. This property is exploited in a later section for experimental design. To proceed to the second FEA study, only one value of shear stiffness is needed. Here, the largest value of shear stiffness in the range considered is selected, which corresponds to the most tightly wound, slip resistant roll.

Locations of Slip Within a Coiled Structure Under Vibration

In the second study, the coiled stiff structure is subjected to base vibration with a range of excitation levels at the assembly's natural frequency, $f_n \approx 100$ Hz, where resonance is expected to exhibit the highest loading. The stress components extracted from the vibration simulation are used to compute the stress resultant at every point in the roll. The stress resultants are then consolidated into a histogram and plotted against the axial and position in the coil, shown in Fig. 2.14, to identify regions of high shear stresses. Superimposed on these plots is the maximum shear capacity at the corresponding radial or axial position estimated previously. Note that the shear capacity was assumed to vary only radially, and is invariant to axial position. Thus, in the axial direction, the maximum shear capacity curve is constant, as denoted by the red horizontal dotted line in Fig. 2.14a. The horizontal axis of the axial distribution plot in Fig. 2.14a is normalized by the length of the assembly, $L = 300$ mm. The horizontal axis of the radial distribution plot in Fig. 2.14b is normalized by the radius of the mandrel, $r_m = 10$ mm. The vertical axis of both plots is normalized by the maximum shear capacity, $\max(\sigma_c)$.
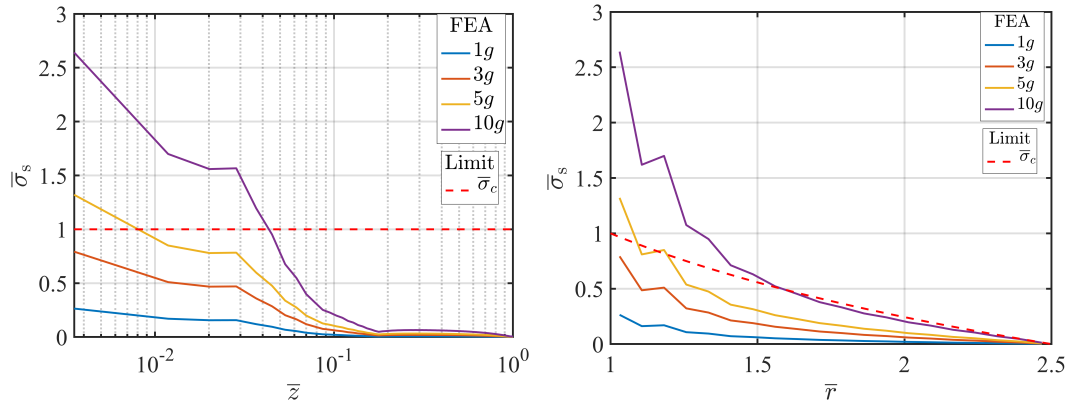
(a) Shear stress resultant distribution with axial position in roll.

(b) Shear stress resultant distribution with radial position in roll.

Figure 2.14: Shear resultant histogram by location in the coil under varying excitation levels.

In the axial direction, the maximum stresses are at the base of the structure (Fig. 2.14a). This is consistent with the initial analytical estimates, where the highest moments and shear stresses are at the base. In the radial direction, the maximum stresses are at the mandrel interface (Fig. 2.14b). These results confirm that the innermost layers, towards the root of the coil, are subject to the highest vibration induced shear stresses.

To identify the slip locations, the stress resultants' magnitudes can be assessed in comparison to the shear capacity. Whenever the stress curves exceed the red shear capacity limit lines in Fig. 2.14, slip is expected to occur. For magnitudes of excitation less than approximately $5g$, no slip is expected anywhere. This result indicates that there exist combinations of load, friction, and structural response configurations where modeling a coil as a homogenized solid may be considered a valid assumption. For a given loading, the extent of slip can be modulated by varying the coiling tension or the coefficient of friction between layers to raise or lower the shear capacity.

To more precisely pinpoint the slip locations, the stress components from the bottommost cross-section of the coil, which experiences the highest moments and shear, can be displayed. The contour plots in Fig. 2.15 depicts the magnitude of extracted stress components at the root of the coil due to $15g$ excitation, normalized by the maximum shear capacity.

Observe that the highest stresses for both components of shear are at the coil-mandrel interface and decay outwards. The maximum out-of-plane axial shear stress, σ_{rz},

(a) Out of plane shear components σ_{rz}.

(b) In plane shear components $\sigma_{r\theta}$.
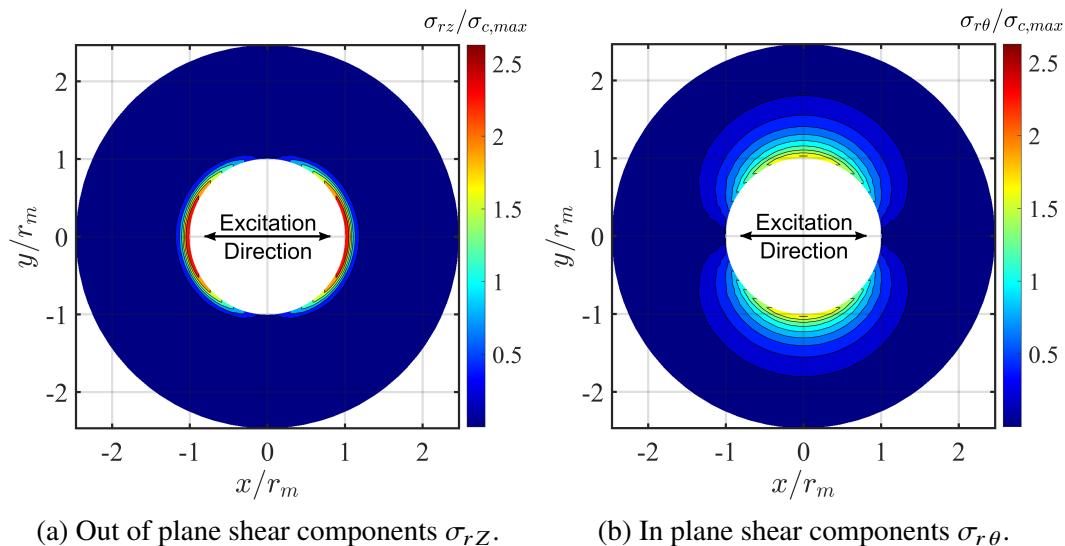
Figure 2.15: Contour plots of stress components at the bottom cross-section of the coil due to 15g sinusoidal loading.

shown in Fig. 2.15a is almost twice as large as the maximum in-plane shear stress, $\sigma_{r\theta}$ shown in Fig. 2.15b. This indicates that the bending mode of vibration is more significant for slip initiation than transverse shear. Despite this, the effect of transverse shear through $\sigma_{r\theta}$ extends for a larger radial distance in the coil, which indicates that a relatively larger number of layers are affected by in-plane shear due to vibration loading (Fig. 2.15b). These locations are consistent with the predictions from analytical estimates, which identified the surfaces aligned with the excitation direction as well as the neutral axis as locations of interest.

The FEA of the coiled-stiff model suggests that, despite exhibiting the highest inter-layer stresses and consequently the highest expected slip resistance, the innermost layers near the root are prone to slipping first. This result highlights these areas as locations of particular interest when evaluating slip in wound rolls, whether for engineering these surfaces to enhance slip damping performance or to prevent interlayer slip.

2.5 Experiment Design for Sensitivity to Coiling Tension

The findings of this section indicate two key results that are relevant for designing an experiment to study the vibration response of this damping concept. The first is that winding tension can have a significant effect on the vibration response of a wound roll, as measured with resonant frequency. The second is that the locations of slip are expected to initiate from a relatively small region. These results suggest that

the behaviors of this damping concept can be studied on a wound roll that contains relatively few number of windings.

For a small scale experimental study, a mandrel-coil assembly that is highly sensitive to coiling tension variation is desired in order to provide the largest disparity in resonant frequency of vibration. This allows for clear differentiation between the responses of 'loosely' and 'tightly' coiled states. The previous FEA framework is reused to repeat the sensitivity analysis of the vibration response performed in Section 2.4 to design a test sample for experiments.

For simplicity, the coiled material for this experiment was chosen to be 25 layers of continuous Kapton membrane. The number of layers selected here was motivated by considerations for subsequent experiments, and involved a compromise between opting for the minimum number of layers for convenience, while ensuring an adequate number of layers to capture interesting behaviors. The material properties of Kapton employed in the simulation are detailed in Table 2.5. In this study, the Kapton is assumed to be isotropic ($E_\theta = E_z$) and a range of in-plane moduli is considered to encompass the various reported values of Kapton properties [61–63]. As before, the radial stack modulus, E_r, was assumed to be 1% of the maximum in-plane moduli considered.

Table 2.5: Kapton Parameters

E_θ (GPa)	E_z (GPa)	E_r (GPa)	ν_{ij}	ρ_s (kg/m^3)	h (mm)
2.5–4.0	2.5–4.0	0.04	0.35	1400	0.05

Since the shear moduli are not directly measured, a range of values is considered up to the isotropic limit: $G_{r\theta} = G_{rz} = \frac{E}{2(1+\nu)}$ for $E_\theta = E_z = 4.0$ GPa. The disparity in resonant frequency, Δf, is defined as the difference between the natural frequency corresponding to the minimum value of shear moduli required to have a fundamental bending mode, and the natural frequency obtained with shear moduli equal to the isotropic limit.

In order to design this experiment, only the modal frequency extraction step of the coiled-stiff FEA model was reused to help choose a mandrel that would be most sensitive to changes in the winding tension of the selected membrane and number of windings. A range of mandrel materials and geometries was considered, and the most sensitive configurations corresponded to mandrels with lower modulus and thinner wall thickness. Selecting a mandrel of lower stiffness, closer to the stiffness

of the coiled material under test, and thinner wall thickness allows a limited number of windings to have a more pronounced effect.

Fig. 2.16 shows how the disparity in resonant frequency varies with mandrel radius and mandrel wall thickness for polycarbonate mandrels. This material was selected for its modulus, which is the most similar to that of Kapton among the materials considered. Fig. 2.16 also demonstrates that the frequency disparity increases with mandrel diameter. The significance of this result is that if the wound layers actually behave as a solid, the added layers from coiling effectively augment the thickness of the mandrel, resulting in increased stiffness. This suggests that the stiffening effect associated with the coiling scales with the size and stiffness of the structure being coiled. The geometry and material property used in simulation to design the mandrel are presented in Table 2.6. As a result of this design study, a polycarbonate mandrel was fabricated from stock material and sized to fit the physical extents and measurement bandwidth of the experimental test setup. The experiment is described in detail in the next chapter.
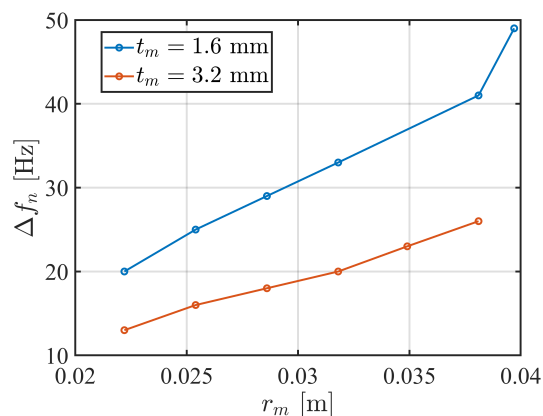
Figure 2.16: Expected wound roll resonant frequency disparity with mandrel radius and wall thickness for polycarbonate mandrels. Mandrels with larger radius and thinner wall thicknesses provide the largest expected disparity with winding tension.

Table 2.6: Mandrel simulation design geometry and properties

r_m (mm)	t_m (mm)	L (mm)	E_m (GPa)	ρ_m (kg/m^3)
40	1.6	300	2.7	1200

Fig. 2.17 shows the variation in resonant frequency with shear stiffness for the selected experimental configuration. Additionally, the resonant frequency of the mandrel by itself without the coil is plotted as well. Note that these results include a 0.05 kg tip mass that was added to the mandrel to bias the resonant frequency to a lower range.

The expected disparity between the loosest and tightest possible configurations is between $30 - 50$ Hz, depending on the actual modulus of Kapton. For effective shear stiffnesses below approximately 1 MPa, the resonant frequency of the roll assembly is lower than that of the mandrel by itself. This indicates that the roll does not provide significant stiffness to the assembly in low winding tension regimes, and behaves more as an added mass.

However, for sufficiently large values of shear stiffness, i.e., coiling tension, the resonant frequency of the wound roll assembly can exceed that of the mandrel alone. If this increase in stiffness is observed experimentally, this would demonstrate an advantageous property of this concept, where the geometric benefits of coiling are leveraged to provide stiffness to the system in addition to damping. The potential advantage is particularly exemplified by the choice of wound material here. In this application, this data suggests that the coiling process imparts structural integrity to the Kapton membrane, which, when unsupported, lacks the ability to withstand compression. However, coiling combines the influence of numerous layers to provide out-of-plane support for each layer in the roll. Consequently, the geometry of coiling is capable of turning even films into structural elements that contribute stiffness to the system, instead of merely adding non-structural mass.
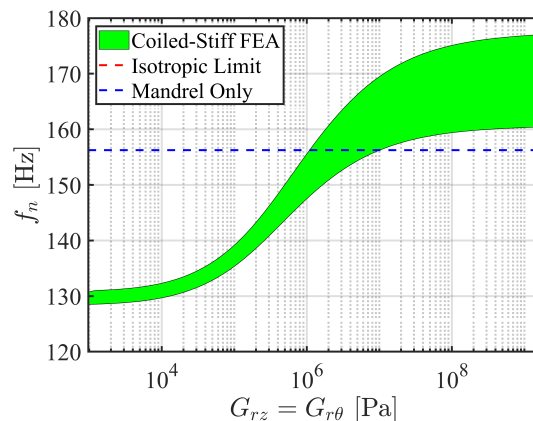
Figure 2.17: Variation in stiffness with shear stiffness (coiling tension). The shaded area corresponds to the uncertainty in the in-plane moduli of Kapton.

2.6   Conclusion

A method for estimating the slip resistance at any location in a tensioned, wound roll using shear capacity estimates derived from the interlayer stresses was presented. This methodology is demonstrated using an FEA model of a notional coiled structure supported by a cantilevered mandrel. The locations of maximum shear stresses from

FEA are consistent with expectations of elementary structural analysis, and indicate the locations where slip is expected to initiate from during vibration loading. If the vibration mode of a cantilevered wound roll structure is a bending mode, slip is expected to occur at the root, near the interface between the first wound layer and the mandrel.

Analyzing stress variations across different excitation levels indicates that there are combinations of friction properties, preloads, structure characteristics, and excitations where vibration stresses are projected to remain below the shear capacity everywhere in the wound roll. Consequently, in these instances, no slip is anticipated within the coil. This outcome suggests regimes where modeling the coil as a homogenized solid could be deemed a valid assumption. For a given structure configuration, increased excitation levels can cause the response to transition from 'no-slip' to 'slip'. This suggests a discriminatory behavior of this concept: 'activation' of this damping concept occurs selectively, responding only when necessary for sufficiently high loads.

Finally, the findings of this chapter suggest that an observable distinction in vibration response is expected between 'loosely' wound and 'tightly' wound rolls, as assessed through resonant frequency measurements, which is used as an indirect measurement of the effective stiffness of the wound roll. This implies a potential advantage of the wound roll damping concept: harnessing the geometric benefits of coiling for integral stiffness adjustment, offering a more scalable approach to vibration response mitigation. The results of this study are exploited in order to design a test sample for lab-scale experiments.

Chapter 3

WOUND ROLL VIBRATION EXPERIMENTS

3.1 Introduction

The slip prediction methodology discussed in the previous chapter provided an estimation of the slip locations inside a wound roll during vibration and the anticipated variation in vibration response with winding tension in the limit where no slip is expected. This was used to design a test sample that would, in theory, show high response sensitivity to winding tension for a limited number of wound layers. Using this test sample, two sets of experiments are performed to investigate the no-slip and slip regimes. The objective of these experiments is to understand the variation in vibration responses indicated by the initial findings of the previous section, as well as to determine the vibration reduction effectiveness of this damping concept.

No-slip Regime: Stiffness Variation

The simulation model used previously assumed that the notional structure in the coiled configuration behaved as a solid with an assumed value of shear moduli, G_{rz} and $G_{r\theta}$, which are related to the tightness of the winding. The utility of the vibration simulation results that indicate regions and load levels where slip occurs is contingent upon the validity of the coiled-stiff model in two aspects. First, that a non-continuous, layered solid that does not undergo slip can dynamically demonstrate the same behavior as a continuous solid. Second, that the range of variation in effective shear stiffness considered is achievable with realistic coiling tensions and contact interactions.

To confirm these two aspects in experiments, the variation in effective shear stiffness of the wound roll assembly with winding tension is measured indirectly using the fundamental frequency of vibration. For these experiments, the structure is intentionally excited at low amplitudes to bias the response of the wound roll towards the no-slip regime for the test structure and range of winding tensions achievable. If the span of fundamental frequencies of the coil system across a range of winding tensions matches that of an equivalently sized solid, then the treatment of the roll as a continuous solid can be considered valid.

Slip Regime: Damping Effectiveness

After studying the behavior of the wound roll damping concept in the no-slip regime, the response in slipping regimes can be studied to assess the damping efficacy. This is done by performing modal characterization of a wound roll assembly using a sine sweep test in order to determine how the frequency response of the test sample varies with winding tension. Damping is extracted from the experimental frequency response spectrum by using the half-power bandwidth method on the first peak acceleration response.

The performance of this damping concept is also characterized for additional types of loads, such as random vibration and impulsive shock loading. In many practical applications, loads experienced by materials or structures are not constant but vary randomly due to factors such as changing environmental conditions or operational variability. Thus, this set of experiments is performed to check how this damper operates in more realistic loading conditions, in order to assess excitation profile dependence.

Finally, to confirm that interlayer slip is the mechanism for energy dissipation, layer slip is measured experimentally. Comparing measured slip locations against simulated predictions is done to confirm understanding of how the vibration dynamics dictate the active regions within the coil for the wound roll damper concept. To measure slip, reference tracking targets are placed at several locations along the length of the mandrel. As a single, continuous membrane is wound around the structure, additional tracking targets are placed on alternating layers, concentric to the base reference targets. The wound roll is then excited using a sine dwell test at the natural frequency of the assembly, and a high speed camera captures the position of the tracking targets. Measurements are performed both axially and transverse to the axis of vibration. The high speed camera images are processed by identifying the centroids of the targets, where the difference between the layer target and the reference indicates slip relative to the base structure, and the difference between layer targets indicates interlayer slip.

3.2 Wound Roll Test Sample Preparation

Wound roll Test Sample Description

The vibration test sample consists of one continuous sheet of 2 mil thick Kapton®HN membrane, sufficiently long to wind 25 layers around the selected polycarbonate mandrel via a winding machine. The materials and geometry of this experiment

were chosen so that a relatively small amount of layers would have a sizeable impact on the structural response of the system. Note that the stiffness and mass of the constituent materials of the mandrel and membrane are approximately equal.

The mandrel consists of a polycarbonate tube, approximately 80 mm in diameter that is fitted with an aluminum mounting base at the root and with a plastic, 3D printed PLA spool end cap at the tip. The spool cap is epoxied into the mandrel at the tip, and the mandrel base is epoxied into the aluminum plate. The mandrel was sized so that the height of the mandrel extending past the 6 mm (1/4") thick aluminum plate was 300 mm (Fig. 3.1).

The plastic spool cap and the aluminum base have several functions. The aluminum plate has a mounting pattern for both the winding machine and vibration table. Both of the mandrel end features serve as spool flanges to ensure membrane alignment during winding and prevent excess axial shifts of the membrane due to slip. The spool cap also incorporates features to support the tip end of the mandrel during winding operations. Additionally, both end features also prevent ovalization of the tube during winding or vibration. Finally, the plastic spool cap also provides a tip mass to reduce the resonant frequency of the assembly to a range that can be more finely resolved by the measurement system and leads to more economical computation time for later simulations.

(a) Mandrel components and assembly.

(b) Mandrel dimensions and locations of mandrel fixed tracking targets.
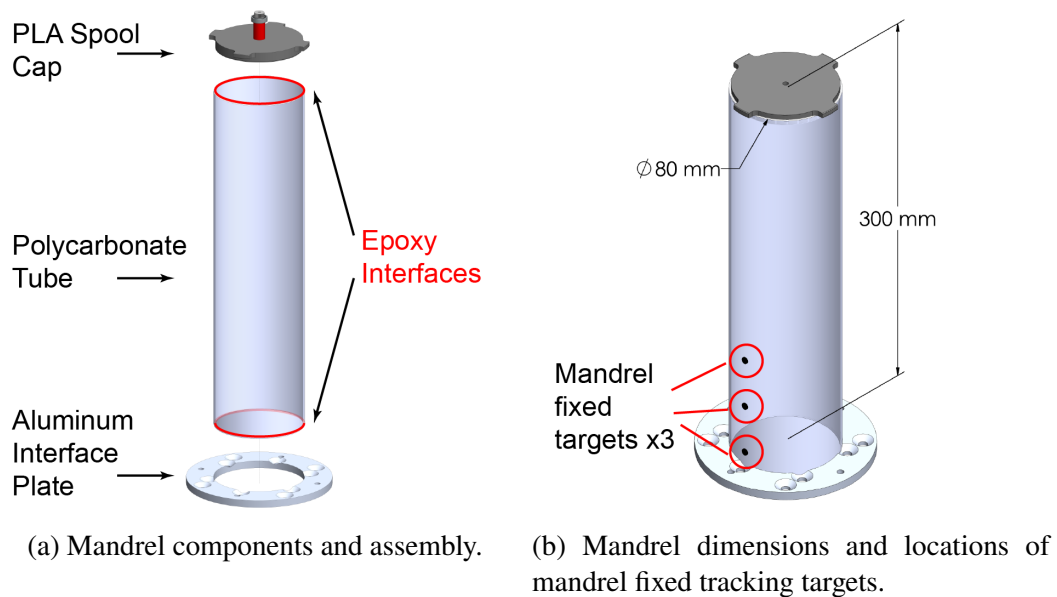
Figure 3.1: Mandrel components, construction, and dimensions.

Test Sample Assembly Procedure and Preload Measurement

A constant tension winding machine was built to perform the winding-rewinding operation. The machine consists of a center winding process that is driven by the rotation of the mandrel, where Kapton film is wound from the membrane roller onto the mandrel (Fig. 3.2). Both the mandrel and membrane roller are driven by brushed DC motors. The central motor is a GW600 DC 12V 10RPM motor with an integrated worm gear train, rated for approximately 12 Nm torque. The motor powering the membrane roller is a Maxon DCX22S motor with an integrated Maxon GPX22UP 186:1 planetary gearhead. The central winding motor operates under constant voltage (speed), and the membrane roller operates under constant current (torque). For this winding setup, the membrane roller is being backdriven, where the torque of the central winding motor overcomes the winding motor to unspool membrane from the roller with tension.
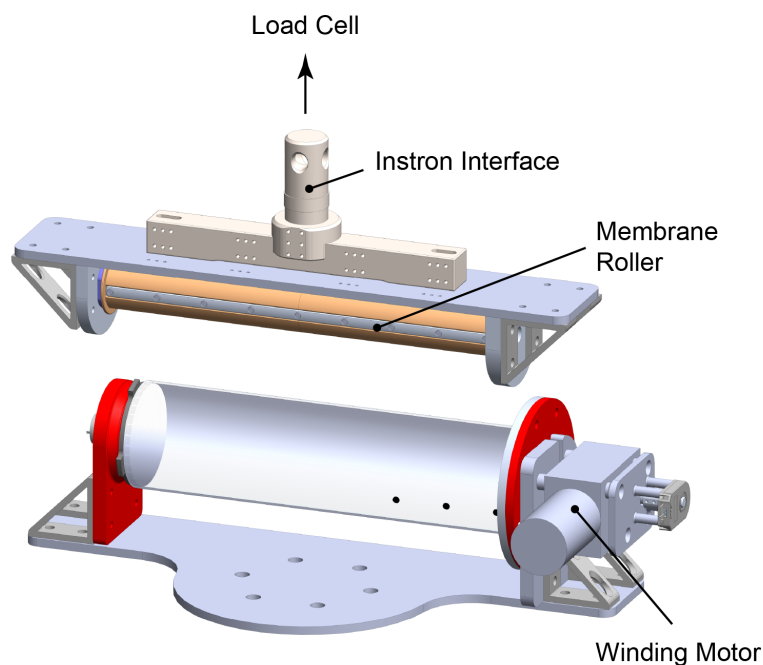
Figure 3.2: Constant tension winding machine. Winding is driven by the winding motor, which rotates the mandrel to unspool membrane from the membrane roller with tension. The membrane roller is attached to an Instron machine to measure winding tension via a load cell.

Before winding on the Kapton membrane, circular reference tracking targets are fixed to the mandrel surface at several locations near the base of the mandrel (Fig. 3.1b).

To start the winding process, one end of the membrane is attached to the mandrel

using tape (Fig. 3.3), and the membrane is then wound over the initial reference targets. During winding, circular ring targets are placed on subsequent alternating layers, concentric to the reference targets (Fig. 3.3, Fig. 3.4a). After coiling is complete, the free end of the membrane is fixed to the outer surface of the roll with tape (Fig. 3.3).

The tracking targets are made of masking tape, and are visible through the transparent mandrel and Kapton membrane when the wound roll is internally illuminated (Fig. 3.4b). The internal surface of the mandrel was covered with aluminized Mylar, which creates a mirrored surface that focuses the internal illumination onto a narrow section of the test sample containing the line of targets. This is done in order to increase signal strength during high speed camera measurements.
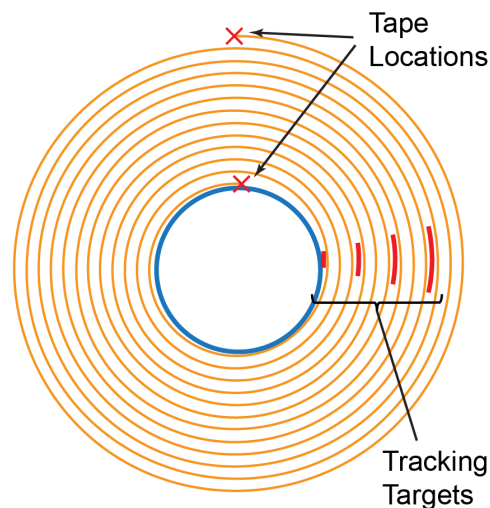
Figure 3.3: Kapton winding start/termination scheme with tape: leading edge fixed to mandrel, trailing edge fixed to roll outer surface. Mandrel and layer targets shown.

Initially, an attempt was made to directly measure the state of stress of the roll using Tekscan A-201 FSR flexible pressure sensors inserted at the beginning of winding at the mandrel interface, under the first layer (Fig. 3.5). Force Sensitive Resistors (FSR), are piezo-resistve elements that convert changes in force to changes in resistance. The changes in resistance are converted to a voltage using devices such as the voltage divider analog circuit module from the Tekscan FlexiForce Prototyping Kit in order to be read by a DAQ device. These sensors have seen successful use in measuring interlayer stresses in wound roll in previous studies [64].

However, it was observed that the response of the sensor was highly sensitive to the

(a) Polycarbonate mandrel with reference tracking targets and layer targets. Positions of layer targets not to scale.

(b) Layer tracking targets illuminated by internal light source.
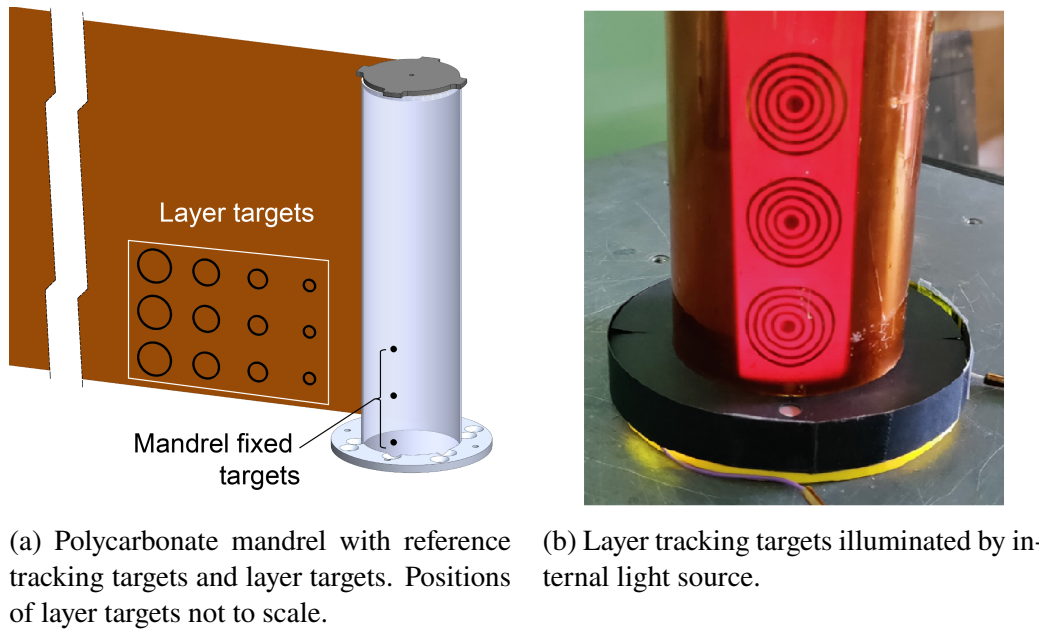
Figure 3.4: Wound roll damper test sample.
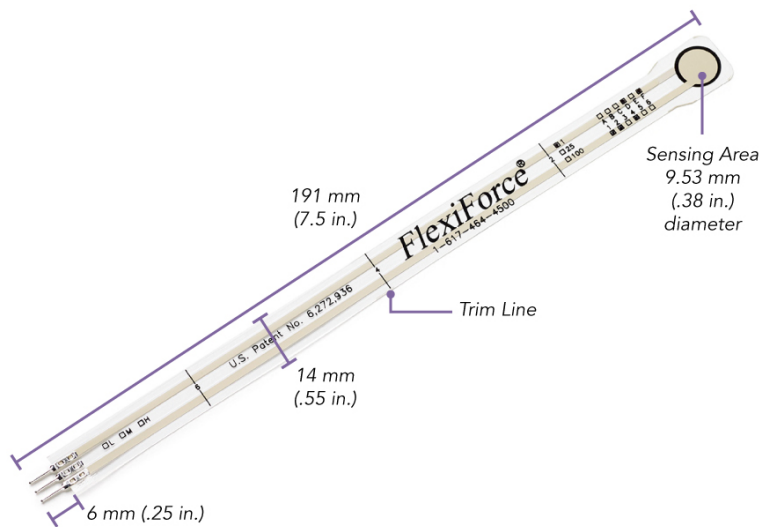
Figure 3.5: Tekscan A-201 FSR Sensor.

stiffness of the interface being compressed. Because different interface materials, especially more compliant ones, can affect results, it is generally recommended to calibrate the FSR and measurement system with setups that emulate the stiffnesses that will be experienced by the sensor in the measurement application [65]. In this particular case, the measured voltage and applied load calibration using an Instron testing machine did not appear to be consistent when the sensors were used on the much more compliant interface of the hollow cylindrical mandrel-Kapton layer system. Unfortunately, attaining in situ calibration within the wound roll poses

a challenge, given the absence of a clear method that avoids interfering with the measurement.

The responsiveness of the sensor was capable of distinguishing between different preload levels in a relative sense, but consistent knowledge of the absolute preload was not obtainable in this setup. There are other methods of measuring interlayer stresses of a wound roll, both indirect and direct, such as pull tabs, roll hardness testers, and acoustic testing, however these were deemed infeasible for the low number of layers in this particular experiment [48, 49].

As such, the winding tension was directly monitored using an in-line force sensing load cell (Fig. 3.2). In order to achieve both approximately constant tension over the entire winding process and maximum tension differentiation between membrane roller current setpoints, the central winding motor voltage was set to 6 V. The membrane roller motor voltage was held constant at 10 V, and the winding current was varied from 0 mA to 1000 mA. For the 0 mA case, the membrane roller was not only unpowered, but was also unplugged, which removed the braking effect due to back EMF so that only a minimal amount of load is applied to the membrane through backdriving the membrane motors' gearbox. Fig. 3.6 shows the characterization study that was used to select these operating points. Setting the winding motor voltage to 6V achieves the best performance in delineating the measured in line tension between roller current settings.

The coiled roll was assembled using a range of different membrane roller currents using this winding process, and resulted are parameterized by the measured winding tension.

3.3   Vibration Experiment Setup and Test Procedure

The preloaded, coiled assembly was then placed on a vibration table, and a retro-reflective tracking marker was placed at the tip of the assembled roll as well as on the shaker head as depicted in Fig. 3.7. The retroreflective tracking markers were used in concert with a Polytec PSV-500 Laser Scanning Vibrometer, which provided a non-contact measurement method that was preferable over accelerometers to avoid affecting the vibration response.

Vibration Response Experiment Procedure

The vibrometer was used to control the vibration table in order to study the behavior of the wound roll under different excitation profiles. Sine sweep was the primary
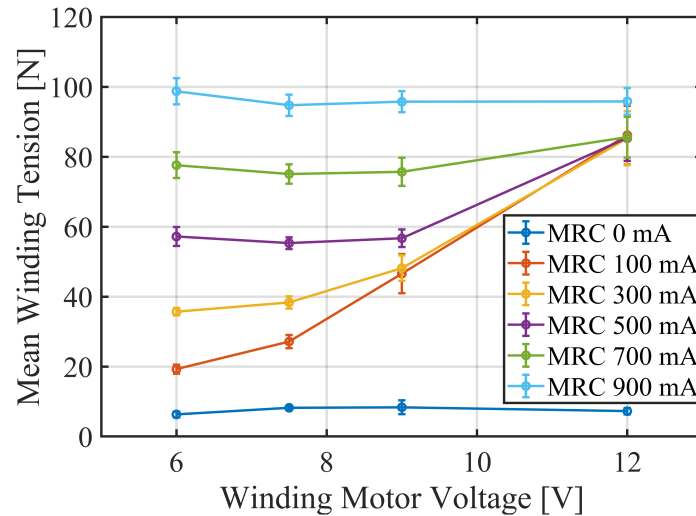
Figure 3.6: Measured winding tension variation with winding motor voltage (winding speed) and membrane roller current (MRC ~ tension). Error bars comprise both the variability observed across three trials and the within-trial variations. Most clear tension delineation between MRC setpoints and consistent mean winding tensions with the winding motor operating at 6 V.
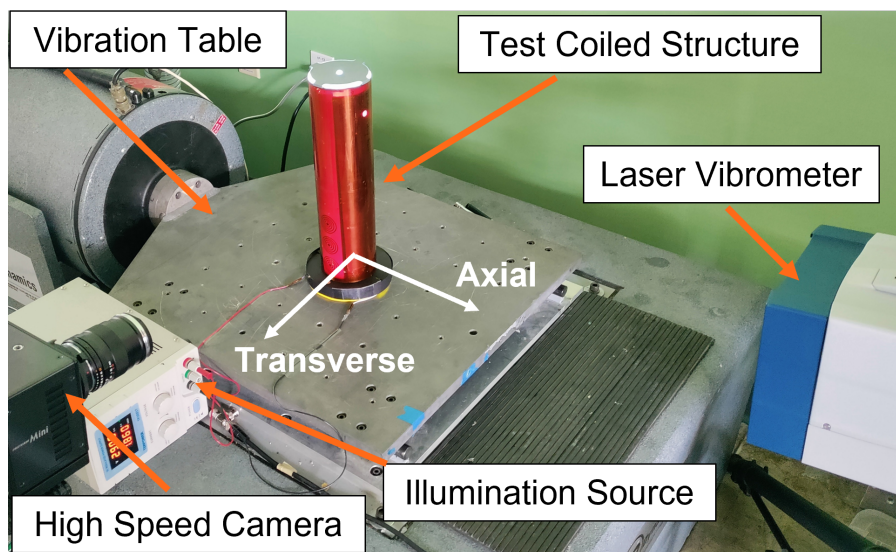
Figure 3.7: Vibration experiment of a wound roll.

excitation profile used for measurement of wound roll response and performance characterization using the metrics of damping and resonant frequency. The other profiles used in this experiment, including sine dwell, random, and shock, are used because they reflect more realistic loading cases. The sweep is run from 5 to 300 Hz for a 45 second duration. The chosen frequency range was selected to encompass the resonant frequency of the mandrel by itself ($f_{n,mandrel} \approx 150$ Hz), and any potential

frequency shifts with winding tension indicated in the previous chapter. Notably, this corresponds to a relatively fast sweep rate ($R \approx 8$ oct/min), which initially raised some concerns about affecting the modal response.

In sine sweep vibration simulations of single degree of freedom (1-DoF) models, the sweep rate is observed to potentially impact estimates of the resonant frequency and damping, causing them to deviate from the steady state response [66]. Experimentally, the effect of sweep rate was explored, but did not appear to impact estimates significantly. An explanation for this observation is that sufficiently damped systems are relatively insensitive to sweep rate. Fig. 3.8 demonstrates the permissible exponential sweep rate, normalized by the resonant frequency, for the response of a 1-DoF system to approach 90% of the expected steady state response as a function of the damping in the system [67]. Fig. 3.8 indicates that, even for modest levels of damping, if the resonant frequency is sufficiently high, the system can support a relatively high sweep rate without significantly affecting the response.
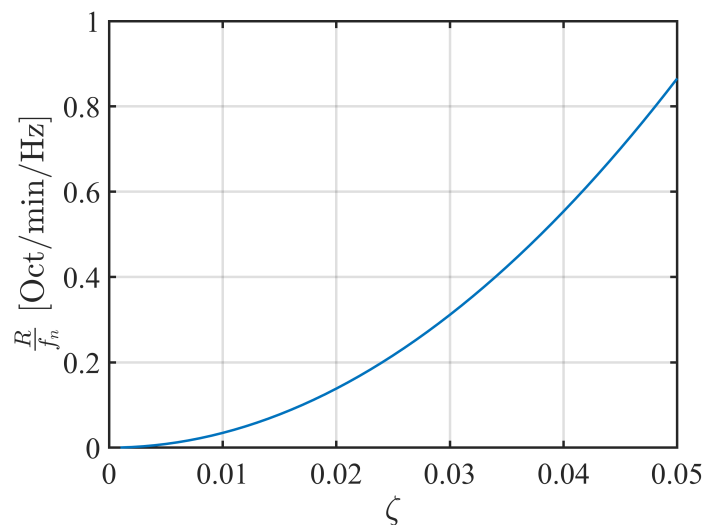
Figure 3.8: Maximum sweep rate, R, normalized by natural frequency, f_n, for 1-DoF swept response level to approach 90% of steady state response.

A more stringent constraint that determined the sweep rate for this experiment was the sampling duration set by two settings on the Polytec Vibrometer software: the number of FFT lines and measurement bandwidth. The selected sweep rate was a compromise to get as high of an FFT sampling resolution possible to get good frequency response resolution while ensuring that the sampling duration covered the entire excitation duration. As a contingency, the vibration responses obtained from non-harmonic loading types like random and shock provide additional data,

unaffected by sweep rate, to corroborate observed trends and behaviors observed under sinusoidal loading.

In all test cases, the acceleration spectrum of the tip tracking marker and the vibration table shaker head marker are recorded in order to provide acceleration transmissibility response curves. Damping is estimated from the experimental transmissibility spectrum by using the half-power bandwidth method on the first peak acceleration response, which corresponds to the natural frequency of the wound configuration (Fig. 3.9):

$$\zeta = \frac{1}{2} \frac{\Delta f_{3dB}}{f_n} \tag{3.1}$$

Before each test, a low level sine sweep is performed to characterize the initial behavior of the wound roll. This characterization is repeated at the end of testing to ensure that no damage has occurred to the roll. In general, outside of cases where damage to the test sample was confirmed, no significant variation between pre-testing and post-testing responses was observed.
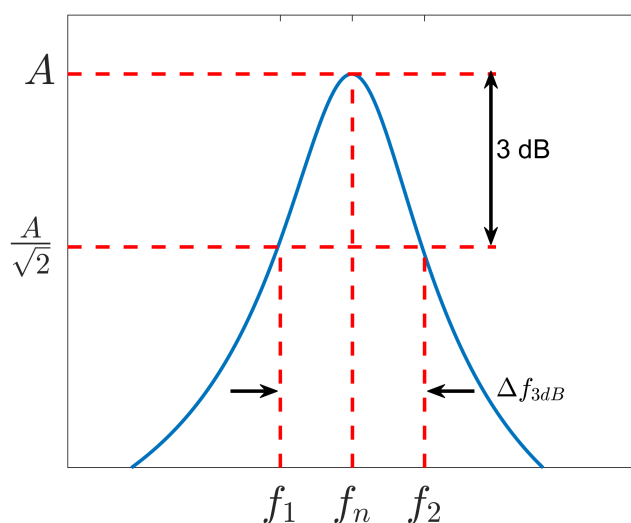
Figure 3.9: Half-Power '3 dB' Method to estimate damping from transmissibility.

3.4 Vibration Experiment Results

Vibration Response in No-slip Regime

The fundamental frequency of the wound roll assembled under different winding tensions was recorded for a range of excitation levels using random excitation. In this set of experiments, random excitation was selected for efficiency in quickly measuring the response of a test configuration under varying excitation levels and in order to make consistent comparisons. Random vibration excites all modes within

the selected spectrum simultaneously, eliminating the need to perform a sine sweep for each tension and excitation level configuration to determine whether a resonant frequency shift had occurred. As amplitudes are also random, the responses are subsequently time-averaged to obtain the mean response before comparison.

The recorded resonant frequency is plotted against the measured tip acceleration and is shown in Fig. 3.10. In addition, the vibration response of the mandrel by itself, excluding the wound roll, is depicted. The figure includes an overlay of the coiled-stiff FEA model's predictions in green, specifically for frequencies surpassing the mandrel-only response.

For this study, two sets of wound roll response data are presented in Fig. 3.10, corresponding to different interlayer surface treatments. The first, corresponds to bare, uncoated Kapton, which is considered the baseline case. The second set of data corresponds to a Kapton roll that has been treated with temporary spray adhesive (Sulky KK2000) to increase the coefficient of friction, which is intended to illustrate the effect of varying the interlayer contact properties. The investigation of treated Kapton is only performed in this set of experiments. All other investigations discussed in later sections study untreated Kapton.
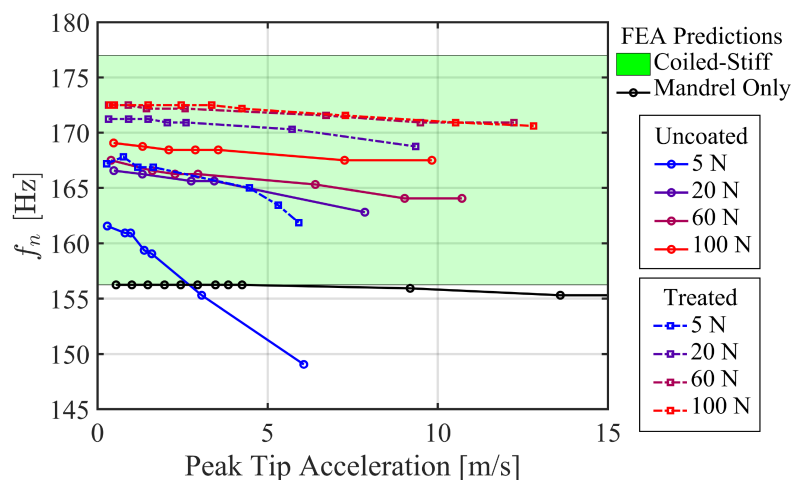
Figure 3.10: Resonant frequency variation of wound roll with winding pretension and contact properties.

Looking at the mandrel-only system, note that the stiffness is approximately constant, irrespective of excitation level. This demonstrates that the mandrel fixture will provide a useful baseline comparison, and any deviation in vibration behavior results from the contribution of the wound roll.

For the wound roll data with uncoated Kapton, the resonant frequency of the wound roll increases with winding tension. Furthermore, the span of measured resonant frequencies is well within the expected range predicted from the coiled-stiff assumption, demonstrating the utility of the FEA model. The shifts in resonant frequency indicate that the roll can provide meaningful adjustment to the effective stiffness of the overall assembly with winding tension.

While the mandrel-only resonant frequency was invariant with the excitation level, the coil-mandrel assembly natural frequency tends to decrease with increasing acceleration. However, increasing winding tension reduces the sensitivity to the excitation level. Despite the reduction in effective stiffness with higher excitation, the assemblies wound at larger tensions maintain a higher fundamental frequency than the unloaded mandrel by itself, indicating that the coil windings are providing structural support. This is in contrast to the most loosely wound case, where the resonant frequency similarly started above the mandrel-only response. However, for sufficiently large acceleration, the assembly stiffness decreases below the mandrel-only level, behaving more like an added mass. The most probable explanation for the response variation is the degree of interlayer slip, where the most loosely wound case studied here experiences greater extents of slip for the same excitation levels.

For the wound roll data with modified contact properties, the response differentiation between winding tension variation is decreased. For the same range of winding preload and excitation levels, the wound roll data with treated Kapton demonstrates stiffer responses, characterized by higher frequencies. Additionally, there appears to be a saturation effect, where there is no significant variation in response after a critical preload level. The maximum recorded resonant frequency of the test cases with increased interlayer friction remains within the predicted frequency range of the coiled-stiff model. This indicates that the isotropic limit used in the coiled-stiff FEA model is a useful upper bound.

The results of this experiment suggest that the simplification of treating a tightly wound roll as a continuous solid is a useful approximation, but its applicability may be limited when excitation levels are sufficiently high to cause significant interlayer slip. The critical load level may be controlled by modifying the winding tension or the contact properties between layers. Moreover, this experiment validates the idea that wound rolls can provide substantial stiffness modification with winding tension.

Vibration Response in Slip Regimes

Sine Sweep: Vibration Response Characterization

For the next set of experiments, the vibration response of wound rolls in slipping regimes is studied to assess damping characteristics. Here, an exponential sine sweep is used to obtain the frequency response spectrum. For this set of tests, the excitation amplitude is fixed and the target input acceleration at base was chosen to be 5 m/s^2 (approximately $0.5g$), which is a typical amplitude for experimental modal characterization.

The frequency responses of the wound roll with different winding tensions are shown in Fig. 3.11a. The natural frequency, f_n and damping estimate, ζ, are extracted from each curve. The damping of the wound roll plotted against the measured natural frequency of the wound roll is shown in Fig. 3.11b. The response and damping of the mandrel by itself is also shown in these figures.

From these plots, there appears to be an approximately bimodal response between 'loosely' wound and 'tightly' cases for the range of winding tensions studied. For low winding tensions, the response curves demonstrate a positive skew, which reduces as tension increases. On average, significant variations in winding tension yield clearly distinguishable responses. However, it is important to acknowledge that there is variability in discerning responses by winding tension magnitude. As illustrated by the scatter in Fig. 3.11b, for the same apparent winding tension, the vibration response is not necessarily consistent and variations are not necessarily monotonic with winding tension. Additionally, with the specified sample preparation procedure and excitation level, the vibration response appears to tend towards saturation at either extremes of winding tension levels. Regardless of how loosely the structure is wound below approximately 20 N winding tension, there is no additional variation in response. Similarly, for tightly wound structures, after approximately 50 N tension, no further significant variation in response is achieved with increasing tension.

A possible explanation for the response saturation is that the degree of interlayer slip for the tested configurations has reached a limiting value. At a constant excitation level for these test cases, the extent of interlayer slip can only propagate so far when wound loosely or be constrained so much when wound tightly. This idea is explored in later experiments when a larger range of excitation levels is considered. Another likely explanation is the variability in the winding process during the assembly of test samples and challenges in precisely controlling incremental changes in winding tension from one test to another. Despite this limitation, the difference in stiffness,
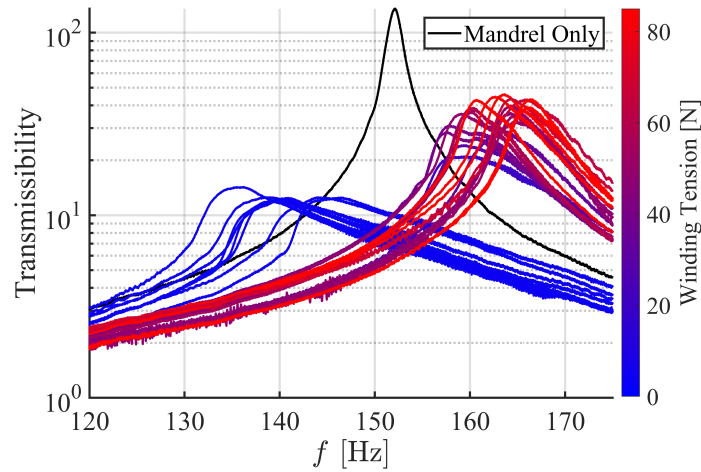
(a) Transmissibility response spectrum.
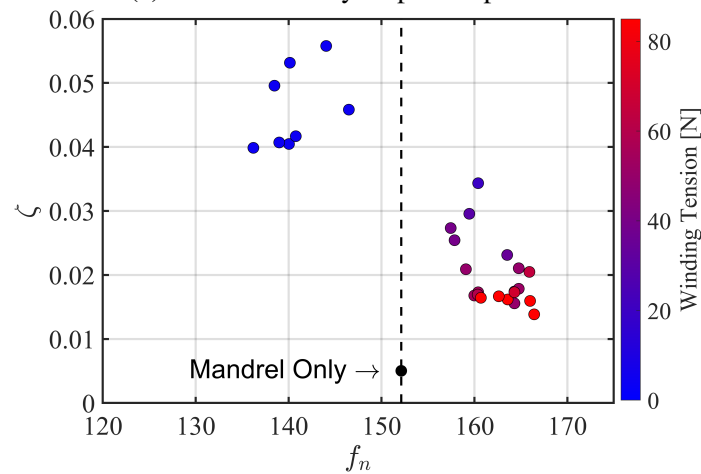
(b) Damping variation with winding tension.

Figure 3.11: Wound roll damper frequency response and damping variation.

amplitude of response, and damping are large enough between 'loosely wound' and 'tightly' wound configurations that conclusive statements can be drawn.

For configurations wound at lower winding tensions, the assembly exhibits reduced stiffness and significantly increased damping relative to the response of the mandrel by itself. The penalty in reduced stiffness in exchange for increased in damping observed in the highest damped configurations is comparatively small for this assembly, as the observed natural frequency was reduced by only approximately 10%. Conversely, more tightly wound cases demonstrate increased stiffness and comparatively less damping than more loosely wound roll. An approximately 5–10% increase in resonant frequency was observed for the stiffest configurations observed.

In general, increasing the winding tension during the coiling process results in an

overall increased stiffness for the final wound roll, but corresponds with decreasing damping. However, regardless of the winding tension, the addition of the wound roll has increased the overall damping of the assembly. The estimated range of critical damping for the wound roll assembly ranges between 1% and 5%, marking an increase from the mandrel-only result of approximately 0.5%. These results confirm the potential of the wound roll damping concept, which utilizes the wound roll as an energy dissipation mechanism.

Random Vibration: Performance Variation with Excitation Level

The vibration response of a wound roll is determined by the coupled interactions between the preload, structure, and excitation. While there were challenges in controlling preload increments to achieve smooth variation, as described in the previous section, the excitation levels could be continuously varied. This provides an opportunity to not only examine the sensitivity of the response to changes in excitation level, but also determine whether the bimodal response observed previously is a real effect. In this set of experiments, the excitation profile reverts to random vibration, with the focus now on investigating a significantly broader range of excitation levels.

Fig. 3.12 shows the vibration response variation between three test cases for varying levels of random vibration excitation: the mandrel by itself, and the wound roll for two levels of winding tension: 20 N and 60 N. In each of the plots in Fig. 3.12, the excitation magnitude labeling is normalized by the maximum level. As previously mentioned, responses to random excitation are obtained by time-averaging to establish the mean response before conducting comparisons. Unlike the sine sweep data, the vibration responses with excitation level do not exhibit the bimodal grouping and have a comparatively smoother transition with excitation level. This indicates that the bimodal response distribution observed in the sine sweep data is most likely an artifact of the sample preparation process, and not a physical mechanism of wound roll damping.

The damping ratios are extracted and plotted versus normalized excitation level in Fig. 3.13 to facilitate more straightforward comparisons. Note that these values are not meant to be compared with the damping estimates reported from sine sweeps, which is typically how these values are conventionally obtained. Instead, they are utilized as an accessible metric that captures the amplitude and width of response peaks for relative comparisons.

Fig. 3.12a shows the mandrel-only response. Here, transmissibility is observed to be
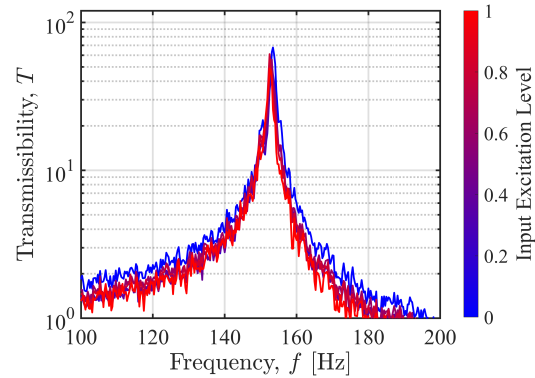
(a) Mandrel-only
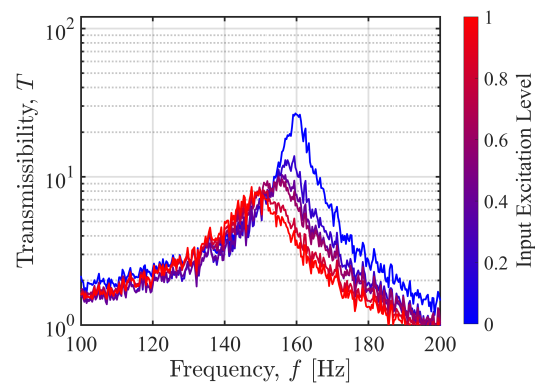
(b) 20 N winding tension
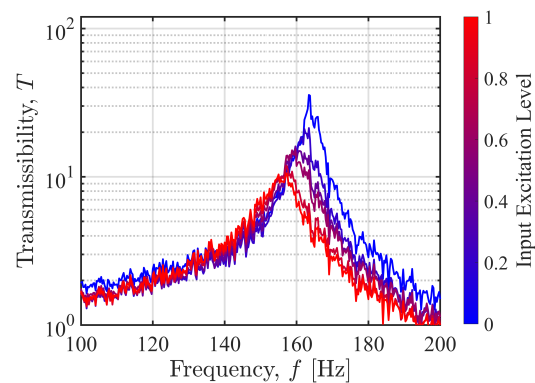
(c) 60 N winding tension

Figure 3.12: Variation in transmissibility with excitation amplitude for random vibration of the wound roll under different winding tensions.

invariant to excitation amplitude (Fig. 3.13). This demonstrates that any subsequent variations in response after including the wound roll are not attributed to the mandrel.

Fig. 3.12b shows a wound roll test case for the lowest winding tension in this experiment set. The wound roll vibration performance is consistent with previous findings;
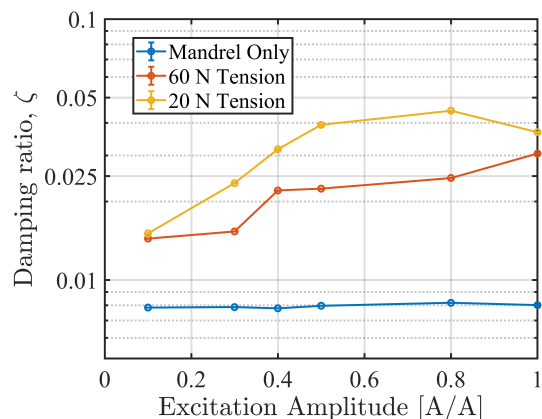
Figure 3.13: Wound roll damping variation with excitation amplitude and winding tension.

regardless of excitation amplitude, the wound roll shows decreased response, and therefore higher damping in all cases relative to the mandrel-only response. As the excitation level increases, the resonant frequency of the wound roll decreases and the damping level increases, as demonstrated by the positive slope in the damping response depicted in Fig. 3.13. This indicates a discriminatory, self-scaling feature of this damping concept. For low amplitudes of excitation, the wound roll exhibits a stiffer response to loading. As the excitation level increases, more layers within the roll slip, which increases dissipation and results in higher damping. This added damping is achieved at a relatively minimal cost, as the resonant frequency undergoes only a marginal change, i.e., approximately 5%.

Fig. 3.12c illustrates how the response varies with increasing winding tension, which further substantiates that the observed phenomena result from the influence of interlayer slip within the coil. Similar to the lower tension case, the wound roll still demonstrates higher damping than the mandrel alone, even with higher winding tension. However, as expected, lower damping is achieved and the range of resonant frequencies is higher, indicating that the higher tension winding demonstrates a stiffer response due to reduced slip (Fig. 3.13).

Shock Loading: Performance Under Impulsive Loads

The final excitation profile in this set of experiments is shock loading. Some traditional damping concepts draw criticism for their inability to respond to impulsive loading without response delay or have loading rate dependent behavior, which may lead to the direct transmission of loads. Therefore, the aim of this experiment is to assess the performance of this concept under shock excitation, which subjects the

wound roll to impulsive, high loading rates. The shock profile used in this study was extracted from a spacecraft qualification test campaign, and is shown in Fig. 3.14 for completeness. Nominally, this profile is intended to specify excitation levels for frequency content up to 5000 Hz, but the primary objective of this profile is simply to subject the test sample to impulsive loads, so no effort is made to ensure the table response matches the original shock response spectrum. This profile was normalized into a voltage signal, and then passed into the vibration table controller.
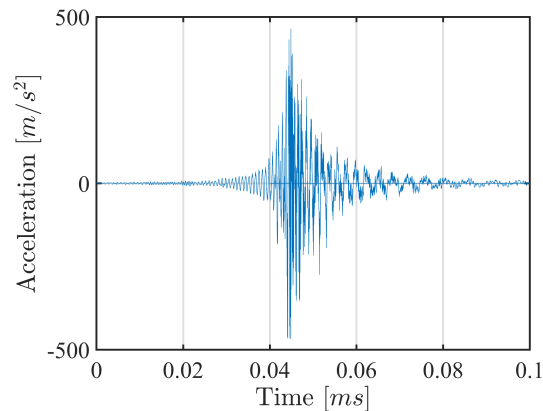
Figure 3.14: Shock time series used to convert into voltage time series input into vibration table.

Fig. 3.15 shows the variation in wound roll response to shock excitation. Immediately apparent is the difference in damping between the mandrel-only case and the wound roll cases. For the mandrel-only case, low damping is evident as indicated by the response exhibiting the highest amplitude and the slowest decay rate, where the mandrel exhibits ringing for an extended duration. This is in contrast with the wound roll test cases, where the response decays much more quickly.
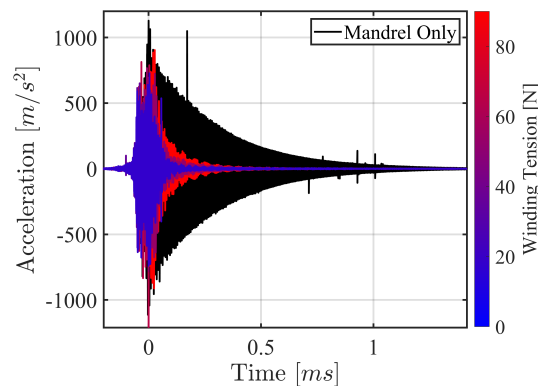
Figure 3.15: Wound roll damper shock response time domain data.

While one might be tempted to attempt to calculate the damping ratio from this

data using the logarithmic decrement, the nature of the data does not lend itself well to this technique. For the mandrel-only response, the logarithmic decrement technique is easy to calculate because there is a single dominant frequency and the exponentially decaying envelope is well-defined and consistent. However, for the wound roll dataset, there are numerous spurious signals that make defining a consistent decay envelope difficult and multiple frequency components with no dominant peak frequency. Instead, the frequency responses can be extracted using the FFT as shown in Fig. 3.16. Note that each of these curves is the averaged response obtained from three separate trials.
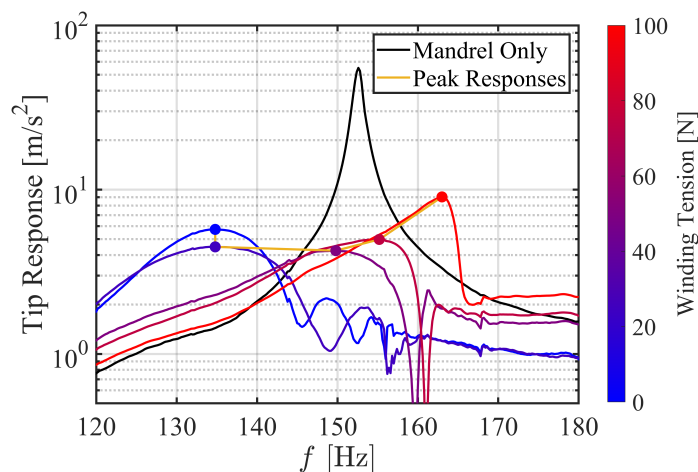
Figure 3.16: Extracted peak acceleration variation with winding tension from shock response.

Note that the overall shape of the wound roll responses obtained from shock loading are significantly different from those obtained from the sine sweep experiments. The disparity between the frequency responses obtained from shock data and sine sweep data can be attributed to the distinct nature of these input signals. Shock data subjects the test sample to impulsive force inputs, leading to a frequency response that reflects the system's response to loading rate. In contrast, sine sweep data involves a continuous and smoothly varying input signal that sweeps through a range of frequencies, providing a more comprehensive view of the system's behavior across different frequency components. The abrupt nature of shocks can excite specific resonances and dynamic characteristics of the system that may not be as prominent or easily discernible during a sine sweep. Additionally, shock events may induce nonlinear behavior in the system, further contributing to differences in the frequency response compared to the linear and continuous excitation provided by a sine sweep.

The responses in Fig. 3.16 generally demonstrate behaviors consistent with the previous excitation profile experiments. As winding tension increases, the frequency of the peak response increases, indicating stiffer behavior that can exceeding the stiffness of the unloaded mandrel for sufficiently high tension. Additionally, irrespective of the winding tension, the presence of the wound roll damper consistently reduces the vibration response where all wound roll responses show lower tip response than the mandrel-only case.

A notable observation is that the configuration with the lowest winding tension does not necessarily exhibit the most damped response. An indication of this property was potentially hinted at in the sine sweep data in Fig. 3.11a, where the response with the lowest resonant frequency did not have the lowest peak response in the dataset. This is an indication that there exists an optimal value of winding tension for peak damping, which is a known property of friction dampers, where frictional energy dissipation is optimizable [68]. Further discussion of this topic will be addressed in upcoming chapters dedicated to FEA, where the magnitude of energy dissipation can be extracted directly.

3.5   Interlayer Slip Measurement Experiment
Layer Slip Measurement Procedure

Having now examined the vibration response and performance of the wound roll damper, the objective of the remaining experiments focus on confirming the underlying mechanism for energy dissipation is, in fact, layer slip. In order to demonstrate this, the approach is to correlate damping levels with direct measurements of layer slip to pinpoint locations exhibiting the highest slip magnitude.

This experiment is performed for two test cases with different winding tensions, using a sine dwell at the resonant frequency of each configuration. During each test, an internal illumination source mounted underneath the test sample is turned on, allowing a high speed camera to record the tracking targets during the vibration experiment at 2000 fps (Fig. 3.4b). The slip measurement for each of the two tension levels tested is performed twice: once with the camera viewing direction aligned axially to the excitation direction and once in the transverse direction (Fig. 3.7). Axial measurement refers to the surface with the normal aligned in the excitation direction, while transverse measurement applies to surfaces with the normal oriented orthogonally to the excitation direction (Fig. 3.17). Because the tracking targets are placed only along one longitudinal line along the test sample to keep the targets

centered in the camera image frame to minimize the effect of distortion, the wound roll and the high speed camera position must be rotated for each viewing direction.
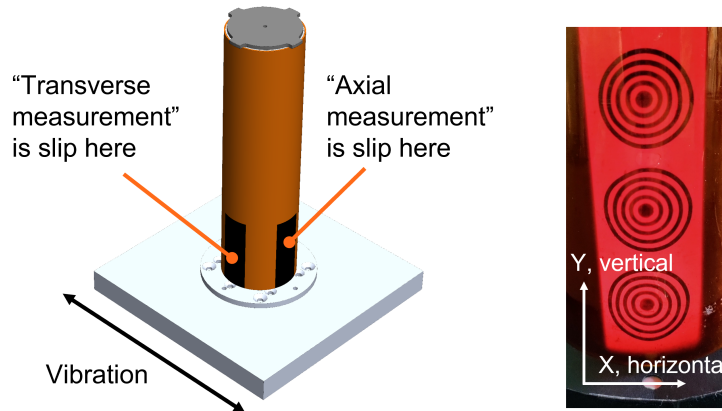
Figure 3.17: Slip measurement location and direction conventions.

Images from the high speed camera were exported onto a personal computer and processed using MATLAB. Each frame was thresholded to create a grayscale image of binary values. The targets in the processed image are identified by the number of connected pixels, as well as their circularity and diameter. Once successfully identified, the centroids of each target, measured in the image coordinate frame (x, y), were stored. A centroid based tracking scheme was found to be more robust compared to an edge detection scheme, which was highly sensitive to imaging noise resulting from high frame rate imaging that measured low signal-to-noise due to lower exposure time. Fig. 3.18 shows an example processed image that indicates the accuracy of the centroid tracking scheme for one particular image.

The targets at a given longitudinal position are denoted as Group i. The targets on a given layer are denoted with Layer j. For a given target Group i, subtracting the position of the reference target, $(x_r, y_r)_i$ from the position of the layer targets $(x, y)_i^j$ eliminates the contribution of the mandrel movement. The resultant is the slip of layer j, $(s_x, s_y)_i^j$, relative to the mandrel:

$$(s_x, s_y)_i^j = (x_r, y_r)_i - (x, y)_i^j \tag{3.2}$$

Interlayer slip can then be computed by taking the difference between layers:

$$(s_x, s_y)_i^{j_1 - j_2} = (s_x, s_y)_i^{j_1} - (s_x, s_y)_i^{j_2} \tag{3.3}$$
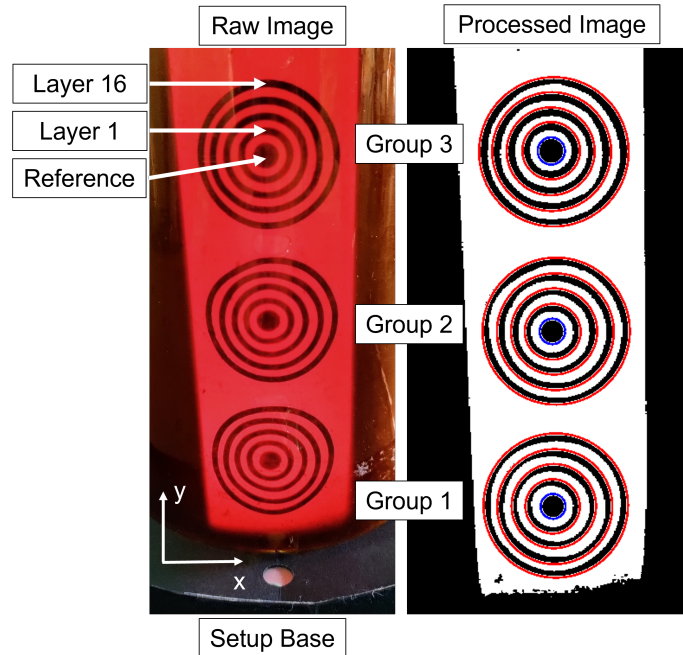
Figure 3.18: Example processed image showing centroid tracking scheme. Here, layer targets were placed every five layers starting from Layer 1 (Layers 1, 6, 11, 16).

Note that the slip calculations in Eq. (3.2) and Eq. (3.3) are performed in the time domain and the units are in pixels.

The noise floor of the measurement and processing chain was evaluated by applying the entire procedure to the sample measured at rest. High frequency noise present in the statically measured centroids in the time domain (Fig. 3.19a), motivated performing analysis in the frequency domain and only considering a neighborhood around the excitation frequency that was tested experimentally (Fig. 3.19b).

This was done by taking the Fourier Transform of the time domain signals, which was a preferred method over directly filtering or smoothing the time domain data to avoid impacting the slip measurement. From this, the maximum uncertainty in the position of the targets measured statically in the frequency band of interest was found to be $\delta = \max(\delta_x) = \max(\delta_y) \approx 0.01$ px. Since slip is calculated from the difference of two uncertain measurements, the propagation of uncertainty results in a total slip noise floor of $\delta_s = \sqrt{2}\delta \approx 0.02$ px. Slip magnitudes at least δ_s above the noise floor would be considered as a real signal, whereas values below this threshold would be considered indistinguishable from the static, no slip condition. As a result, after first performing slip calculations in the time domain, the results are converted
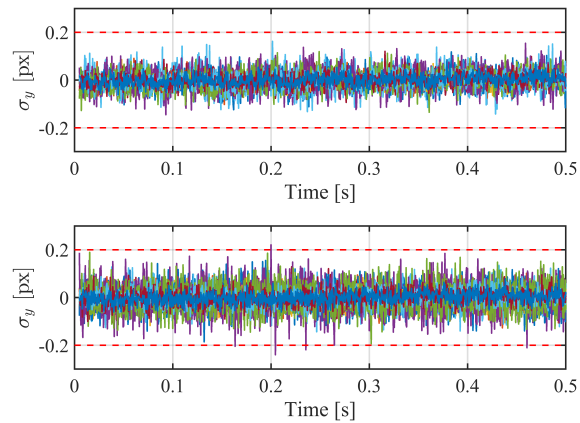
(a) Time domain centroid locations.
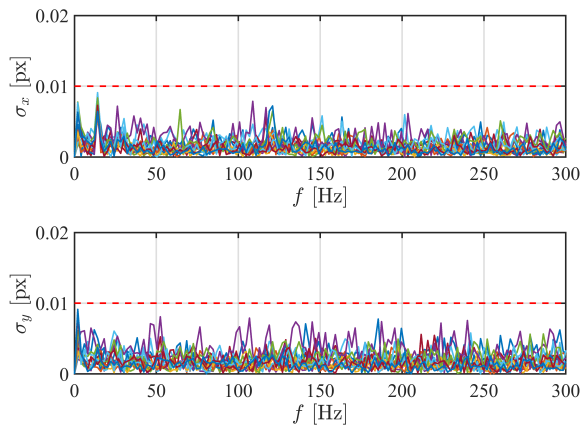
(b) Frequency domain centroid locations in frequency band of interest

Figure 3.19: Noise floor (red dashed line) estimation of measurement and centroid tracking processing chain of all 15 targets measured statically. Frequency domain noise floor lower than time domain noise floor by an order of magnitude.

into the frequency domain for evaluation. The dimensions of the targets are known and can be used to convert from pixel units to mm. The conversion is approximately 0.1 mm/px.

Slip Experiment Results

Fig. 3.20 shows an overview of all slip measurements, where the maximum, mandrel relative slip, in any direction (x, y) at any layer, $\max_{j}[(s_x, s_y)_i^j]$, is plotted against the target groupings for both axial and transverse measurements. In this figure, the error bar corresponds to the uncertainty of the measurement, δ_s. The red dashed line in this plot corresponds to the noise floor. The black dashed line shows the

maximum slip, considering only the x direction, s_x. This is included to gauge the relative magnitudes between s_x and s_y.
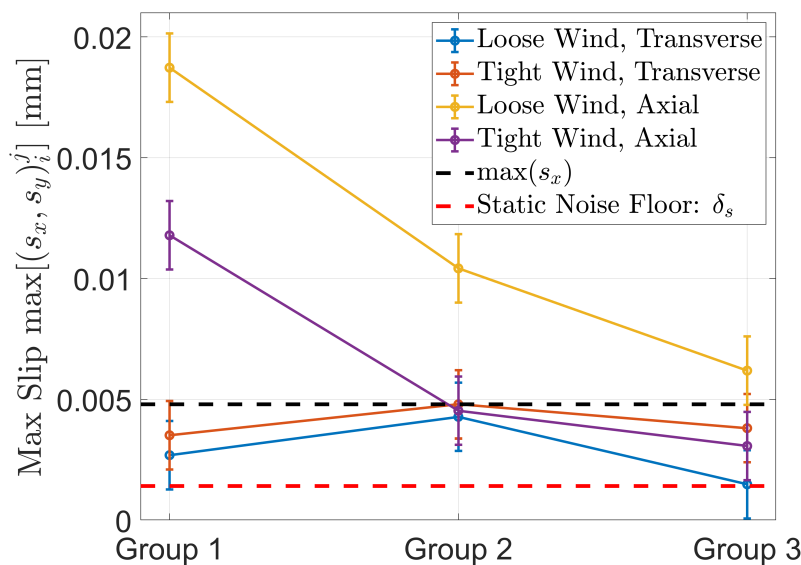
Figure 3.20: Aggregate mandrel relative slip: maximum of vertical and horizontal slip at any layer for axial and transverse measurements.

In examining the data, the scale of slip is noted to be well under 1 mm in amplitude, which is less than 0.01% of the length of the wound roll assembly. This experiment is conducted at the natural frequency of the system, representing conditions where maximum stresses are anticipated. Consequently, it is expected to yield among the largest slip amplitudes among the experiments conducted. This measurement indicates that only a relatively small amount of slip is necessary to achieve the damping performances observed. With the combined effects of the spool caps and winding start and end terminations, no significant large scale shifts in the wound roll layers were observed, despite sustained loading and regardless of the periodicity of the loading. These results suggest that the wound roll damping concept can operate effectively without requiring substantial stroke.

Comparing now the directions, slip measured on the transverse face is observed to be smaller than in the axial face. Additionally, in the transverse direction of measurement, there is no clear difference between the loose and tight winding cases: the curves coincide within the uncertainty of the measurement. In the axial direction of measurement, there is an unambiguous delineation between tight winding and loose winding, as seen in the difference of the slip magnitudes. Therefore, attention is focused on the axial measurements and the components of mandrel relative slip (s_x, s_y) can be examined separately.

In the axial direction, the vertical slip, s_y, is larger than the horizontal slip, s_x. This can be seen in Fig. 3.20, where the largest horizontal slip recorded does not exceed 0.005 mm. Thus, only the vertical slip data for the axial measurement direction is reported in Fig. 3.21 for both winding cases.

Fig. 3.21a and Fig. 3.21b show the vertical slip measurements, s_y, for each winding tension case, delineated by grouping as well as by layer. Here, the loosely wound case demonstrates larger slip magnitudes than the tightly wound case. Maximum slip, in either case, occurs towards the base of structure (Group 1) and falls off further away from the base, consistent with previous estimations. Comparing the magnitude of slip by layer, the maximum degree of slip does not occur at Layer 1, which does not match the theoretical prediction. However, a possible explanation for this discrepancy is that the leading edge of the 1$^{\text{st}}$ layer was fixed to the mandrel with tape at the beginning of winding, and so there is an additional constraint on this layer (Fig. 3.3).

Examining Fig. 3.21a, the mandrel relative slip magnitude curves for Layers 6, 11, and 16 coincide. This suggests that after a certain layer, between Layer 1 and Layer 6, there is no more relative movement between layers. This fact is clearly evident when considering the interlayer slip, $(s_x, s_y)_i^{j_1 - j_2}$, instead of the mandrel relative slip, as shown in Fig. 3.22. The curves in this figure are obtained by subtracting the centroid position of Layer 6 from the centroid positions of all subsequent layers in the time domain, and then taking the Fourier Transform.

Fig. 3.22 demonstrates that the measured slip relative to Layer 6 is indistinguishable from the static noise floor, which indicates that there is no appreciable interlayer slip beyond Layer 6. This result is consistent with the findings in Section 2.4, which indicated that the largest shear stress components for a wound roll undergoing base excitation were the σ_{rz} shear stresses in axis to the excitation direction. The location of these stresses was at the base of the structure, propagating only a small radial distance away from the innermost layer. This experiment confirms that due to the bending vibration mode of the structure, the inner layers towards the bottom of the roll, in axis of vibration, have the largest effect on dissipation for the wound roll damper concept due to slipping in the vertical direction.

3.6   Conclusion

In this chapter, the vibration performance of the wound roll damping concept was explored using a range of different excitation profiles. The results indicate that this
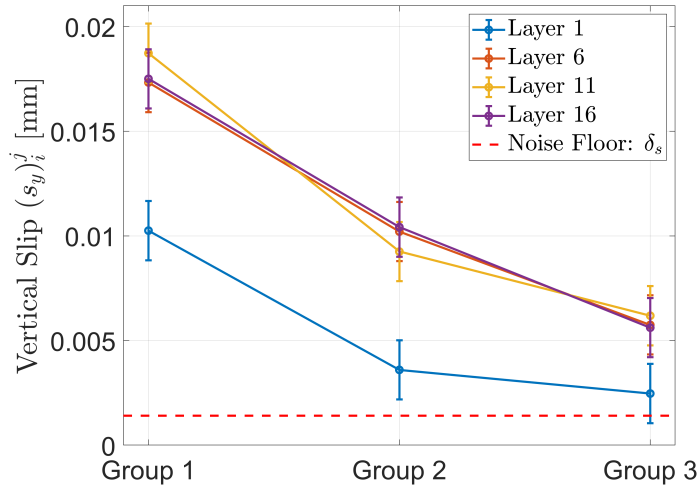
(a) Vertical slip by layer and group for loose winding.
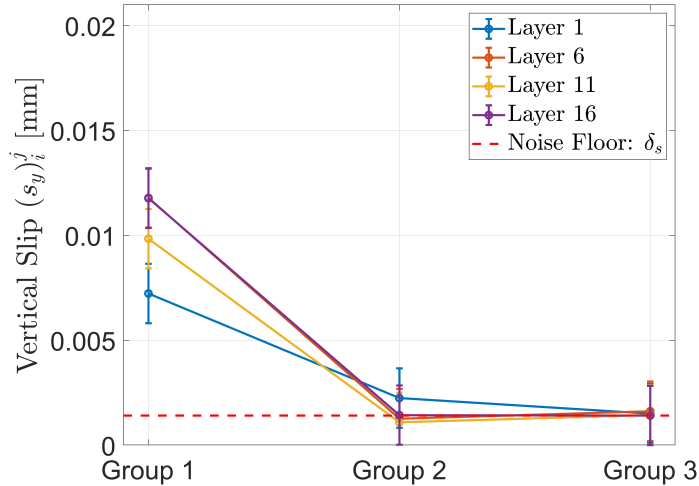
(b) Vertical slip by layer and group for tight winding.

Figure 3.21: Comparison between axially measured, vertical slip (s_y) relative to the mandrel for tight and loose winding.

concept is a relative motion device; regardless of the loading spectra or rate, if the excitation induces stresses that exceeds the shear capacity, slip occurs and leads to increased damping. This indicates that this concept works for any waveform or frequency, and works for all resonances.

The concept was demonstrated to exhibit sensitivity only to excitation amplitude, indicating discriminatory, self-scaling behavior. It "activates" only when stresses reach a sufficiently high level, and inherently scales with loading through the geometry of coiling. As loads increase, the propagation of slip through coiled layers and axial extents also increases, resulting in enhanced damping. Additionally, this scheme was proven to be an integral vibration damping and stiffness scheme that
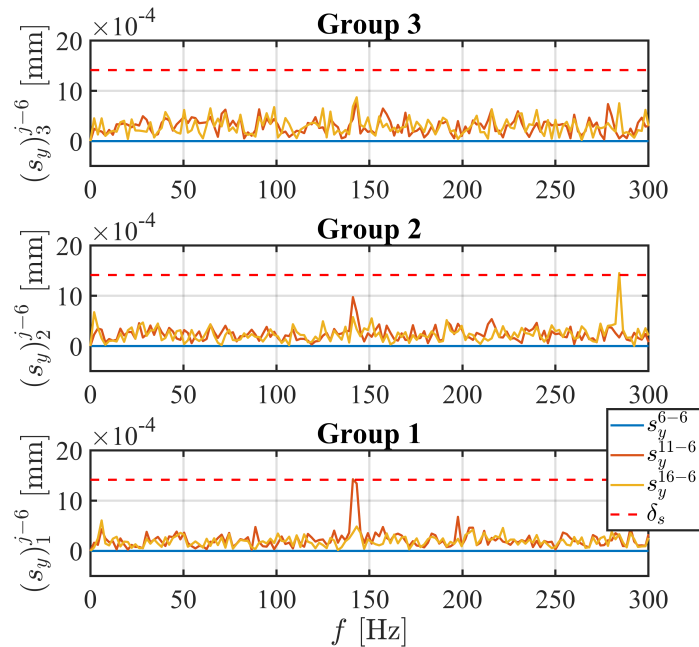
Figure 3.22: Interlayer slip, relative to layer 6, for axially measured, vertical slip (s_y) for loose winding. All interlayer slip measurements are below the static noise floor, indicating that there is no relative movement between layers after layer 6.

is tuneable with winding tension. Although, similar to other damping concepts, there remains an adverse relationship between damping and stiffness, the associated decrease in stiffness for increased damping is comparatively low.

The slip measurement experiment was able to confirm the 'active' regions in the wound roll damping concept. These are the regions where slip occurs during vibration and are responsible for the energy dissipation mechanism. High speed camera measurements determined that the vibration mode of the structure dictates the location of the actively slipping regions. For the case of a cantilevered, cylindrical structure with a wound roll damper, subject to base excitation, interlayer slip initiates at the base of the roll from the inner layers. This result indicates that, while the entire coiling form factor plays a role in the stiffness of the assembly, only a limited region may participate in the damping process for a given excitation loading level. This result is salient as it identifies the critical regions for focus when considering techniques to engineer contact properties to control slip for either the purpose of adjusting damping or protecting sensitive surfaces.

Chapter 4

FINITE ELEMENT SIMULATION OF WOUND ROLL DAMPING

4.1 Introduction

Following the experimental studies, a finite-element analysis (FEA) is performed in order to build a simulation model that correlates with the variations in damping and locations of slip observed in the experiments. The objective of this model is to capture the experimentally observed behaviors:

1. Quantitatively, the range and magnitude in damping and stiffness variations with preload.

2. Qualitatively, the positive skew transmissibilities for low preloads and the trends in responses with preload.

3. Inner layers towards the bottom of the roll, in the axis of vibration, contribute strongly to the energy dissipation due to slipping in the vertical direction.

The aim is to build the simplest model capable of encapsulating both the quantitative and qualitative features observed in experiments. Even qualitative agreement between experiments and simulation would provide a starting point for demonstrating understanding of the key parameters for this frictional damping mechanism.

Because the simulation now needs to provide damping estimates, the model consisting of a homogenized coil solid that is bonded to the mandrel can no longer be used, and discrete layers are required to model the contact interfaces for slip. Friction is a dynamic and time-dependent phenomenon where the frictional forces between surfaces can vary due to factors such as changes in relative motion and applied loading. This variability can lead to dynamic effects such as stick-slip behavior, hysteresis, and other temporally varying responses. As such, obtaining an accurate model of the vibration response and damping from Coulomb friction can only be achieved with time-domain simulations.

The simulation is conducted on a simplified, 3D representation of a wound roll, which consists of several concentric, cylindrical shells, which approximate coiled layers around a mandrel. The simulation uses geometry and properties derived from

the experimental setup. The coil layers are preloaded against the elastic mandrel using a range of pressures, and a friction interaction is defined between all adjacent contact surfaces. Base excitation is then applied, both in the form of sine sweep and sine dwell. The simulation is integrated in time, and the tip and base accelerations are recorded for the sweep excitation to obtain the frequency response, while the contact status of all elements is recorded for the dwell excitation to identify the extents of slip. The simulated frequency response, corresponding damping values, and slip locations are then compared against the experimentally measured values.

4.2 Wound Roll Damping FEA Simulation Setup and Simulation Procedure

The simulation is conducted on a simplified 3D representation of a wound roll that consists of several concentric, cylindrical shells, which approximates coiled layers around a mandrel. Similar to the experiment, the coiled structure is supported by an isotropic mandrel, fixed in a cantilevered configuration with a tip mass, m. The coiled structure is represented by n elastic layers placed around the mandrel, with the outermost layer preloaded with a pressure loading, σ_r. The mandrel is defined by the length, L, outer radius, r_m, and wall thickness, t_m. The coiled structure has the same length as the mandrel and layer thickness, t_l, which is scaled to have total thickness of all layers equivalent to the 25 Kapton layers in the experiment: $n \cdot t_l = 25 \cdot t_{Kapton}$ (Fig. 4.1).
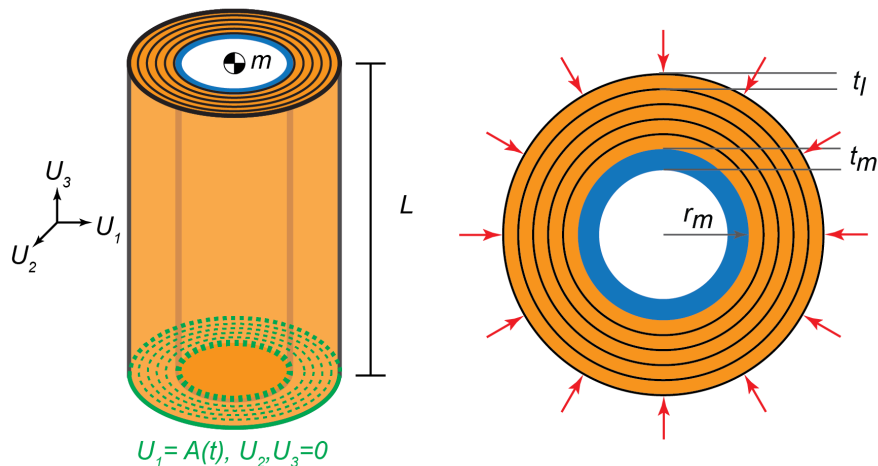
Figure 4.1: Geometry of coiled structure for FEA.

For this simulation, the geometry and properties used in the model are derived from the experimental setup in Section 3.2. The coil layers were preloaded against the elastic mandrel using a range of pressures, and a friction interaction was defined between all adjacent contact surfaces. The contact interfaces between the coil

and mandrel and adjacent coil layers are defined by a Coulomb-like, penalty friction model, where a small degree of elastic slip is allowed to help with convergence issues associated with the discontinuity of the unmodified Coulomb model (Fig. 4.2). The friction model is defined with coefficient of friction, μ, allowable elastic slip, γ^*, hard contact, i.e., no penetration, and separation allowed. No other form of damping was included. The numerical damping associated with the default integration method for dynamic implicit contact simulations is observed to have negligible effect on the simulation response. This is further discussed in Appendix B. The mandrel was modeled using S4R shell elements and the coil layers were modeled with M3D4R membrane elements, which have no bending stiffness. The base of the coil was assumed to be bonded to the mandrel's base (Fig. 4.1).
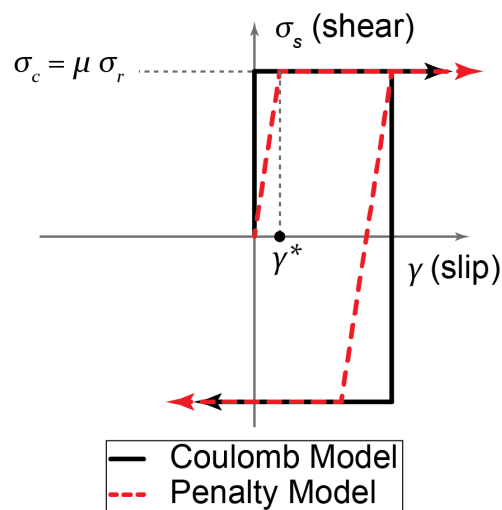
Figure 4.2: Penalty friction model compared against Coulomb friction model. Allowable elastic slip γ^*.

The geometry and properties of the mandrel-coiled layers system as well as certain simulation parameters are shown in Table 4.1 and in Table 4.2. These values were determined from a combination of datasheet properties, direct measurement, and correlation from indirect measurements. In particular, the modulus of the mandrel, E_m, was adjusted so that the resonant frequency of the 'mandrel-only' case matched experimental values of the corresponding 'mandrel-only' experiment. Similarly, the modulus of the Kapton layers, E_l, was tuned such that the resonant frequency of the simulation configuration with bonded coil layers (i.e., no slip), obtained from an eigenvalue frequency analysis, matched experimental values of the highest preload test case. In this manner, both the original underlying stiffness of the mandrel by itself and the limiting behavior of the highest preload experimental case were

captured. Densities were calculated assuming the basic dimensions of the geometry (i.e., theoretically exact) to calculate the volume, and weighing the physical test articles to obtain the masses. Appendix A discusses the sensitivity of the simulation model to the value of the allowable elastic slip, γ^*.

Table 4.1: Geometry and Simulation Parameters

L (mm)	D (mm)	t_m (mm)	t_l (mm)	n	μ	γ^* [m]
300	80	1.5	$25/n$	1–5	0.25	10^{-6}

Table 4.2: Material Properties

E_m (GPa)	ρ_m (kg/m^3)	E_l (GPa)	ρ_l (kg/m^3)	m (kg)
2.7	1200	2.8	2000	0.05

The finite element software ABAQUS was used to determine the variation in the vibration response of the coil-mandrel assembly, as well as the locations of slip. First, a static analysis was performed to apply the initial preload of the coil layer(s) against the mandrel. In the next dynamic implicit step, the assembly was subjected to one of two acceleration base excitations for each study and time integration of the model response was carried out.

For the frequency response study, sinusoidal base excitation using a geometric chirp base acceleration excitation was applied. The geometric chip, also referred to as an exponential chirp, is performed over a reduced frequency range from 125 to 175 Hz at a constant 5 m/s^2 amplitude with a 2 oct/min sweep rate. Despite finding no significant impact on modal response with varying sweep rates in experiments, a lower and more conventional sweep rate was chosen in simulations to err on the side of caution and ensure a conservative approach that does not affect modal response.

Fully modelling the dynamics and contact interactions between 25 layers for the experimental frequency sweep profile and duration was found to be computationally expensive. Therefore, using the results of Section 3.5, which indicated that the inner layers tend to exhibit more slip than outer layers, the simulation models only one layer $n = 1$ for the sweep studies. The range of preload stresses considered in simulation varies from 10 kPa to 300 kPa, which encompasses the range of experimentally applied radial stresses that are estimated using measured winding tensions with the stress models from Section 2.2 (Fig. 4.3).

Given the computational expense associated with time domain simulations, aggressive mesh reduction was conducted. Here, due to computation cost, mesh con-
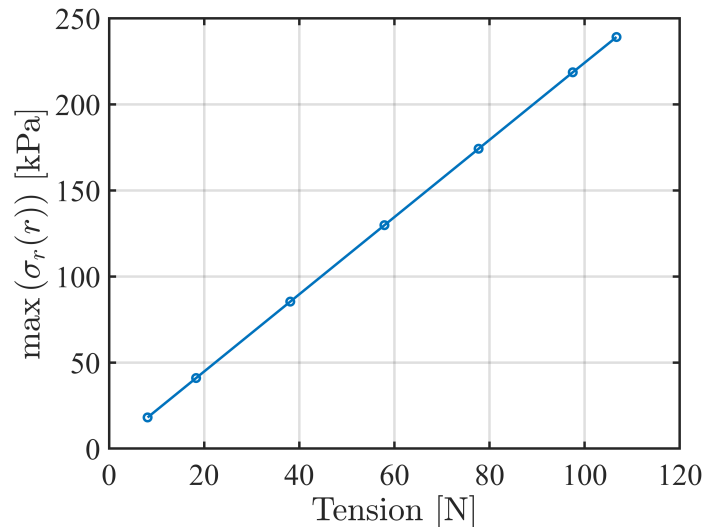
Figure 4.3: Estimated mapping of winding tension to radial preload, σ_r, calculated from winding stress models using experimentally measured winding tensions.

vergence was investigated using the linear perturbation frequency method instead of time domain simulations. The acceptable mesh density criteria corresponded to the lowest mesh density that still maintained 99% of the converged value of f_n. Generally, this corresponds to approximately 300 elements minimum for each shell, achieved by seeding the edges of the cylindrical shell with at least 30 mesh seed points on the circular edges and 10 mesh seed points on the axial edges.

The output of the sweep simulation provides the time history of the tip response of the coil-mandrel system, as well as the base input. The Fourier Transform of the tip response and base input, and subsequent ratio between the two provides the transmissibility response spectrum in the frequency domain, where the damping is estimated, again using the half-power bandwidth method.

For the layer slip study, a sine dwell base excitation was prescribed at the original 'mandrel-only' frequency, $f_n \approx 150$ Hz. Here, the number of modeled layers is increased, $n = 5$, in order to determine how many layers does slip propagate through during the vibration event. The simulation is run sufficiently long to reach steady state. In this simulation, each layer was individually preloaded with $\sigma_r = 200$ Pa. Thus, the total preload on the innermost layer, against the mandrel interface, was 1 kPa. The contact status of the elements for all layers as well as the mandrel was recorded for the dwell excitation, with acceleration amplitudes ranging from $1 - 3g$. The simulated frequency response, corresponding damping values, and slip locations from these two studies can be compared against the experimentally

measured values.

4.3   Results of Frequency Response Study

The simulated frequency responses for a variety of preloads are compared against a set of experimentally measured frequency responses with the closest equivalent measured preloads (Fig. 4.4). There is observed to be relatively good, agreement between the simplified FEA model and the experimental results.

Quantitatively, the simulation reports a span of resonant peaks and transmissibility amplitudes that are comparable to the experimentally measured results for a similar range of preloads. The response amplitude in both datasets decreases with decreasing preload, indicating that the looser winding exhibits increased energy dissipation and hence damping. For low preload cases, the experimental frequency response curves are positively skewed, which is likewise captured by the FEA model. This behavior is an indication of nonlinear damping or stiffness (softening) [69].

(a) FEA simulated frequency responses.   (b) Select experimental frequency responses.
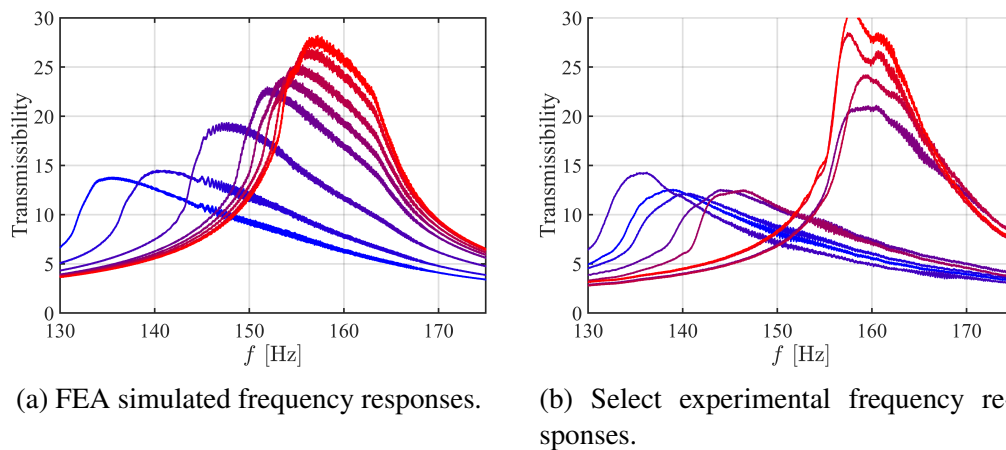
Figure 4.4: Comparison between simulated and experimentally measured frequency responses. Preload increases from blue to red.

The reduction in slip with higher preload results in decreased energy dissipation, causing the excitation response to increase compared to the lower winding tension cases. For both simulation and experiments, the reduction in slip further causes an increase in stiffness beyond the mandrel-only response, as seen with the highest preload responses where the resonant frequencies exceed that of the mandrel by itself ($f_n > 150$ Hz). This indicates that the FEA model successfully captures the stiffening effect where, for sufficiently high pretension, slip is suppressed, and the coiling form factor increases the effective wall thickness of the cylindrical sample, which causes the stiffer response observed.

Fig. 4.5 plots the damping values extracted from the simulated responses with the previously shown experimental data. Both datasets exhibit similar trends between estimated damping and apparent stiffness with preload variation. The estimated damping from simulation has relatively good agreement with the experimentally observed range, with comparable magnitudes and frequency range spans with preload. This suggests that the underlying physics, namely the frictional slip damping and structure-dynamic loading interaction, has been captured by the simplified model. Noteworthy is that these results were achieved by simulating a single contact surface, further indicating that the innermost layer is the most important to energy dissipation in this concept.
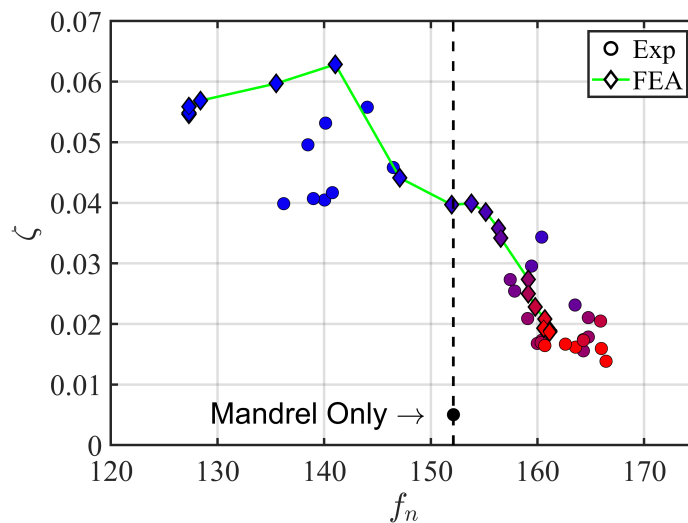
Figure 4.5: Damping-resonant frequency variation with preload; comparison between simulation (diamonds) and experiment (circles).

The frictional energy dissipation, E_F, can be directly extracted from the simulation results to determine if the response amplitude reduction of this concept is solely due to work done by friction or if additional contributions from other phenomena, such as destructive interference, need to be considered. The highest rates of frictional energy dissipation during the sweep coincide with resonance, where the wound roll is subjected to the greatest loads. This is shown in Fig. 4.6 where cumulative work done by friction is plotted on top of the mandrel tip response during the sweep.

Fig. 4.7 plots the maximum frictional energy dissipation against the applied radial preload. Here, the energy dissipation is observed to decrease with increasing preload. Comparing just the total energy dissipated by friction alone against the damping estimate, the peak damping configuration does not necessarily coincide with the highest energy dissipation (Fig. 4.8). Regardless, in general, higher damp-

(a) Low preload ($\sigma_r = 1$ kPa).

(b) High preload ($\sigma_r = 300$ kPa).
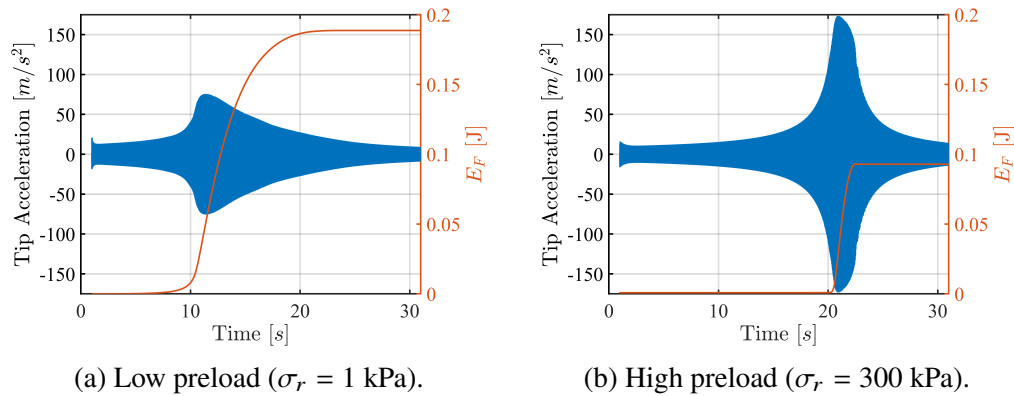
Figure 4.6: Tip response and frictional energy dissipation from FEA sine sweep for low and high preload cases. Energy dissipation rates are maximum around resonance.
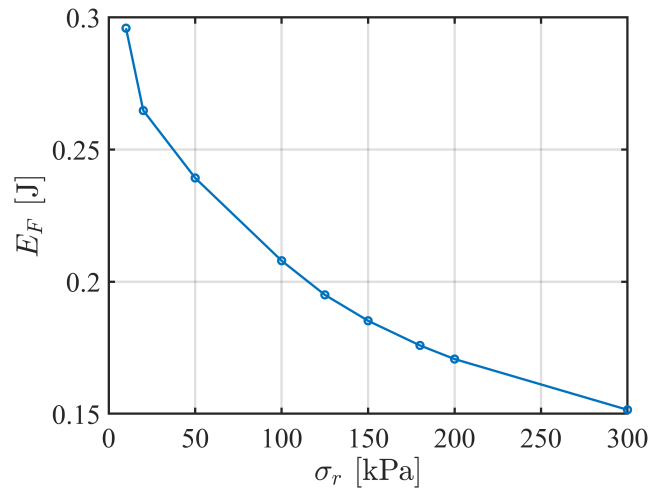
Figure 4.7: Frictional energy dissipation, E_F, from lab-scale FEA simulation vs. radial preload, σ_r. Energy dissipation decreases with radial preload.

ing is positively correlated with E_F. This result confirms that the response amplitude reduction in this damping concept is largely due to the friction dissipation mechanism.

4.4   Results of Interlayer Slip Dwell Study

After obtaining agreement between the simplified FEA model and frequency response experiments, this model is reused to determine the locations of slip. Here, the number of layers is increased from the previous study from $n = 1$ to $n = 5$ in order to find where slip occurs and its propagation through the layers. This was done by tracking the contact status of all surfaces, which differentiates between slipping and sticking contact states. Fig. 4.10 depicts the cumulative, steady state
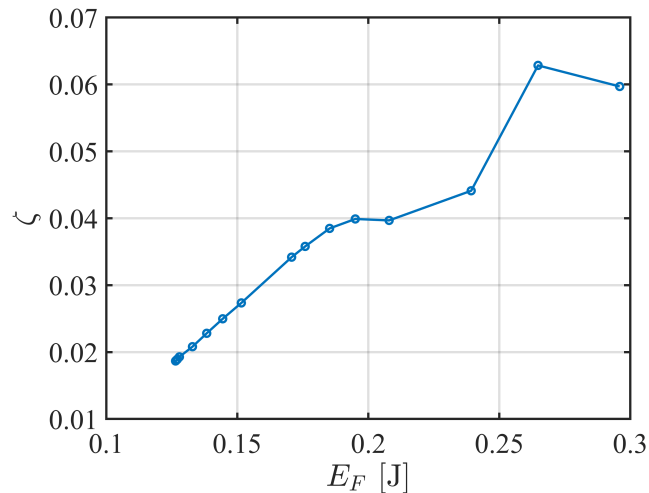
Figure 4.8: Frictional energy dissipation, E_F, vs. damping, ζ. Energy dissipation is strongly positively correlated with damping estimate for lab scale FEA simulation.

contact status for each layer across multiple loading amplitudes. Here, 'cumulative' meaning these plots depict locations of slip on each layer that was observed at any point during the simulation in red, whereas green denotes sticking, i.e., no slip, observed throughout the entire simulation. In this representation, the slip status of Layer j indicates slip with respect to Layer $j + 1$.

In Fig. 4.10a, the following behaviors are observed. First, the largest slip area occurs at the innermost interface, between the mandrel and Layer 1. Next, this largest patch of slip is vertical slip that occurs on the faces aligned with the U1 axis, which is the excitation axis. This can be seen in Fig. 4.11, which is a vector plot of the maximum, relative displacements between Layer j_{i+1} and the preceding Layer j_i, which is denoted as $\vec{U}^{j_{i+1}-j_i}$. And finally, after a certain layer, no slip is observed on any subsequent outer layers, as seen in both Fig. 4.10a and Fig. 4.11.

Keeping the friction and preload consistent, increasing the excitation level causes the area of cumulative slip to grow in the vertical direction as well as propagate through additional layers (Fig. 4.10b, Fig. 4.10c). This indicates that larger excitation increases the extent of the layers that actively participate in energy dissipation, corroborating the previously stated assertion that the performance of the wound roll damper inherently scales with the excitation level. All these behaviors are consistent with the findings of the slip estimation theory in Chapter 2.

Comparing the slip measurements obtained in simulation against experiment results in Sec. 3.5, there is likewise observed to be good, qualitative agreement for the behavior trends in slip propagation, except for the location of maximum slip. In

experiments, the location of maximum slip magnitude was not at the innermost layer of the roll. This is in contrast to both the simulated and theoretical prediction, where the maximum slip occurs at the innermost layer, between the 1st winding and the mandrel.

The reason for this discrepancy was previously theorized to be the result of the different boundary conditions. In the experiment, the longitudinal free edge of the innermost layer was fixed to the mandrel at the start of winding with tape (Fig. 4.9a). The extent of the constraint in the vertical direction, which is the dominant slip direction for this loading case, significantly limits the allowable movement of this layer. Conversely, both the theoretical and simulated models approximate the spiral wrap of the wound roll as a series of concentric shells, and each layer is restrained by the circular edge at the root (Fig. 4.9b). From the results depicted in Fig. 4.10, this boundary condition does not significantly restrict vertical slip, allowing the innermost layer to demonstrate the maximum slip magnitude.

Free edge terminated with tape
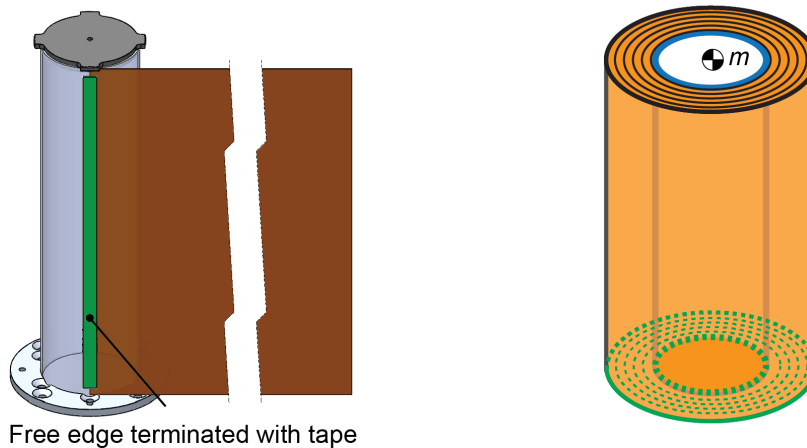
(a) Experiment boundary condition: vertical free edge of spiral wound membrane fixed with tape, arresting slip at the 1st winding.

(b) Simulated boundary condition: circular root edges of concentric shells fixed.

Figure 4.9: Different boundary conditions (highlighted in green) between experiment and simulation.

This discrepancy in layerwise location of maximum slip between simulation and experiments potentially indicates the sensitivity of this concept to the boundary conditions on each layer in the wound roll. However, in this particular configuration, the damping performance is not observed to be significantly affected, as there is good agreement between simulation and experiments in both transmissibilities and

damping magnitudes in Fig. 4.4 and Fig. 4.5 respectively. This further indicates that modeling a wound roll as a series of concentric cylinders is a good approximation, and additionally suggests that a damping device that consists of preloaded concentric cylindrical shells in frictional contact also constitutes a valid alternative damper configuration.

The results of this study demonstrate that the simulation successfully captures the experimentally observed behaviors: the inner layers towards the bottom of the roll, in the axis of vibration, have the largest effect on dissipation for the wound roll damper concept due to slipping in the vertical direction.
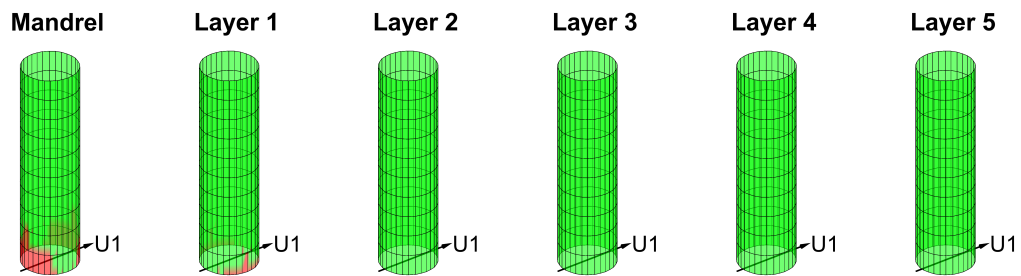
(a) Cumulative steady slip locations for 1g loading
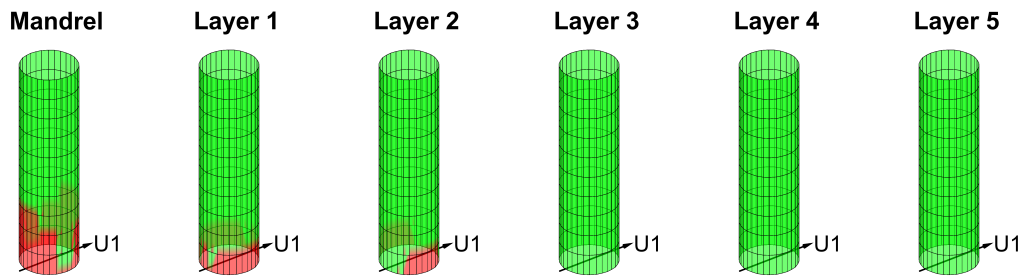
(b) Cumulative steady slip locations for 2g loading
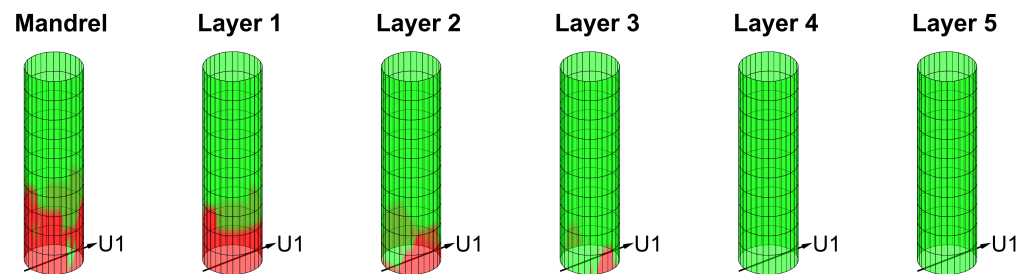
(c) Cumulative steady slip locations for 3g loading

Figure 4.10: Cumulative locations of slip with loading variation. Red indicates that slip has occurred at that location at some point during the simulation.

Layer 1	Layer 2	Layer 3	Layer 4	Layer 5
$\vec{U}^{1-r}$	$\vec{U}^{2-1}$	$\vec{U}^{3-2}$	$\vec{U}^{4-3}$	$\vec{U}^{5-4}$
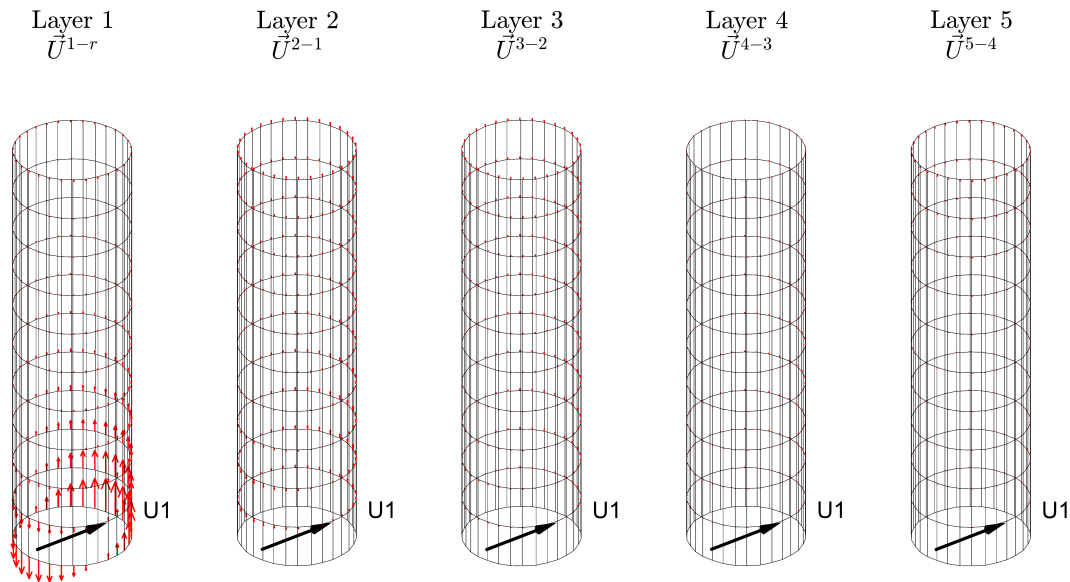
Figure 4.11: Maximum relative displacement vectors between adjacent layers for 1g loading. The largest vectors occur between Layer 1 and the mandrel in the vertical direction.

4.5 Conclusion

This chapter discusses a 3D FEA model for wound roll damping, composed of concentric shells representing the mandrel and coiled layers. This model is minimalistic and only includes the interaction between the material properties and geometry of the structure, the contact definition between interfaces, the preload, and excitation level. The simulated excitation included sine sweep to characterize the vibration response and sine dwell simulations, to observe the steady state slip response, mirroring experiments.

The relatively simple FEA model demonstrated good qualitative and quantitative agreement with experimental damping responses. The span of resonant peaks and corresponding damping variation with preload match those measured experimentally. The vibration response correlation between the FEA model and experimental results is noteworthy, particularly considering that only one slipping interface was modeled. This result reinforces the notion that the innermost layers are important regions of energy dissipation in this damping scheme.

Moreover, the slip investigation revealed slip extents and vectors consistent with experimental data and theoretical predictions. The results further confirm that slip propagates to additional layers and axial extents under larger excitation. This finding provides direct evidence of the self-scaling property inherent in this concept.

The identified underlying mechanism for wound roll damping is confirmed to result from the coupling between structural dynamics and interlayer contact properties. For a given loading, the locations of maximum shear stresses in the wound roll are seen at the base, near the mandrel interface. As a result, these are the locations where slip will initiate once the excitation level exceeds the force of friction.

Chapter 5

TWO DEGREE OF FREEDOM REDUCED ORDER NUMERICAL MODEL

5.1 Introduction

In the previous chapter, a non-linear, finite element model was demonstrated to have good prediction of the vibration response of the wound roll damper. However, these efforts are computationally expensive. For the FEA model studied, several approaches were employed to reduce computation time, which included aggressive mesh density reduction, modeling slip along a single interface to decrease the number of contact surfaces, biasing the resonance of the wound roll system towards lower values to reduce required time increments, and utilizing a relatively fast sweep rate to lower the total simulation step time. Despite these efforts, a single simulation run still demands a CPU computation time spanning 50 to 100 hours. Consequently, it takes approximately 3 to 5 days to complete a set of 10 simulations on a server-class machine (2x Intel(R) Xeon(R) Gold 6354 CPU and 1 TB ram). The duration required for implementing this approach makes it impractical for conducting studies to explore design space associated with this damping concept. As such, a more efficient method is needed.

It is commonly asserted that mechanical systems can be represented by a simple 1D mass-spring-damper systems. Thus, this is the approach that is taken here. In theory, the wound roll damper concept could be modeled with a single mass along with nonlinear stiffness and damping functions that are fitted to the observed dataset. For dissipative systems, there are also methods that similarly abstract away the complexities of the physical system and are capable of estimating damping by modeling only the hysteretic stress-strain behavior [70–73]. These methods simplify the analysis by focusing on the net effective force-displacement behavior, rather than the detailed interactions between the structure, loading, and dissipation mechanisms. However, the objective is to refrain from transforming this problem into a black box and instead maintain a physics-based approach that preserves understanding and interpretability as much as possible. Thus, a key self-imposed constraint for this study involves requiring the modeling of a friction interaction.

The vibration of 1D friction systems is extensively studied with a variety of problem-

solving techniques [74–79]. Many of these studies make assumptions of the solution such as focusing on or linearizing about the state of continuous or steady sliding motion, which permit closed form analytical solutions, frequency domain methods, or other model reduction and simplification techniques. However, in this work, there is no assumption on the degree or state of sliding. In the presence of realistic excitation, it is anticipated that this damper concept will exhibit a spectrum of behaviors, spanning from no slip to stick-slip to continuous slipping [80]. As such, the technique taken here is solving the equations of motions using numerical integration in the time domain.

The objective of this 1D friction-vibration model is to achieve the same frequency response behaviors under base excitation as seen in experiments and simulations. Specifically, the targeted behaviors to capture in the vibration response are the variations in damping and stiffness with preload. From experiments and simulation model, and the requirement to explicitly model a friction interaction, it's clear that at least two masses are required to accurately depict this system: one representing the mandrel, referred to as the primary, and the other representing the coil, referred to as the secondary.

With the stipulation that the masses be in contact to model a frictional interface, there are only three possible arrangements of the two masses that are differentiated by the base boundary condition of the secondary: base fixed with the primary and driven directly by the base excitation, isolated from excitation and driven only by the motion of the primary, and attached directly to the primary (Fig. 5.1).

(a) Based fixed secondary   (b) Base isolated secondary   (c) Fixed to primary
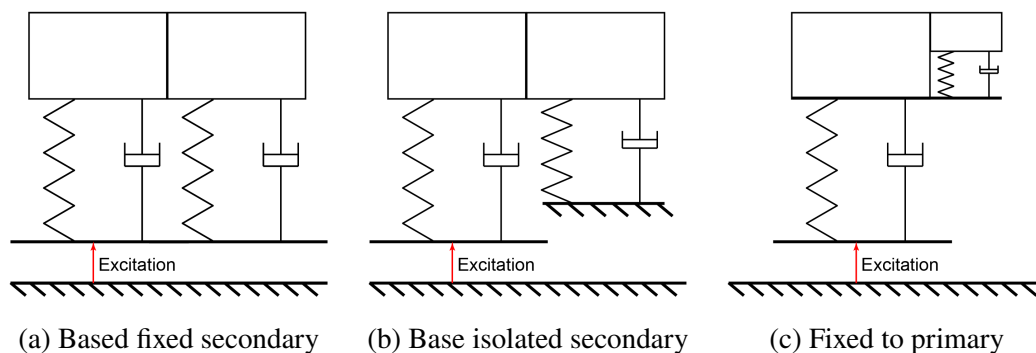
Figure 5.1: Possible 2-DoF friction mass-spring-damper models.

The model selection among these options was conducted through a qualitative evaluation of each model's capability to effectively capture the desired responses using inspection and initial exploratory simulation studies. Attaching the secondary

to the primary can be immediately ruled out, because the overall stiffness of this assembly does not increase with preload; the secondary always serves as an added mass (Fig. 5.1c). The other two models are observed to be capable of capturing the stiffness increase with preload. In the limit of sufficiently high preload, the primary and secondary masses stick together, where the overall system stiffness is then a combination of the two stiffness.

Among these two options, the base isolated configuration was compelling because it suggests that the primary response drives the excitation of the secondary (Fig. 5.1b). This initially seemed more representative of reality, given that the roll is attached only to the mandrel in experiments. However, the base-isolated model was ultimately rejected due to its excessive coupling of the secondary response to the primary. In scenarios where the primary might exhibit a diminished response due to its own dynamics, the reduced excitation applied to the secondary could erroneously imply the absence of secondary motion, even though the secondary may possess its own vibration mode. Furthermore, during initial exploratory tests, this model failed to adequately exhibit the desired qualitative behaviors in its responses. Experimentally, the transmissibilities are observed to demonstrate a positive skew (Fig. 5.2a), where this model generally produces responses with a negative skew (Fig. 5.2b). As such, the based-fixed secondary, where the secondary is directly excited by the base vibration, was selected (Fig. 5.1a).
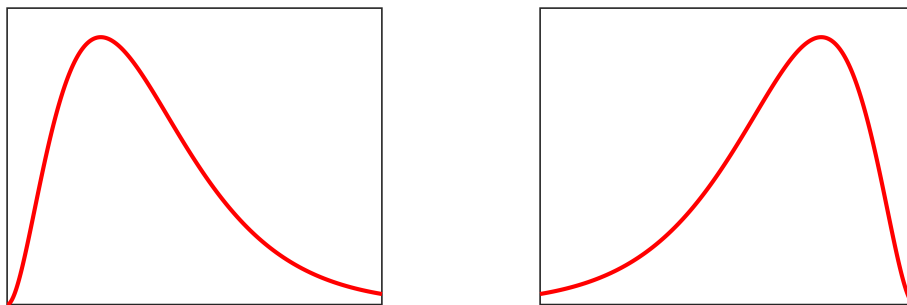
(a) Positive skew: typical of experimentally observed wound roll transmissibilities for low preloads.

(b) Negative skew: not observed experimentally.

Figure 5.2: Positive vs. negative skew response curve shapes.

The remainder of this chapter describes the model in more detail and discusses the key properties necessary for this model to capture the wound roll vibration response behaviors. The model is compared with experimental and simulated values through frequency response transmissibility curves to verify that the model

accurately captures the desired physics of the wound roll damper.

5.2   2-DoF Model Definition and Numerical Simulation Procedure

Fig. 5.3 illustrates the diagram of the two degree of freedom, reduced order model of the wound roll damper. The model consists of two separate mass-spring-damper systems, (m_i, k_i, c_i) for each mass $i \in [1, 2]$, that are preloaded together in contact with a force, F_N. The primary mass represents the mandrel and the secondary mass represents the wound roll. The masses do not have dimension, and are therefore assumed to always remain in contact. Both masses are attached to the same reference plane, which is subjected to a sinusoidal displacement load with amplitude Y_0 and frequency ω.
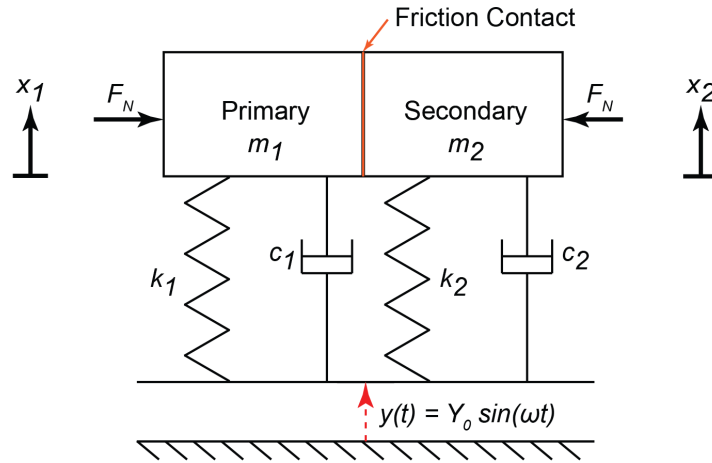
Figure 5.3: 2-DoF mass-spring-damper model of wound roll damper with frictional contact subject to harmonic load.

The free body diagram of the masses are shown in Fig. 5.4. The friction model employed in this study continues to be the Coulomb Friction model with a coefficient of friction, μ. Here, the direction of the friction force is captured through the "sign" function applied on the difference in velocity of the two masses:

$$\mathrm{sgn}(\Delta \dot{x}) = \begin{cases} -1 & \text{if } \Delta \dot{x} < 0 \\ 0 & \text{if } \Delta \dot{x} = 0 \\ 1 & \text{if } \Delta \dot{x} > 0 \end{cases} \tag{5.1}$$

This enforces the direction of friction force to always act opposite the direction of each block's velocity.
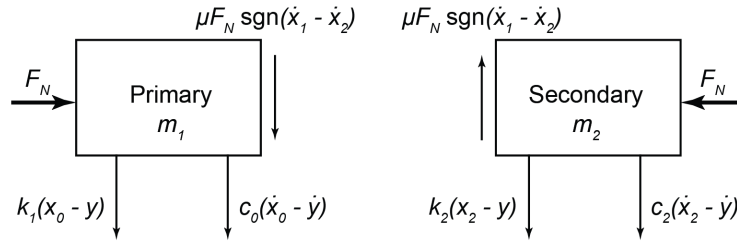
Figure 5.4: Free Body diagram of primary and secondary masses.

From this, the coupled equations of motion of the system are:

$$m_1\ddot{x}_1 + k_1 x_1 + c_1 \dot{x}_1 + \mu F_N \text{sgn}(\dot{x}_1 - \dot{x}_2) = k_1 y + c_1 \dot{y} \tag{5.2}$$

$$m_2\ddot{x}_2 + k_2 x_2 + c_2 \dot{x}_2 - \mu F_N \text{sgn}(\dot{x}_1 - \dot{x}_2) = k_2 y + c_2 \dot{y} \tag{5.3}$$

These equations can be converted into continuous-time state-space form in order to be solved in MATLAB. However, the raw form of the governing equations presents a challenge in numerical integration due to the sign function's discontinuity at $x = 0$. This discontinuity renders the problem excessively 'stiff', leading to numerical instabilities that manifest as issues such as oscillations, inaccuracies, and difficulties in achieving convergence [81]. Using the sign function in the equations of motions is observed to significantly extend the simulation runtime and result in spurious spikes in the frequency response curves.

Similar to how the penalty model uses a small degree of elastic slip to help with convergence in FEA, here the Coulomb Friction model is approximated with a smooth function to remove the discontinuity to speed up computation time [82, 83]. There is a spectrum of possible smooth approximations; here, the selected approximation involves the use of a logistic function, $s(x) = \frac{1}{1+e^{-x}}$. The function is adjusted to shift its output range from -1 to 1:

$$\text{sgn}(x) \approx S(x) = 2s(x) - 1 = \frac{2}{1 + e^{-x}} - 1 \tag{5.4}$$

Appendix C discusses the sensitivity of the simulation results to the accuracy of the sigmoid approximation.

Utilizing the smooth approximation, the governing equations are converted into a system of first order differential equations, and then solved using the *ode45* function with zero initial conditions. To derive the response spectrum, a series of dwells were conducted across a range of excitation frequencies, ω. Each simulation was
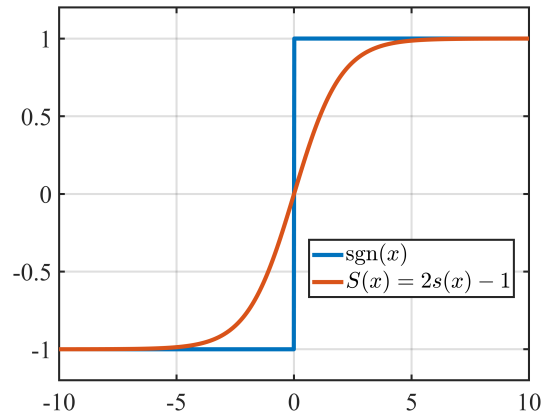
Figure 5.5: Smooth approximation to the sgn function.

integrated for a duration of 6 time constants: $T = 6\tau$, where τ corresponds to the time constant for a second order, underdamped system responding to a step response and is a function of the natural frequency of the system, ω_n, and the damping ratio, ζ, given by [84]:

$$\tau = \frac{1}{\omega_n \zeta} \tag{5.5}$$

Due to the lack of prior knowledge about the natural frequency of the system for a given preload, the current forcing frequency ω is used to estimate the time constant for each run. Additionally, a highly conservative damping ratio of $\zeta = 0.2\%$ is assumed for this calculation to better ensure that the duration of the simulations are sufficiently long for the transient response to decay and the steady state response to be reached.

The call to the *ode45* command to solve the differential equation is encapsulated within a wrapper function to facilitate parallel computing against multiple excitation frequencies simultaneously using *par-for-loops* from the Parallel Computing Toolbox in MATLAB [85]. The output for each excitation frequency simulation run is the peak steady state displacement of the primary mass.

The response of this model results from a coupled interaction between the loading, amplitude Y_0 and frequency ω, preload F_N, and structure properties, (m_i, k_i, c_i). In this model, the specific values of μ and F_N independently hold no significance; μ only plays a role in the force balance equation through the product of the two terms, which is a measure of the friction force capacity: $F_c = \mu F_N$. Consequently, to span different winding tensions, iteration is only necessary for a single loop involving the force capacity, F_c.

In general, the structure properties (m_i, k_i, c_i) are constants, except for the masses, (m_1, m_2), and the secondary mass stiffness, k_2. Initially, the model was run with all structure properties held constant to assess whether friction contact alone was sufficient to cause all desired behaviors; however, the observed responses did not capture the desired behaviors, specifically the positive skew response shape. These results lead to the hypothesis that incorporating nonlinear stiffness is also necessary to accurately model the wound roll damper [69].

Upon reviewing the experimental data, theoretical foundations established in previous chapters, and the results of the numerical simulations with constant structural parameters, it became evident that there were two related issues with the model. First, using a constant secondary stiffness did not accurately account for the fact that the stiffness of the secondary varies with preload, $k_2 = f(F_N)$. Second, due to the variation in stiffness with preload, for sufficiently low preload the wound roll becomes too loose to support itself, and instead relies on the mandrel for support. In this regime, the wound roll behaves as an added mass on the mandrel. For higher winding tensions, the wound roll gains increased stiffness, transforming into a more cohesive structural element that is capable of supporting a greater portion of its own weight.

These related behaviors can be effectively modeled as a nonlinear variation in secondary stiffness and a zero-sum, 'added mass loading' from the secondary to the primary that changes with preload. The entire spectrum of potential nonlinear functions that can describe this phenomenon is vast, but the fundamental characteristic required is that the stiffness should increase with preload and approach a limiting behavior for sufficiently high preload. The behavior of the mass is likewise expected to follow this trend, where for low preload the mass of the secondary is added to the primary mass and wholly supported by the primary stiffness. The added mass loading reduces as the preload increases until reaching a point where the mass is entirely reconstituted in the secondary and supported by its own stiffness.

This phenomenon is accurately described by the sigmoid function already being used to smooth out the discontinuity of the friction definition, which prompted its adoption as an initial hypothesis. Here the new, nonlinear secondary stiffness, k_2', where the preload dependence F_N is replaced by the friction capacity F_c to keep the single loop variable, and is given by:

$$k_2' = k_2 \cdot S(F_c) \tag{5.6}$$

And the statement of zero-sum 'added mass loading' from the secondary and the primary mass is given by:

$$m_1' = m_1 + m_2 \cdot [1 - S(F_c)]$$
$$m_2' = m_2 \cdot S(F_c)$$

<div align="right">(5.7)</div>

Initial simulations suggested that these two factors were the crucial elements missing, as after incorporating the effects of nonlinear stiffness and mass, the simulations accurately captured all desired qualitative behaviors. The potential of this model in simulating the vibration response of the wound roll damper is demonstrated via correlation against the experiment and simulated results.

5.3 Comparison with Experiments and FEA

To confirm the effectiveness of the reduced order, 2-DoF model of the wound roll damper, the goal is to use the model and compare its results with experimental data and FEA simulation results. Correlation is achieved when the transmissibilities span the same frequency range and amplifications with preload variation as well as demonstrate the same qualitative behaviors, such as the positive skew response for low preload. To run this model, 8 parameters are needed: a set of three of mass-spring-damper values (m_i, k_i, c_i) for each mass, the friction capacity F_c, and the amplitude of excitation, Y_0.

Without loss of generality, the frequency response can be initially normalized so the resonant frequency corresponds to $\omega_n = 1$, where the masses are normalized by the primary mass, m_1, and the stiffness are normalized by the primary stiffness, k_1. While the model illustrated in Fig. 5.3 includes discrete dampers for each mass, this is primarily for the sake of generality and to ensure a bounded response under conditions of extremely low or high preload. The intention is for the contact friction to provide the primary damping effect in this simulation. As such, the damping values, (c_1, c_2), are intentionally set to very low values for the main purpose of ensuring finite responses. This is necessary in the limits where the preload is either low enough to decouple the responses of the primary and secondary, or when the preload is high enough for the masses to stick. In either case, the friction contact produces little damping.

Initially, at this juncture, a grid search was employed to iterate over the remaining unknown structure parameters, the limiting secondary properties: (m_2, k_2) along with the intended parameter variations, (ω, F_c, Y_0). The implementation of this

brute-force method served the dual purpose of gauging sensitivity to individual parameters and identifying the configuration that yielded the best performance. Following an initial coarse search, a set of parameters demonstrating the best performance was chosen for further refinement. A notable advantage of maintaining a physics-based approach in the modeling of this system was observed in the ability to justify the best-performing values by relating them with the experimental properties and measurements.

While both the mass and stiffness of the secondary affect the overall amplitude and span of the frequency responses with preload variation, the mass m_2 was observed to have more control over the resonance location for lower preload, representing the resonant frequency floor for a set of winding tension variation responses. The secondary stiffness, k_2, largely controlled the amplitude of response as well as the resonance location for high preload, representing the resonant frequency ceiling for a set of winding tension variation responses. The best-performing value of m_2 closely aligned with the actual mass of the wound roll in experiments, normalized by the mass of the mandrel (experiments: $\frac{m_s}{m_m} = \frac{0.12 \text{ kg}}{0.15 \text{ kg}} \approx 0.85$). After this value was set, the value of k_2 was selected from a refinement that targeted aligning the resonant peaks of the numerical simulation in the bonded-masses limit with the experimentally observed range. With the mass-spring-damper values finalized, the range of frequency responses for preload variation was largely fixed. Finally, the amplitudes of the transmissibility were tuned by varying the excitation amplitude, Y_0. While the exact values of preload and the excitation amplitude individually do not have direct experimental justification, the ratio between them does.

In previous studies of the dynamics of 1-DoF mass-spring systems with friction under base excitation, the vibration response was observed to only depend on the frequency of forcing and the force ratio between friction and the max spring force, $\frac{F_c}{F_k}$ [74, 76]. In a one-dimensional system where the force of friction acts in opposition to the motion of a base-excited mass, the extent of motion is determined by the relative magnitudes of the friction force and the spring force. Based on these findings, a similar technique is employed here to provide justification of the relative magnitudes of Y_0 and F_c used in the simulations by comparing the estimated values from experiments.

To estimate the force ratio from experiments and simulation, an estimate of the friction force and the maximum 'spring' force are needed. In experiments, the friction force is assumed to be equal to the maximum friction force the entire

cylindrical interface between the mandrel and 1$^{\text{st}}$ winding can support. In simulation, the maximum friction force is simply the shear capacity, F_c. For this work, the spring for both experiments and simulations is assumed to correspond to the mandrel, which is the primary mass in simulation. In experiments, the spring stiffness is the flexural stiffness of the mandrel and the force is calculated from the deflection of the tip mandrel. For simulation, the spring force is calculated from the primary stiffness, k_1, and the input forcing displacement, Y_0.

Table 5.1 shows the assumed values to estimate the experimental force ratio between friction and mandrel deflection. The maximum shear capacity estimated in the experiments is $\sigma_c = \mu \sigma_r = 75$ kPa. Over the surface area of the innermost layer, the total friction capacity is approximately $F_c = 2\pi r h \sigma_c = 6$ kN. Assuming the vibration loading of the wound roll can be approximated as a tip load, the flexural stiffness of the mandrel with modulus, E, second moment of area, I, and length L, given by:

$$k = \frac{3EI}{L^3} \tag{5.8}$$

With the assumed tip deflection of $x_{tip} = 1$ mm, the spring force of the deflected mandrel is $F_k = kx_{tip} \approx 100$ N. Under these assumptions, the experimental force ratio is given as $\frac{F_c}{F_k} \approx 60$.

Table 5.1: Assumed properties to calculate the ratio between friction forces and mandrel 'spring' forces in experiments.

μ	σ [kPa]	r [mm]	h [mm]	x_{tip} [mm]	E [GPa]	t_m [mm]
0.25	300	40	300	1	2.8	1.6

Originally, this work assumed $Y_0 = 1$ and $F_c = 1 - 100$, which satisfied the required force ratios ($\frac{F_c}{F_k} = \frac{F_c}{k_1 Y_0} = 100$). However, the positive skew response and transmissibility amplitudes were not obtained. Increasing Y_0 was necessary to both achieve the desired response skew shape and the desired response magnitudes. Despite this adjustment to Y_0, the range of force ratios remained within the desired range to match experiments ($\frac{F_c}{F_k} = \frac{F_c}{k_1 Y_0} \approx 70$). Table 5.2 lists the best performing values identified that were selected for output comparison. Note that no claim is made about the global optimality or uniqueness of this solution.

Table 5.2: Best performing numerical simulation properties

m_1	k_1	c_1	m_2	k_2	c_2	Y_0	ω	F_c
1	1	0.002	0.85	1.15	0.0025	1.5	0.4–2	1–100

Fig. 5.6 compares a subset of the frequency response curves for the wound roll damper obtained from experiments, FEA simulations, and the numerical reduced order model discussed in this section. For the numerical result, the horizontal axis scaled so that $\omega_n = f_{n,mandrel}$. While the correlation is not exact, this reduced order model is demonstrated to have acceptably accurate performance. Over the same frequency range and span of preload ratios, the model remains within the experimentally observed transmissibility range and demonstrates the same qualitative response variation with preload.

As observed with experiments, the reduce order model begins with a positively skewed response at low preload and generally demonstrates the largest damping values. Based on the insights acquired during the development of this model, it is now understood that the positive skew response is a consequence of the nonlinear stiffness of the wound roll with preload and the associated additional inertial loading that is applied to the mandrel when the roll is too compliant to support it own weight. As the preload increases, the response becomes more symmetric and increases with amplitude and resonant frequency, indicating increasing system stiffness; consistent with both experimentally measured and simulated responses. As a result of this study, a relatively simple model of the wound roll damper has been obtained, which not only offers profound insights into the physics of the wound roll damper, but is also considerably faster than FEA simulations, enabling the examination of a broader design space.

5.4   Discussion on Issues with Generalizability via Design Space Studies

Having established correlation and gained confidence in its accuracy at a single design point, an attempt was made to utilize the reduced order model framework to explore an extended design space using this more efficient technique. Here, the objective was to examine the sensitivity of the wound roll damping concept to the relative masses and stiffnesses of the mandrel and the wound roll. The non-dimensionalized space is maintained, keeping masses and stiffnesses normalized to the primary properties. With this approach, the absolute mass and stiffness are abstracted out, which was intended to allow the results to be more broadly applicable to arbitrary configurations that share the same relative mass and stiffness ratios. Table 5.3 shows the span of parameters considered.

Fig. 5.7 illustrates the contour map of maximum possible damping from the design space considered, which varies m_2 and k_2. This study suggests that for a fixed sec-
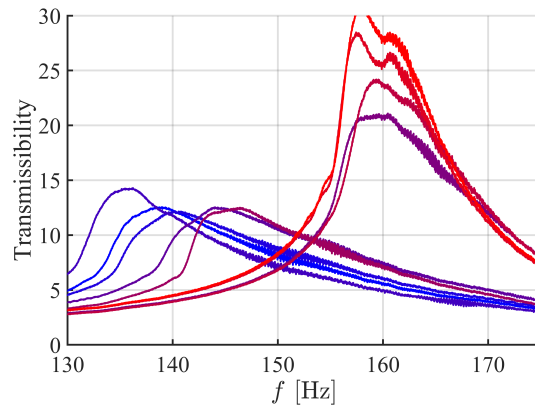
(a) Experimentally measured response.
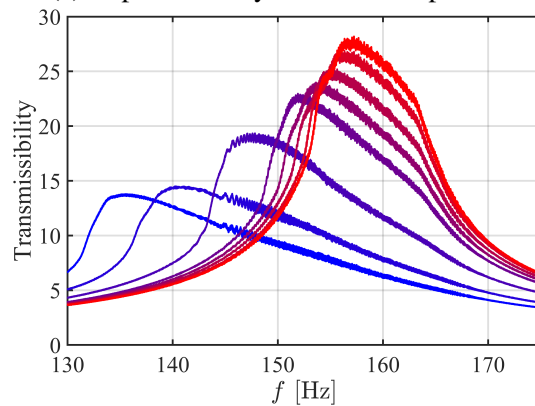
(b) FEA simulated response.
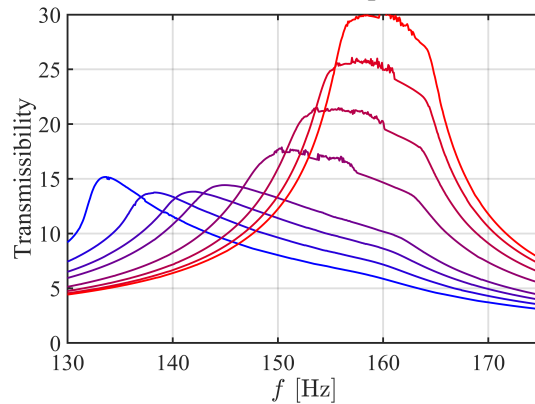
(c) Reduce order model numerical simulated response.

Figure 5.6: Wound roll damper vibration response variation with winding tension/preload obtained from experiments and simulations. Curves are depicted with a gradient ranging from blue to red, transitioning from lower preload to higher preload.

ondary mass, increasing the secondary stiffness should result in increased maximum damping.

Table 5.3: Design space survey simulation properties

m_1	k_1	c_1	m_2	k_2	c_2	Y_0	ω	F_c
1	1	0.002	0.25–2	0.5–2	0.0025	1	0.4–2	1–100
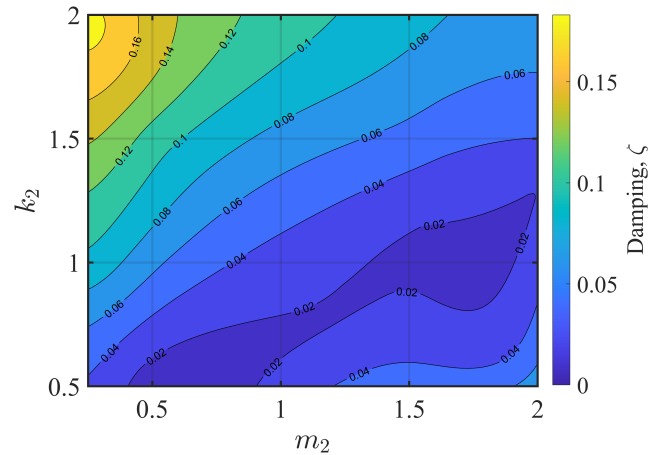
Figure 5.7: Design space contour map of maximum damping obtained using 2Dof reduced order model.

To validate this result, the FE model from the previous chapter was re-run for different values of the layer modulus E_l, maintaining all other parameters constant. Fig. 5.8 plots the variation in the damping response for several increasing values of E_l. Contrary to the damping contour map obtained from the reduced order model, the maximum possible damping obtained from the FE model decreases as the roll stiffness increases.
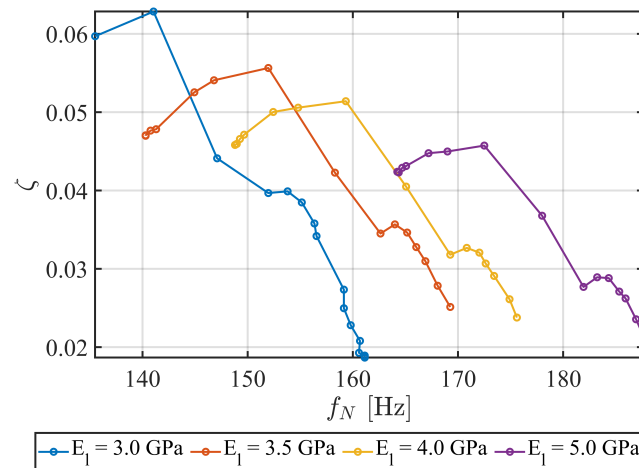
Figure 5.8: Variation in lab-scale simulated damping response with changes to wound roll layer modulus. Peak damping recorded decreases with increasing roll modulus.

While good correlation was achieved for the fitted response, definitive generalization of this model beyond single-point fitting is not possible at this time. Future work will be required to investigate this discrepancy.

5.5 Conclusion

In this chapter, a reduced order, 2-DoF model of the wound roll damper was proposed. This model was a physics based approach that explicitly modeled a friction contact between two mass-spring-damper systems. The primary system represents the mandrel, and the secondary system represents the wound roll. The key factors contributing to the success of this model in capturing the physics of the wound roll damper was modeling the nonlinear stiffness variation and added mass loading of the secondary. The model was demonstrated to have good correlation with experiments and simulations using values that are justifiable from experiments.

The impact of this model is significant for several reasons. First, it is dramatically faster than FEA, allowing rapid traversal of a wider design space to perform design studies to identify best performing configurations. Second, using the model with normalized values abstracts away dependence on the absolute values of properties, thereby enhancing its versatility and applicability to any arbitrary systems with similar relative properties. Finally, as the model is grounded in physics during development, additional understanding of this concept has been gained from the sensitivity studies performed in the incremental process of developing this model. Thus, the model and results are interpretable, which increases comprehension of the wound roll damping concept behavior and sensitivities.

Chapter 6

VIABILITY OF THE WOUND ROLL DAMPING CONCEPT AT REALISTIC SCALES.

6.1 Introduction

The potential of the wound roll damper concept has been validated through a combination of vibration experiments, finite element analysis (FEA), and numerical simulations. The discoveries made up to this juncture demonstrate the following properties of this damping concept:

1. This scheme utilizes the properties intrinsic to the coiling packaging scheme, i.e., coiling packages a structure in a cylindrical shape, which has potential geometrical benefits, and creates distinct layer interfaces to facilitate slip dissipation, and thus requires no added components and is entirely passive.

2. The damping and overall stiffness of the system can be varied depending on the winding tension applied. While damping and stiffness are inversely related, the associated cost of increasing one parameter for another was observed to be relatively small.

3. Slip initiates from a relatively small region within the roll, and the extent of the slipping regions is affected by the relative magnitude between the interlayer friction capacity and the excitation magnitude. Only a small amount of motion is sufficient to provide significant damping.

4. Through the layered geometry, the damping concept exhibits a discriminatory, self-scaling behavior. For low excitation, no slip occurs and there is a stiffer overall response. Increasing excitation levels causes slip to propagate to additional layers in the coil, which increases damping.

5. The damping concept is a relative motion device and therefore works for any excitation profile.

These findings were obtained from experiments and simulations at laboratory scales. Real-world deployable space structures that are packaged by coiling, such as ROSA, Starshade, and the Caltech Space Solar Power Project (SSPP), encompass a broad

spectrum of stiffnesses, length scales, and number of wound layers [30–33]. In order for the wound roll damping scheme to be utilized in practice, its capabilities must be understood in broader and more practically applicable contexts.

Hence, the objective of this chapter is to assess the performance of the wound roll damper concept under more realistic scenarios by investigating its sensitivity to changes in physical parameters of the coil, such as the mass, effective stiffness, and the number of coiled layers, as well as to understand how the damper concept performs at scale. The finite-element (FE) simulation, already employed previously, is reused to study a geometrical and material design space that is informed from real-world coiled space structures. The simulation model is a simplified 3D representation of a wound roll, comprising a cylindrical solid, that approximates a set of coiled layers, concentric with a mandrel shell held in a base-fixed configuration. In this configuration, slip occurs solely along the coil-mandrel interface, with no slip assumed within the coil itself. To emulate the stress state imposed by a winding tension, the coiled layer solid is preloaded with a surface pressure, and a friction interaction is defined between the outer surface of the mandrel and the inner surface of the coiled layer solid.

The primary performance metric outputs from these simulations are the damping ratio, ζ, and the resonant frequency of the system where the damping ratio is measured, f_n. To obtain these two metrics, a sine-sweep base excitation is applied. The simulated structural response is integrated in time, and the tip and base accelerations are recorded for the sweep excitation. The simulated frequency response and corresponding damping ratio values can then be extracted for any given configuration selected from the design space. The results of the finite-element simulation are used to determine the performance and sensitivity of the wound roll damping concept in a realistic design space, using the resonant frequency and damping ratio for each configuration studied. Attention is given to the range and rate of variations to provide indications of performance, robustness, and tunability of the wound roll damper concept.

6.2   Parameter Space and Geometry Definition

This section describes the methodology for selecting the design space in terms of material properties and geometric parameters that will be used in the FE simulation to study the damping and stiffness for realistic applications. These parameters are important for the performance of the wound roll damping concept, as the material

properties and geometry of the structure couple with the environmental loading and contact properties to determine the structural response. Consequently, they play a pivotal role in influencing the damping and resonant frequency performance metrics that are extracted from the system response. Here, real-world coiled space structures, are examined.

The geometries of the coiled structure in this simulation study are derived from recent, state-of-the-art coilable space structures including ROSA, Caltech SSPP, and Star Shade [32, 33, 86–91]. Multiple point designs for these structures exist at several scales. The following specific instantiations, corresponding to the largest versions of these structures, are selected for study: iROSA (18 m × 3 m, considering only half of the system as the entire structure is stored in two separate rolls) [92], SSPP (60 m × 60 m) [33], and HabEx Star Shade (52 m diameter) [32].

Table 6.1 shows the relevant dimensions and properties, including the length of the coiled structure, L, the mandrel diameter, D_i, the outer diameter of the coiled structure, D_o, and the mass of the coiled structure, m_s. Note that m_s is the best estimate of the mass of the coiled structure alone, excluding the mandrel, based on reported areal densities, power densities, or directly stated mass metrics.

Table 6.1: Estimated Parameters for Coiled Space Structures

Structure	L	D_i	D_o	m_s
iROSA	3.0 m	0.5 m	0.8 m	25 kg
Caltech SSPP	1.0 m	0.4 m	1.6 m	500 kg
Starshade HabEx	3.0 m	1.5 m	4.0 m	1500 kg

Although these structures are anisotropic, i.e., composed of diverse materials, functional elements, and geometric configurations, for simplicity the coiled layers in this study are considered to be uniform, isotropic, and homogeneous, both materially and geometrically. The masses and dimensions in Table 6.1 can then be used to define the mean densities. Furthermore, although the structures under consideration include elements made of relatively stiff materials, such as carbon fiber or fiberglass, a relatively modest modulus of $E = 5$ GPa is assumed for the baseline configuration for all structures. This is within the range of stiffnesses previously calculated from a RVE of the Caltech SSPP structure in Section 2.4 (Table 2.4) and is considered to account for the reductions in stiffness caused by cutouts and other compositional discontinuities. With these assumptions, the coil is fully defined, and the remaining task is to finalize the mandrel design.

6.3 Design Study: Mandrel Sizing

After defining the design space for the coiled layer properties, the remaining decision is the configuration of the mandrel around which the layers are coiled. Using the coiling diameter of the reference structures in Table 6.1, the outer diameter of the mandrel can be determined. Thus, only the material and wall thickness of the mandrel need to be defined. To streamline the design process and create a generalized approach for all considered missions, aluminum has been selected as the mandrel material, owing to its widespread application as a structural material in aerospace. The last remaining choice is to select the mandrel wall thickness for each mission.

Solid aluminum cylinders are not viable for launch mass constraints. Launch loads often act as a critical determinant for structural sizing, and thus, they are assumed to be the primary driving requirement for mandrel sizing. Hence, the mandrel's wall thickness to support each configuration of the coiled structure is chosen so that it provides a 25% margin against yield ($\sigma_{y,Al6061} \approx 280$ MPa) under loading.

For this study, the mandrel margin is required to be compliant against two simultaneous loads: a transverse, quasi-static acceleration and an external pressure load. The amplitude of the transverse acceleration loading is equivalent to typical, sinusoidal acceleration launch loads while accounting for dynamic amplification, which generally exceeds prescribed steady state acceleration loading [8, 93]. The external pressure loading arises from the wrapping pressure from the coiled structure.

The mandrel sizing simulation study is performed in ABAQUS on a 3D model of a shell mandrel. This study continues to focus on the configuration where an isotropic mandrel is fixed in a cantilevered arrangement with a tip mass denoted as m. The mandrel is characterized by its length L, outer diameter D_i, and wall thickness t_m. End stiffeners hold the mandrel circular. For this design study, the coil structure is not incorporated. Instead, its inertia is introduced as a non-structural mass applied on the mandrel. Furthermore, the point mass, m, situated at the mandrel's tip is assigned a mass equivalent to that of a solid, aluminum end cap disk, with a thickness equal to the wall thickness of the mandrel.

The analysis is performed in a single static analysis step, with the transverse loading and wrapping pressure applied concurrently. The magnitude of the transverse static loading is 100 g applied as a gravity load, which is equivalent to a sinusoidal load of 1 g with 0.5% damping [94, 95]. This represents an extremely conservative design, where the coil is assumed to act only as an added mass that provides no damping, to

ensure the mandrel has adequate margin regardless of the behavior of the wound roll in later simulations. The wrapping pressure assumed is 500 kPa, which is well under the critical buckling load of a cylinder under external pressure for all configurations considered [96]. The peak Mises stress, σ_{max}, is extracted to calculate the margin, assuming a factor of safety of $FoS = 1.2$, given by:

$$\text{Margin} = \frac{\sigma_{y,Al6061}}{\sigma_{max} * FoS} - 1 \geq 25\% \tag{6.1}$$

For each of the configurations considered in Table 6.1, the design study is performed by running the loading conditions against a range of mandrel thicknesses from 1 mm upwards. Figure 6.1 shows the calculated margin for a range of mandrel wall thicknesses for each point design considered, assuming the corresponding added mass estimates of the coil in Table 6.1. The mandrel thickness is given by the intersection of the margin curve with the 25% level, Fig. 6.1.
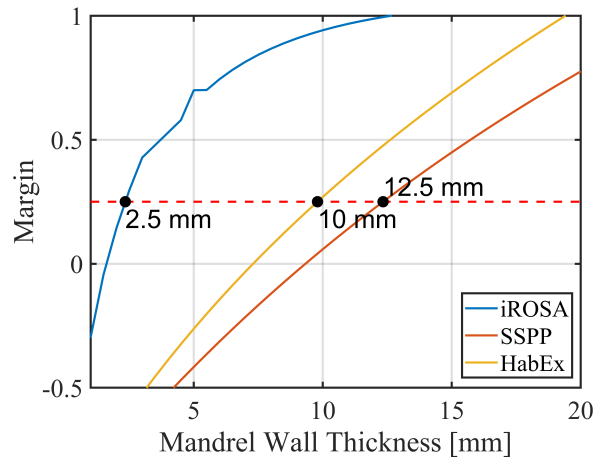
Figure 6.1: Mandrel wall thickness design studies for each point design.

Table 6.2 summarizes of the mandrel properties described by the following metrics:

Mandrel aspect ratio, AR, defined as the ratio between length and mandrel outer diameter:

$$AR = \frac{L}{D_i} \tag{6.2}$$

Mandrel-structure mass ratio, MR, defined as the ratio between mandrel mass, m_m, and the structure mass, m_s:

$$MR = \frac{m_m}{m_s} \tag{6.3}$$

Mandrel-structure thickness ratio, TR, defined as the ratio between mandrel wall thickness, t_m, and the coiled structure thickness, t_s, which is found by taking half the

difference between the estimated outer diameter of the coil from the outer diameter of the mandrel from Table 6.1:

$$TR = \frac{t_m}{t_s} \tag{6.4}$$

Mandrel-structure diameter ratio, DR, defined as the ratio between the coiling diameter (mandrel outer diameter), D_i, and the coiled structure outer diameter, D_o:

$$DR = \frac{D_i}{D_o} \tag{6.5}$$

Mandrel bending stiffness, k, using the modulus of aluminum for E and the second moment of area of each cylindrical cross-section, I:

$$k = \frac{3EI}{L^3} \tag{6.6}$$

Table 6.2: Mandrel Properties and Metrics

Mission	L [m]	D [m]	m_t [mm]	AR	MR	TR	DR	k [kN/mm]
iROSA	3.0	0.5	2.5	6.0	1.2	0.015	0.625	1.0
SSPP	1.0	0.4	12.5	2.5	0.1	0.02	0.25	60.0
HabEx	3.0	1.5	10.0	2.0	0.25	0.01	0.375	100.0

Table 6.2 shows that the considered configurations span a wide range of wound roll geometries. Having established the geometry and material specifications for the point designs, the mandrel design study is concluded, paving the way for the full characterization study of the wound roll.

6.4   Finite Element Simulation of Wound Roll Damping at Realistic Scales

For the vibration performance study, the coiled structure solid is incorporated into the model specified in Section 6.3. The simulation is performed on a simplified 3D model of a wound roll, composed of a cylindrical solid concentric with the shell mandrel. Informed by earlier studies, which highlighted the mandrel-inner layer interface as the most susceptible to slip, here, the assumption is made that there is no slip within the coil, allowing it to be modeled as a solid. In this manner, the only slipping interface is along the mandrel-inner layer boundary. In contrast to previous simulations, which exclusively utilized shells elements for the lab-scaled model, the increased total thickness of the coils requires using solid elements.

The coiled structure solid is assumed to be isotropic, with the outer surface of the coil solid being preloaded with a pressure loading σ_r. The coiled structure is defined

by length L and thickness, t_s, as illustrated in Fig. 4.1. The inner diameter of the base of the coil was assumed to be bonded to the mandrel's base. The mandrel was modeled using S4R shell elements and the coil layer solid was modeled with C3D8R solid elements.

The interaction between the innermost coil layer and the mandrel was specified with the following contact definition. In the normal direction, the contact condition is set to enforce hard contact, meaning that no penetration is allowed, while still permitting separation. The friction model for the tangential direction is defined by a Coulomb penalty friction model, with coefficient of friction μ. No other form of damping is included.

As previously stated, the friction capacity, which is the amount of force an interface can support until slip occurs, is assumed to be equal to the product of the coefficient of friction and the preload for the Coulomb-like model, $\sigma_c = \mu\sigma_r$. Although there are multiple degenerate combinations of μ and σ_r that result in the same friction capacity, the reduced-order model makes it clear that preload influences the state of stress in the wound roll, and consequently impacts its stiffness, and therefore affects the vibration response. Thus, variations in both the friction and preload parameters must be studied independently. For the coefficient of friction, this study assumes the contact surfaces can be engineered to have arbitrary friction properties and uses $\mu = 0.25$ for the baseline simulation case. The variation in the vibration response of the simulated coil with friction capacity is the focus of this study, so a range of preload values is considered.

The procedure for this simulation is as follows. First, a static analysis was performed to apply the initial preload of the coil layer solid against the mandrel. In the next dynamics implicit step, the assembly was subjected to an acceleration base excitation profile and time integration of the model response was carried out. In order to obtain the frequency response, a sinusoidal base acceleration excitation using a 0.5 g geometric chirp from 5 to 160 Hz over a period of 20 s was applied. The output of the sweep simulation reports the time history of the tip response of the coil-mandrel system, as well as the base input. The Fourier Transform of the tip response and base input, and subsequent ratio between the two provides the transmissibility response spectrum in the frequency domain, where the damping is estimated using the half-power bandwidth method at the resonant frequency.

6.5 Base Configuration Simulation Results

Transmissibility Response Variation with Preload

The variations in vibration response with preload of the baseline configurations of the coiled structures are shown in Fig. 6.2. These plots show the transmissibility of the mandrel tip response as a function of the input frequency for different preloads, and are largely included in this raw form for full transparency to provide an initial insight. From these frequency responses, the variation in the estimated damping with resonant frequency is shown in Fig. 6.3, which presents the trends in a more standard format. While the attenuation observed in the dataset generally exceeds the levels where the 3 dB method is understood to be accurate, damping is estimated using this method in a manner that provides a conservative estimate. Appendix D discusses the approach and reasoning behind this choice.
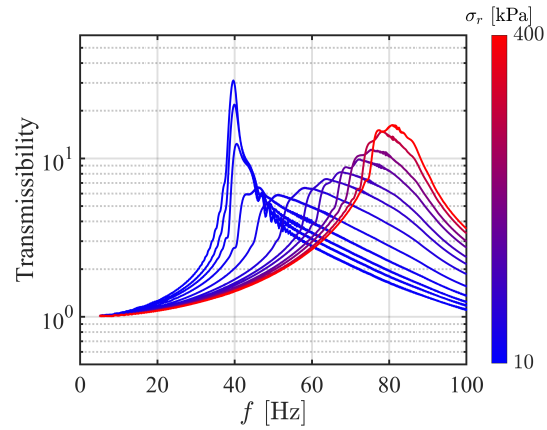
(a) iROSA scale
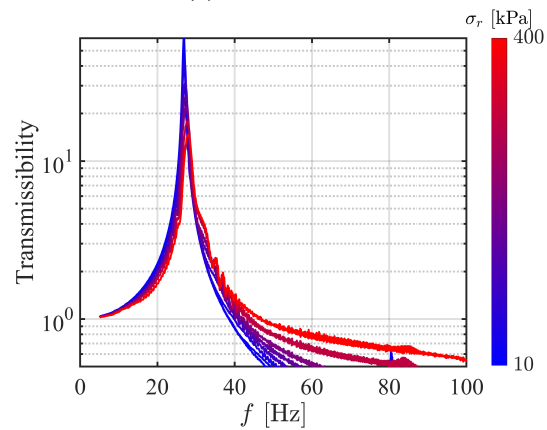
(b) SSPP scale
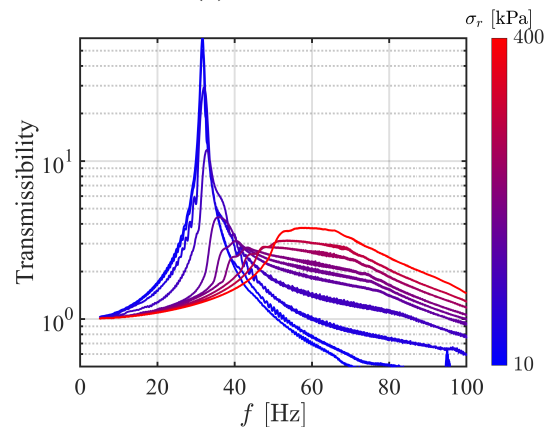
(c) Starshade HabEx scale

Figure 6.2: Transmissibility variation of baseline configurations with preload.

In Fig. 6.3, the vibration response of the structures at low preloads shows the lowest damping and lowest resonant frequency. In all three of these cases, the lowest preload case (10 kPa) does not correspond to the highest damping and exhibits the highest amplitude response. An indication of this effect, where the lowest preload
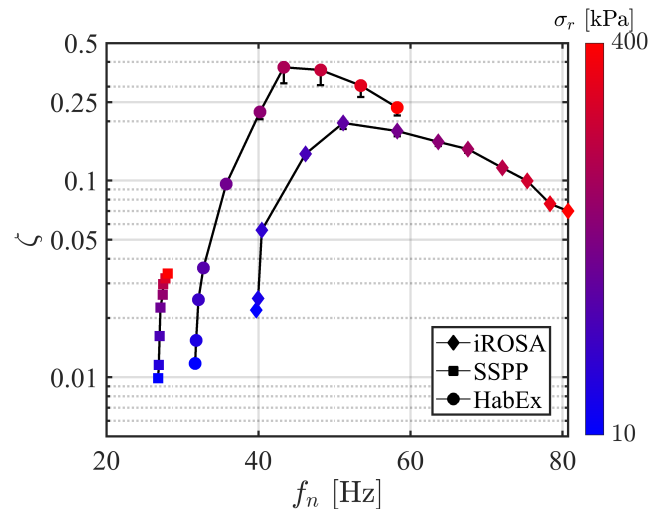
Figure 6.3: Damping (ζ) and resonant frequency (f_n) variation of baseline configurations with preload.

does not necessarily result in the lowest response, was similarly observed in both laboratory scale simulations and experiments as indicated in Fig. 5.6.

For two configurations, iROSA and HabEx, increasing the preload results in increasing damping up to a critical preload point, beyond which the damping decreases. These observations are consistent with the general characteristics of friction damping, where there exists an optimal preload configuration which results in the maximum possible damping [68]. This phenomenon arises from the inverse relationship between the shear capacity, which controls the prevalence of slip, and the work done by friction, both of which are governed by the preload magnitude.

The amount of energy dissipated by friction is determined by the work done by friction forces when slip occurs. At lower preload, the shear capacity is reduced, meaning slip is more likely to occur. However, the overall work done is reduced due to the lower preload. Conversely, higher preload increases the shear capacity and results in less frequent slipping. One might assume reduced slip should always result in lower energy dissipation; however, while slip initiation is more difficult, when slip does occur, proportionally more work is done due to the correspondingly higher forces. Because there is an inverse correlation between slip extent and work done, an optimal preload level that balances the two quantities exists. This phenomenon provides insight into why damping levels do not exhibit a substantial decrease despite an overall reduction in slip at higher preload levels.

Beyond the maximum damping point, the vibration responses of the iROSA and

HabEx scaled structures demonstrate characteristics observed in previous laboratory-scale experiments: increasing the winding tension above this value results in an overall increased stiffness, but corresponds to decreasing damping. Of particular note is that both the iROSA and HabEx scale structures are able to span a wide range of resonant frequencies with preload variation. The SSPP scale structure on the other hand is confined to a relatively narrow frequency range. For the SSPP configuration, the range of preloads considered has not led to a reversal in damping-resonant frequency; however, there is an observable trend that possibly indicates a plateau in the behavior.

Energy Dissipation Correlation with Damping Level

Fig. 6.4 plots the frictional energy dissipation in Joules against the corresponding damping ratio extracted for each structure configuration. Immediately noteworthy is the maximum energy dissipation for all structures is less than 1 kJ over a 20 s duration sweep. This suggests that the damping provided by this concept at realistic scales does not produce significant amounts of heat.

Unlike the lab-scale simulation results in Section 4.3, the correlation in peak damping versus energy dissipation is much less clear. Previously, while the configuration with maximum energy dissipation did not correspond to the highest damping ratio estimate, energy dissipation was observed to be strongly correlated with the damping estimate for the lab scale simulations. This trend is not observed for the realistic scaled simulations (Fig. 6.4).

However, focusing solely on total energy dissipation fails to acknowledge the variations in stiffness among different configurations, which leads to distinct resonant frequencies. While the exponential sine sweep profile employed in both experiments and simulations excite an equal number of cycles at each frequency, the duration of a 'cycle' depends on the frequency. Functionally, this indicates that less time is spent at higher frequencies compared to lower ones. In the case of the wound roll damper, the most significant dissipation rates occur at resonance, where the extent and magnitude of slip are the largest. Because the stiffness, and therefore the resonant frequency, vary with preload, meaningful comparison of total energy dissipated can be obtained with suitable normalization that accounts for the differences in displacement and time between configurations. Here, energy dissipation in Joules is converted to power dissipated per meter squared by dividing the work done by friction, extracted from the simulation, by both the square of the peak tip
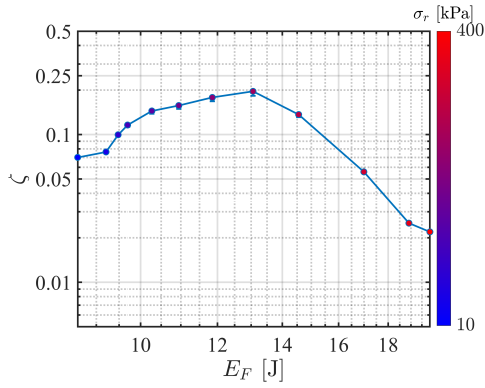
(a) iROSA scale
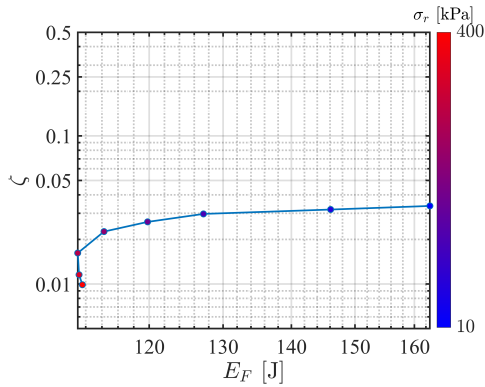
(b) SSPP scale
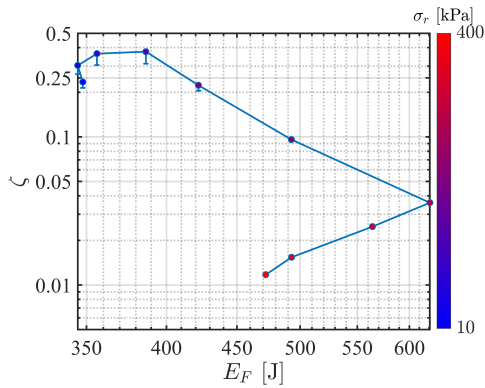
(c) Starshade HabEx scale

Figure 6.4: Damping ratio (ζ) variation with frictional energy dissipation of baseline configurations with preload.
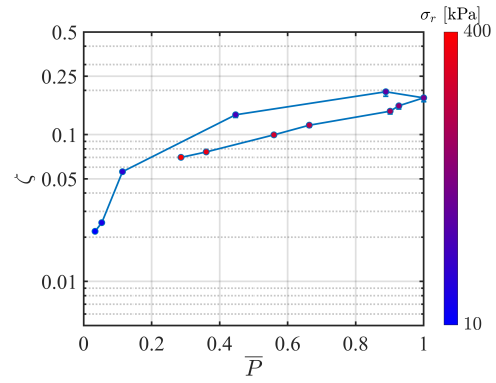
(a) iROSA scale
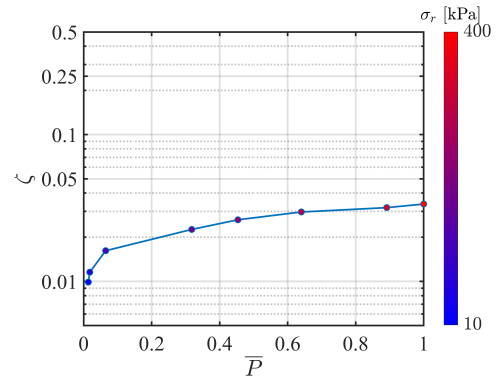
(b) SSPP scale
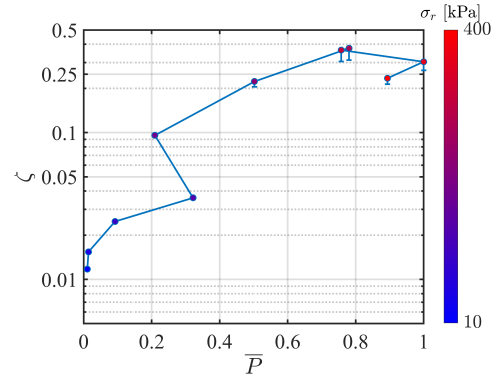
(c) Starshade HabEx scale

Figure 6.5: Damping ratio (ζ) variation with normalized power dissipation per meter squared of baseline configurations with preload.

displacement, x_{tip}, and the resonant frequency, f_n:

$$P = E_F / \max(x_{tip}^2) / f_n \tag{6.7}$$

This relation is analogous to an alternative definition of the damping ratio for

oscillators, which relates the power dissipated to the energy stored [97]:

$$\zeta \propto \frac{\text{Power Dissipated}}{\text{Energy Stored}} \tag{6.8}$$

Power dissipated is obtained by relating the total energy dissipated to the natural frequency of the system. The square of the maximum tip displacement observed is used as a proxy for the strain energy of the model at resonance.

Fig. 6.5 plots the damping ratio against the normalized power dissipated per meter squared, $\overline{P}$. Similar to the laboratory-scale simulation, the maximum damping observed does not precisely align with the peak power dissipation across all scenarios. Nonetheless, higher damping is observed to be strongly correlated with this rescaling of frictional work that takes into account the different stiffnesses and time scales between configurations. This result reaffirms that the reduction in response amplitude provided by this damping concept at real-world scales predominantly stems from frictional dissipation.

Despite the variation in responses between these structures, a significant amount of damping can be achieved where friction alone provides the energy dissipation mechanism. The minimum damping ratios observed is $\zeta \approx 1\%$ and significantly higher damping configurations exist and are achievable by varying the winding tension only.

In concluding, the geometric benefits of utilizing a coiled structure as a structural element have been demonstrated at large scales with the observed resonant frequency increase with winding pressure, while still maintaining elevated levels of damping. These results suggest that the performance of the wound roll damping concept is viable at practical scales. To gain a deeper understanding of how variations in these configurations influence the difference in responses, sensitivity studies are explored in the next section.

6.6 Sensitivity of Wound Roll Damper Performance

The objective of the sensitivity studies is to understand the relative effects of varying the simulation parameters on the vibration response of the wound roll configurations. A secondary objective is to determine whether the sensitivity studies can explain the different behavior of the SSPP structure observed thus far compared to the other two configurations. Specifically, the SSPP structure exhibits responses within a relatively narrow range of stiffness observed through resonant frequency measurements, as

well as the absence of a clear demonstration of the optimal preload for achieving maximum damping. These behaviors are not observed in the other two cases.

For sensitivity studies, the approach is to examine how varying the design and properties of the coiled structure affects the vibration response of the system. In these studies, the mandrel design remains fixed, as geometrically, the coiling diameter of a structure undergoing coiling is typically determined by the minimum safe change of curvature for the structure [98]. Thus, only adjustments to the materials and geometry of the coil are considered. For the design variation of a real structure, materials can be changed, the arrangement and continuity of materials can be adjusted, the contact properties between the structure and the mandrel can be modified, and the size of the final deployed structure can be altered to achieve larger or smaller coiled dimensions. The net effect of these design variations in real space result in variations in the effective bulk stiffness of the coil, the coefficient of friction, and the outer diameter of the coil when translated into the context of the simulation framework in this study. Therefore, the three parameters under consideration for the sensitivity studies are the structure homogenized modulus E, the coefficient of friction μ, and the structure thickness scaling factor s (Fig. 6.6).
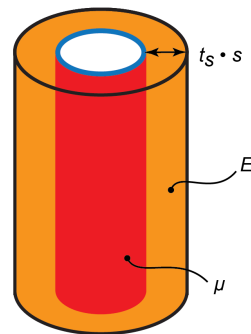
Figure 6.6: Wound roll sensitivity parameters under study: homogenized modulus E, coefficient of friction μ, and structure thickness scale factor s.

To study the effect of the coiled structure's stiffness and the friction between the coil and the mandrel, values that bracket the baseline configuration are selected, reflecting either more conservative estimates or more finely engineered configurations. For the size sensitivity study, the structure coil thickness is modified by a scaling factor s to vary the outer diameter. This can be thought as studying the sensitivity of vibration performance to the deployable structure size. When utilizing coiling as a packaging scheme for deployable structures, expanding the size of the final deployed

structure can often be achieved by simply incorporating additional layers in the coiled configuration. At the time of writing, the reference structures for the baseline configurations represented the largest concepts proposed for each configuration. Therefore, only scaling down from these baseline configurations is considered.

The simulation was rerun for different parameters as shown in Table 6.3. The new sensitivity study data is plotted with the previous results and shown in Fig. 6.7, Fig. 6.8, and Fig. 6.9, in terms of the raw responses. Fig.6.10 reanalyzes the data presented in Fig.6.9 in relation to shear capacity. To better highlight the underlying trends, the maximum damping for each configuration can be extracted, along with its corresponding resonance frequency, and plotted in Fig. 6.11.

Table 6.3: Sensitivity Studies

Sensitivity Study	s	E [GPa]	μ
Baseline	1	5	0.25
Stiffness	1	1, 10	0.25
Friction	1	5	0.125, 0.5
Size	0.25–0.75	5	0.25

From the stiffness sensitivity study in Fig. 6.7 and Fig. 6.11a, the dominant effect of this parameter is to shift the resonant frequency of the coiled structure assembly. In general, the peak damping achievable decreases as the structure becomes stiffer, but remains within the same order of magnitude across a wide range of moduli values. This result is consistent between all structure configurations and indicates that the rate at which damping changes with coiled structure modulus is low. In certain configurations, substantial changes in the overall assembly stiffness can be realized by adjusting the effective modulus of the coiled structure, while minimally impacting damping performance. Notably, the stiffness of the structure is not observed to affect the overall shape of the damping-resonant frequency response curves for the SSPP size structure (Fig. 6.7b).

In Fig. 6.9, the damping response curves for different coefficients of friction exhibit a significant degree of overlap, although not necessarily at the same preload value. This is to be expected, since the shear capacity for the Coulomb-like friction model is given by the product of the coefficient of friction and the preload. In the test cases considered, there are several different combinations of μ and P that result in the same shear capacities. This effect is better shown in Fig. 6.10, which plots the damping ratio against the shear capacity.
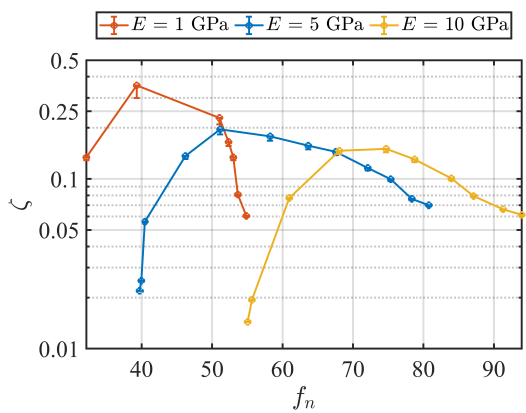
(a) iROSA scale
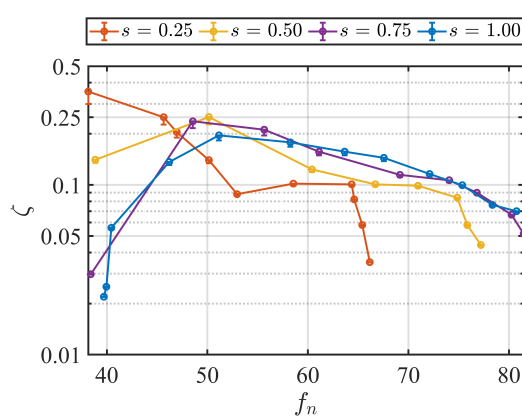
(a) iROSA scale
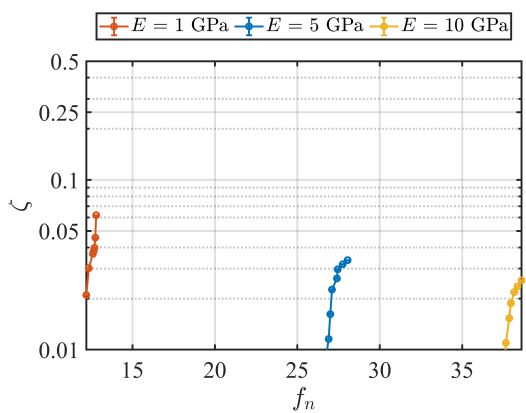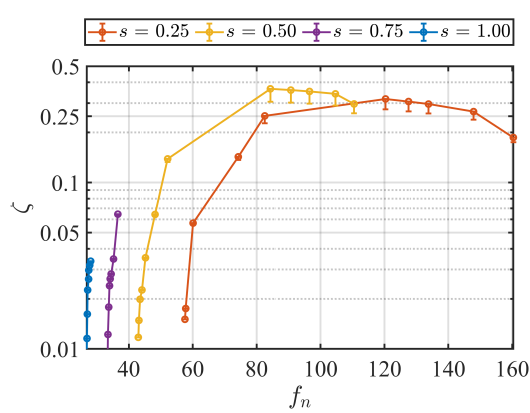
(b) SSPP scale
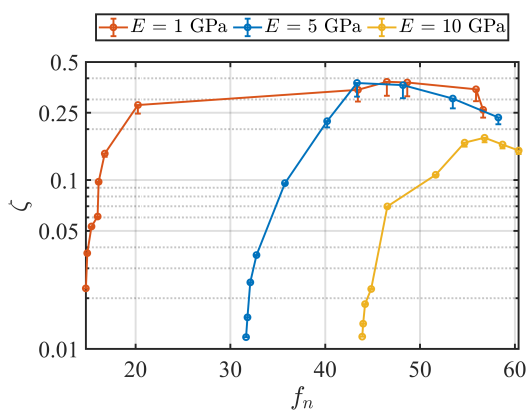
(b) SSPP scale

(c) Starshade HabEx scale
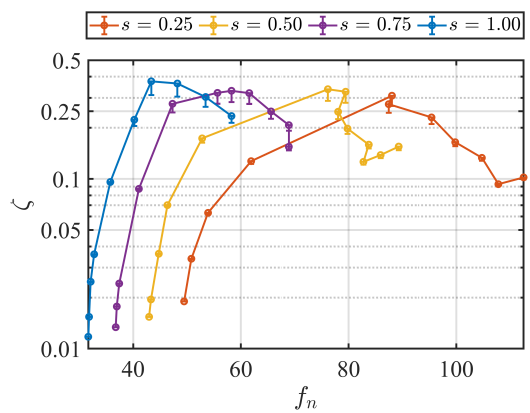
(c) Starshade HabEx scale

Figure 6.7: Stiffness Sensitivity Study

Figure 6.8: Size Sensitivity Study
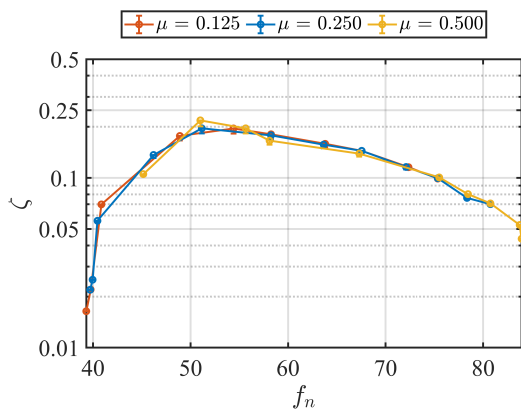
(a) iROSA scale
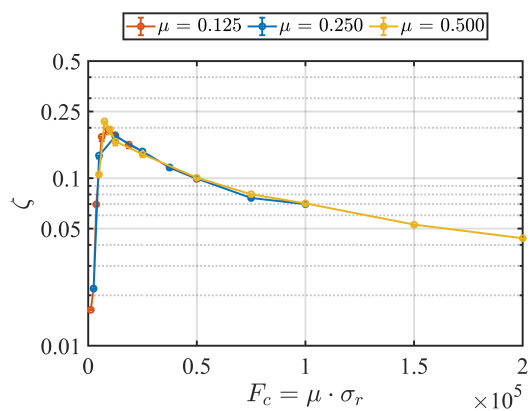
(a) iROSA scale
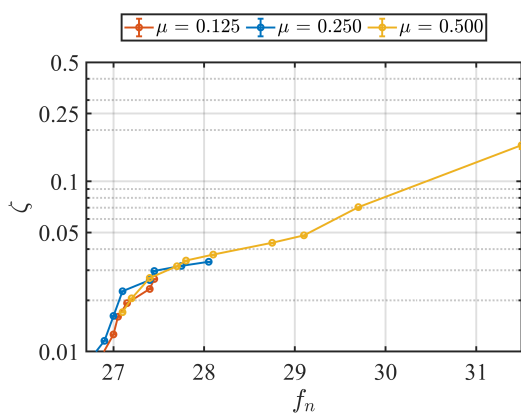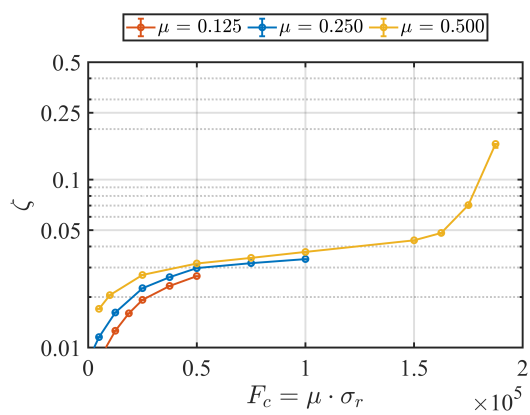
(b) SSPP scale

(b) SSPP scale
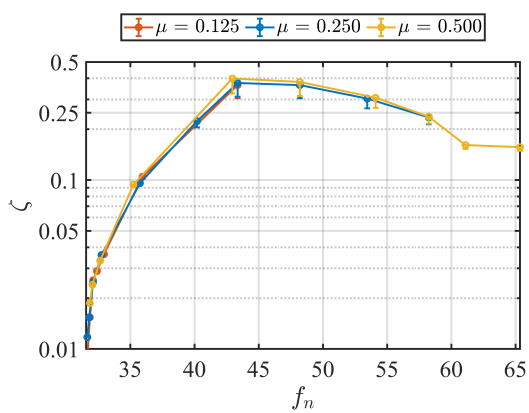
(c) Starshade HabEx scale
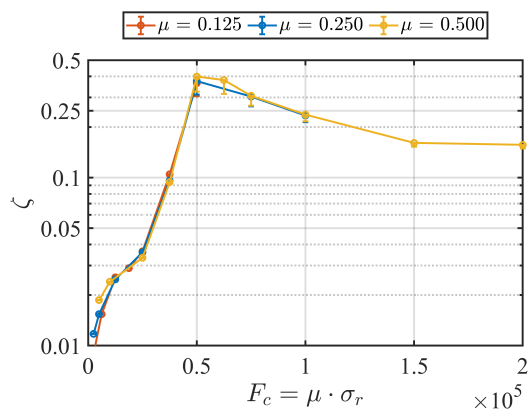
(c) Starshade HabEx scale

Figure 6.9: Friction Sensitivity Study

Figure 6.10: Damping variation with shear capacity.
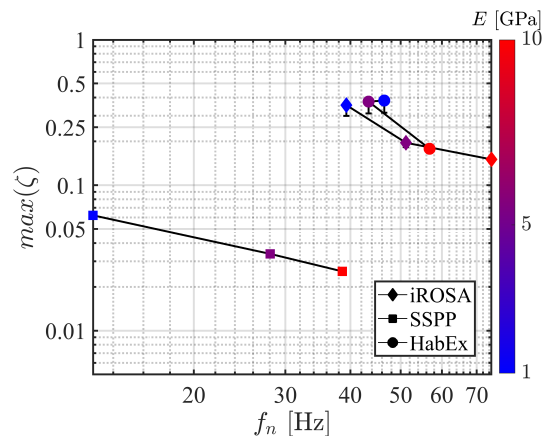
(a) Stiffness sensitivity study
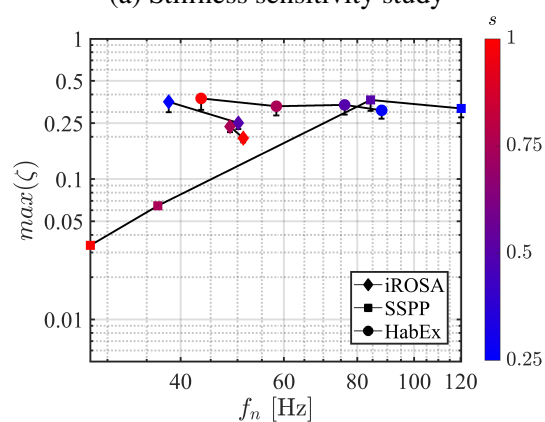
(b) Size sensitivity study
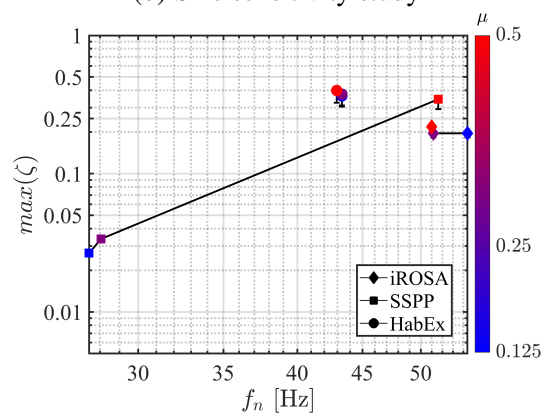
(c) Friction sensitivity study

Figure 6.11: Maximum damping and corresponding stiffness sensitivity trends.

For the iROSA scaled structure, the responses at identical shear capacities coincide almost exactly (Fig. 6.10a). With the SSPP and HabEx scaled structures, there are slight offsets between the curves (Fig. 6.10b, Fig. 6.10c). This data illustrates that, despite anticipated redundancy, the vibration performance in all cases may not be attributed to the shear capacity value by itself. Instead, the response might exhibit

some dependence on the individual values of the friction and preload. This result is not surprising, as the preload changes the stress state of the system, which is observed to affect the system stiffness. For the iROSA and HabEx scaled structures, the maximum damping achieved is not significantly affected by the coefficient of friction (Fig. 6.10a, Fig. 6.10c). However, with the SSPP structure, the range of damping increases significantly for the highest coefficient of friction considered, at the largest preloads (Fig. 6.10b). This sensitivity to shear capacity is believed to be related to the different behavior of this structure observed in Fig. 6.3 and will be discussed next.

For the size sensitivity study, three different behaviors are observed in response to scaling of the structure size (Fig. 6.8, Fig. 6.11b). With the iROSA scaled structure, there is comparatively little change in damping and resonant frequency with size (Fig. 6.8a). This is in contrast to the SSPP structure, where the amount of damping increases drastically as the structure becomes smaller (Fig. 6.8b). Here, note that the shape of damping-resonant frequency response curves now exhibits the expected behaviors for the small structure sizes, $s \in (0.25, 0.5)$: a much wider range of resonant frequencies are observed with the responses demonstrating an optimal preload value for peak damping. For HabEx, the dominant effect of scaling the structure is to simply shift the vibration response to the right towards higher frequencies as the structure size decreases, with no major changes in the maximum achievable damping (Fig. 6.8c). As the dimensions of the structure reduce, the inertial loading on the mandrel is reduced, leading to an increase in the stiffness of the system.

Having finally achieved similar behaviors between the structures with the above size sensitivity study, this result suggests that they are related to size or mass. In order to explain the different sensitivities observed, the metrics comparing the mandrel to the structure in Table 6.2 are revisited.

The most compelling metrics to explain the different behaviors between the structure configurations were the diameter and mass ratios, DR and MR. The diameter ratio provides a measure of the relative sizes of the structure and mandrel: as the diameter ratio decreases, the structure tends to become larger than the mandrel. The mass ratio provides a measure of the relative masses of the structure and mandrel: as the mass ratio decreases, the structure tends to become heavier than the mandrel.

Fig. 6.12 plots the diameter and mass ratios, DR vs. MR, which compare the relative sizes and masses of the structure and mandrel.
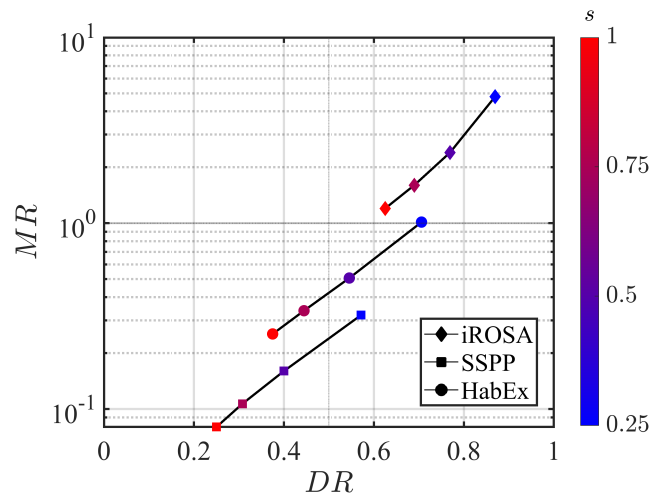
Figure 6.12: Diameter ratio vs. mass ratio for three structures.

For the iROSA case, the mass of the mandrel dominates, as $MR > 1$ for all cases. Additionally, the mandrel is a significant fraction of the structure size, with $DR > 0.5$. This indicates that the vibration response of this structure is expected to be mandrel dominated, which supports the trends observed in the sensitivity studies, where the response was relatively insensitive to the structure properties.

The HabEx case is intermediate in terms of both size and loading. The mandrel is about the same size as the structure, as $DR \approx 0.5$. However, for smaller sizes, the overall structure mass decreases and becomes comparable to that of the mandrel. This potentially explains why there is only a shift in resonant frequency.

The SSPP structure is an order of magnitude lower in terms of mass ratios and relative size. This indicates that the mandrel is supporting a mass much heavier and larger than itself, and hence the response is dominated by the coil loading the mandrel. This explains the unique behavior observed in the friction sensitivity study in Fig. 6.10b, where higher shear capacities result in stronger coupling between the coil and the mandrel. As the structure becomes smaller, these effects are reduced. This suggests that the vibration response sensitivity is dependent on the relative size of the mandrel support and the coiled structure loading. Note that even though the mandrel design against the applied loading was conservative, demonstrating positive margin for extremely low damping, it is not necessarily optimized to take best advantage of the wound roll damping concept. This result provides an interesting consideration for redesign.

These sensitivity studies provide additional evidence that the wound roll damping concept has many features that naturally lend themselves to scaling with material,

geometry, and contact parameters.

6.7   Conclusion

In this study, simulations were used to investigate the efficiency of the wound roll damping concept in realistic contexts, considering recent state-of-the-art deployable structures for space. The structures considered covered a range of structural parameters, including aspect ratios, sizes, and mechanical properties. The findings of this study confirm the potential of the proposed damper concept in achieving substantial levels of damping in practical contexts. The lowest level of damping recorded was around 1%, with many potential configurations surpassing this value by an order of magnitude. These damping levels are of practical interest as they provide a substantial decrease in vibration response at resonance, with certain configurations approaching virtually no amplification across the tested frequency range. Furthermore, the examination of energy versus damping demonstrated that the performance of this damping concept is achievable without generating significant amounts of heat.

The observed benefits of the damping concept at practical scales were not limited to damping alone. The coiling form factor's geometric considerations enable embedded adjustability of the apparent stiffness in the coiled structure, providing a dual advantage in structural design. This adjustability was demonstrated by shifts to higher resonant frequencies with preload. These findings were consistent in all the concepts considered.

The sensitivity of the damping concept to changes in structural stiffness, size, and coefficient of friction was further explored. A noteworthy observation is the difference in sensitivity between the structures considered. This aspect was notably emphasized in the study of structure sizes, revealing a range of sensitivities among the different configurations, spanning from nearly invariant in the iROSA case to highly responsive in the SSPP case. This indicates that the performance of this concept is sensitive to the relative size and mass between the mandrel and the coiled structure. The sensitivity study also highlights another crucial aspect, which is that identical friction capacities resulting from different combinations of preload and coefficients of friction may not yield identical vibration responses in all cases.

A notable aspect of these results is that the damping levels observed in this study were achieved simulating only one slipping interface. While the wound roll damping concept can provide scalable damping with excitation through the propagation of slip to additional layers, this study indicates that significant damping can be attained

without additional interfaces. In this work, the coiled structure was treated as a homogenized solid, where no slip is assumed inside the coil and slip only occurs between the innermost layer and the mandrel. Thus, having only one friction interface is demonstrated to be sufficient, where only the movement and deflection of the mass and stiffness of the coil as a bulk entity is utilized in this concept. From a practical standpoint, this result holds significance for mission designers concerned about potential damage from interlayer slip between sensitive surfaces or active components within coiled layers. Thus, the wound roll damping concept can be employed, even when all layers within the coiled structure are fully constrained, by incorporating a sacrificial interface on or between the innermost layer and the mandrel.

The results of this study provide compelling evidence for continued development of this damping concept through experiments at scale.

C h a p t e r   7

CONCLUSION

This research set out to accomplish four main objectives.

1. Understand the physical mechanism of this concept by creating a theoretical approach to determine conditions where slip is or is not expected.

2. Experimentally assess the effectiveness of this concept in reducing vibration responses.

3. Discover how to model and simulate the behavior of this damping concept.

4. Assess whether this damping concept addresses the issues identified with other types of dampers.

To address the first objective, the interlayer shear capacity of a wound roll was compared against the expected stress distribution during vibration. The interlayer shear capacity was determined by using stress field analyses, which estimated the radial stresses at any location inside the wound roll due to tension winding. Utilizing a Coulomb friction model, scaling these radial stresses by the coefficient of friction provided the shear capacity, which is an estimate of the shear stresses a layer can sustain without slip. From simple analytical studies and FEA, the magnitudes and locations of stress that would result in interlayer slip from vibration loading were compared against the shear capacity. For configurations that excite bending modes of a wound roll supported by a cantilevered mandrel, slip is expected to initiate at inner layers, towards the root. The extent of slip is determined by a coupling between the winding preload, vibration loading level, and structure properties. From simulation studies performed, it is expected that the winding preload can have a significant effect on the effective stiffness of the wound roll, which impacts the vibration response.

The second research objective was achieved by designing a small scale wound roll test sample; a process that was informed by understanding gained during the first objective. The design of the wound roll test article was sized specifically to maximize the vibration response sensitivity to winding tension stress state for a relatively small number of wound layers. The wound roll consisted of 25 layers of continuous Kapton

membrane wound around a polycarbonate mandrel. This test sample was subjected to vibration testing using a variety of waveforms and excitation levels to experimentally assess the effectiveness of this concept in reducing vibration responses. From these results, the vibration performance of this concept was confirmed. Here, the wound roll damping concept was demonstrated to reduce the amplitude of response irrespective of loading waveform type and loading rate, showing sensitivity only to excitation level. Performance was observed to be sensitive to loading magnitude, as the level of damping increased as excitation level increased. Additionally, the resonant frequency of the overall system could be modified by varying the winding tension. Interlayer slip was directly measured using high speed cameras, where the magnitude of slip correlated directly with the damping level and inversely with winding tension.

The behavior of this concept was captured via two approaches: finite element simulations and a reduced order model. The finite element simulations were performed in 3D and consisted of an inner cylindrical shell, that represented the mandrel, and outer concentric shells or solids that represent coiled layers. The reduced order model was a 2-DoF system that is composed of two mass-spring-damper systems in frictional contact. Both models were demonstrated to achieve good correlation with experimentally measured wound roll vibration response, capturing qualitative and quantitative features. A significant amount of understanding was achieved during the development of these models. Both of these models only simulate a single slipping interface, but are able to capture the damping magnitude, indicating that the innermost layer of the wound roll damper provides a significant amount of dissipation in this concept. Additionally, the shape of the responses, namely the positive skew for low winding tensions, was discovered to primarily result from the nonlinear variation with winding tension of the stiffness of the wound roll as well as the degree of mass loading that the roll applies to the mandrel. The FEA simulations further provide additional evidence of the self-scaling nature of this concept, as the propagation of slip through different layers and axial extents are directly observable.

Finally, the performance of the wound roll damping concept, measured through experiments and simulations, was assessed against the limitations common to other dampers types. Ultimately, this damper is demonstrated to not be subject to the limitations affecting other dampers. The wound roll damping concept is observed to be a relative motion device, invariant excitation spectra, and self-scaling with excitation magnitude. Regardless of the loading rate or waveform, if the excitation

is large enough to cause interlayer slip, then friction dissipation will provide damping to the system. While stiffness and damping are still adversely related in this concept, large increases in overall stiffness, as measured by the resonant frequency, are achievable while maintaining significant levels of damping. Thus, this damping concept is an integral stiffness and damping scheme that is observed to be robust and scalable, providing tunable performance with winding tension. Furthermore, simulations indicate that this concept is viable at realistic scales, capable of providing significant damping and stiffness modification.

Future Work

This study exclusively focuses on wound rolls supported by a cantilevered mandrel, exploring solely transverse excitation and bending mode shapes associated with the first resonant bending frequency. While this may cover a wide range of applications, it by no means completely covers all the possible configurations. Exploring the efficacy of this concept across additional mode shapes, higher frequency modes, loading orientations, and mounting configurations would increase understanding of this damping concept.

This work assumes that wound rolls have continuous, large contact areas to work with. However, particularly for deployable structures, the object being coiled will not necessarily have uniform thickness resulting in intermittent points of contact. A natural extension of this work would be to study how well this concept performs with intentionally reduced contact areas. Similarly, the results of this work suggest that for a given level of excitation, only a partial region of the roll is actively engaged in slipping. Another possible avenue for research is to take this damping concept to the extreme, removing the wound roll entirely, and only putting material where slip typically occurs. While this may remove material that provides stiffness to the assembly, this approach aims to explore whether damping performance is influenced by the removal of non-slipping regions.

A third possible future research direction would be to study the effect of anisotropic configurations. The results of this research thus far generally only assume isotropic or homogenized wound rolls. Real structures, particularly deployable space structures, are not continuous, often having cutouts and other compositional discontinuities where stiffening elements are not uniformly distributed. Investigations can be conducted to identify whether the configuration or placement of stiffening elements could significantly impact the damping and stiffness capabilities provided by this

damping concept.

And finally, a potential avenue for future research is to determine the vibration performance of this damping concept through experiments at realistic scales. The simulations suggest that this concept is capable of providing significant damping and stiffness for some of the largest deployable space structures ever proposed. Experimental confirmation of these values would provide significant support for the widespread adoption of this concept for vibration mitigation.

A p p e n d i x   A

ELASTIC SLIP SENSITIVITY OF THE PENALTY FRICTION MODEL IN FEA

The penalty friction model used through this work for the tangential contact definition in FEA simulations is defined by the coefficient of friction, μ, and the allowable elastic slip, γ^* (Fig. A.1). Here, the allowable elastic slip is defined as the absolute magnitude of the allowable relative displacement that may occur before surfaces begin to slip. By default, the allowable elastic slip is typically set to a fraction of a "characteristic contact surface face dimension" [99]. Due to the vague nature of this definition and the fact that the initial results were inaccurate with the default setting, the parameter had to be manually configured.
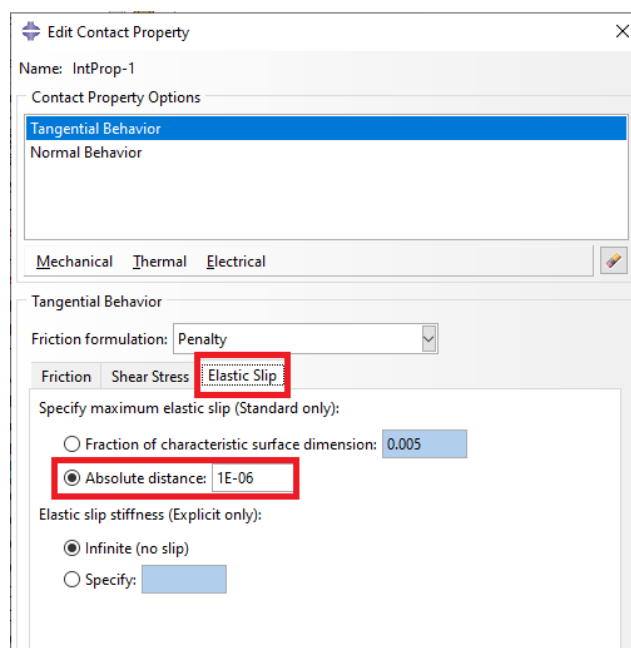
Figure A.1: ABAQUS setting for elastic slip γ^*. For the simulations in this work, $\gamma^* = 1$ µm.

Fig. A.2 demonstrates how the simulated wound roll vibration response changes for the lab scaled simulation, with preload $\sigma_r = 1$ kPa. The simulations begin to show better agreement with the experimental results for $\gamma^* \approx 1$ µm. Although the response appears to converge as the allowable elastic slip is reduced, further decreasing it results in a significant increase in simulation run time. As such, $\gamma^* = 1$ µm was

selected for all simulations presented in this work. Considering the experimentally measured magnitudes of slip, this value was deemed acceptable and justified based on data.
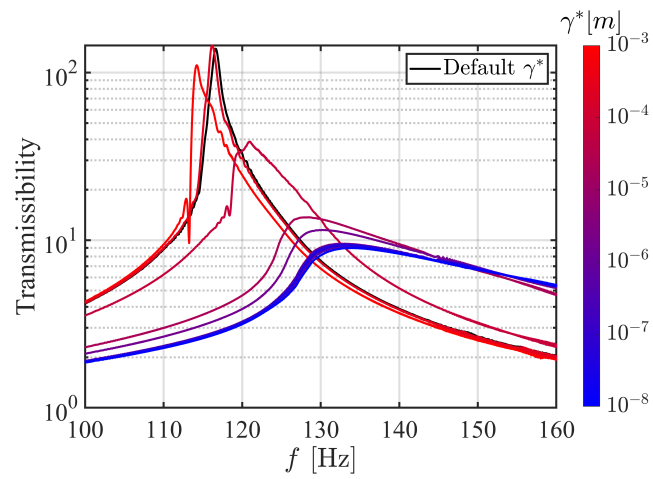
Figure A.2: Sensitivity of wound roll vibration response to γ^*.

A p p e n d i x   B

EFFECT OF NUMERICAL DAMPING ON WOUND ROLL VIBRATION RESPONSE

Although the FEA model used in this work specifically only incorporated friction contact for dissipation, it is essential to acknowledge that the chosen solution method for time domain dynamics introduces an additional damping source. Abaqus/Standard employs implicit time integration operators like the Hilber-Hughes-Taylor (HHT) or backward Euler, which may introduce numerical damping [100]. This damping arises from the approximations made during the discretization of continuous equations of motion into a discrete time-stepping scheme. These discretization errors can result in an artificial damping effect, causing the numerical solution's amplitude to diminish over time. This is acknowledged as a factor that may particularly impact simulations involving fluctuating contact conditions. Because the response transmissibility and damping levels due to contact friction are desired outputs of the simulation, the effect of the solver must be understood.

Fig. B.1 shows the default time integration methods available through ABAQUS CAE. The 'Transient Fidelity' and 'Moderate Dissipation' methods are HHT, and the 'Quasi-Static' method is based on backward Euler. The behavior of the HHT method is controlled by three parameters, (α, β, γ) [101]. In this context, $\alpha < 0$ introduces damping, while $\alpha = 0$ provides no damping. The default ABAQUS integration methods correspond to pre-programmed values of these parameters. ABAQUS also allows for direct specification of custom HHT parameters (Fig. B.2). Table B.1 shows the HHT parameters for the default ABAQUS integration methods, as well as the case for no damping.

The choice between integration method can affect both the simulation results and analysis computational efficiency. By default, ABAQUS uses Moderate Dissipation

Table B.1: Default parameters for the Hilber-Hughes-Taylor integrator.

Parameter	Transient Fidelity	Moderate Dissipation	No Damping
α	−0.05	−0.41421	0
β	0.275625	0.5	0.25
γ	0.55	0.91421	0.5
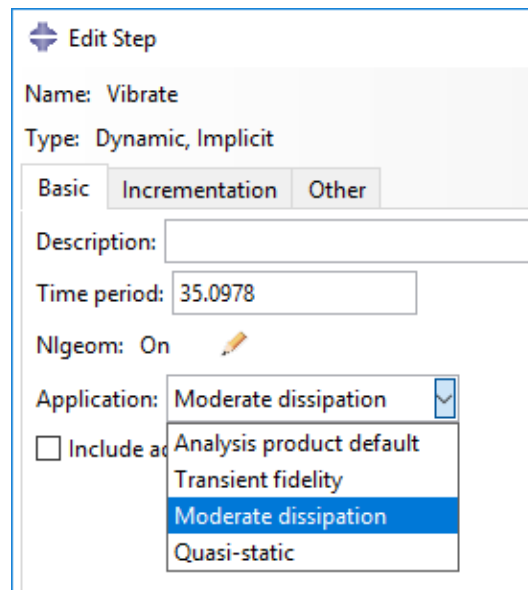
Figure B.1: Available ABAQUS dynamic implicit time integration methods: transient fidelity, moderate dissipation, quasi-static.
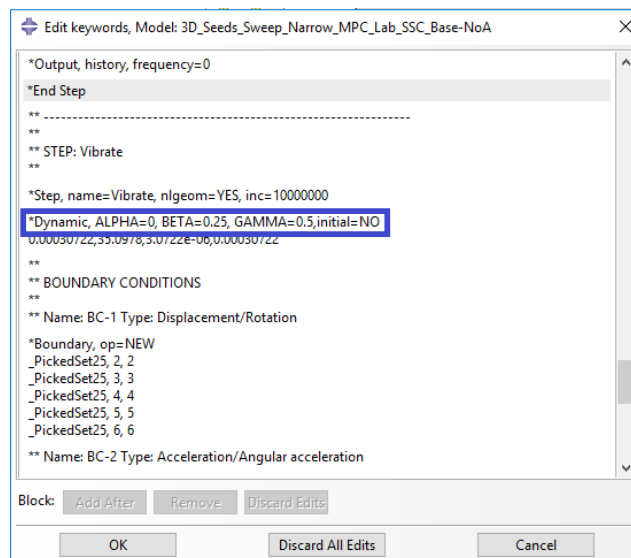
Figure B.2: Direct specification of Hilber-Hughes-Taylor integrator parameters through modification of ABAQUS keywords/input file.

for models that contain surface-based contact. The sensitivity of the wound roll vibration response to each of these integration methods was studied in order to determine the suitable integration method. Fig. B.3 shows the vibration response for the lab-scaled simulation (σ_r = 10 kPa, μ = 0.45) using each integration setting. From this plot, the Quasi-Static method does not demonstrate the expected vibration response. The backward Euler method used in the Quasi-Static operator is known

to be more dissipative than the HHT operator, and as such, excessive numerical damping severely attenuates the vibration response.

The HHT operators are observed to demonstrate the expected vibration response. Notably, there is no significant difference between any of the HHT methods, where the default ABAQUS methods are observed to be comparable to directly specifying the energy preserving integration method for no damping ($\alpha = 0$). Because increasing dissipation results in better computation efficiency, this work uses the default integration method (Moderate Dissipation) which provides the most numerical damping among the HHT methods studied and uses a more aggressive time incrementation scheme. Since the solution accuracy is not significantly affected, this study maintains the assertion that the simulation model incorporates no damping sources other than the contact friction interaction.
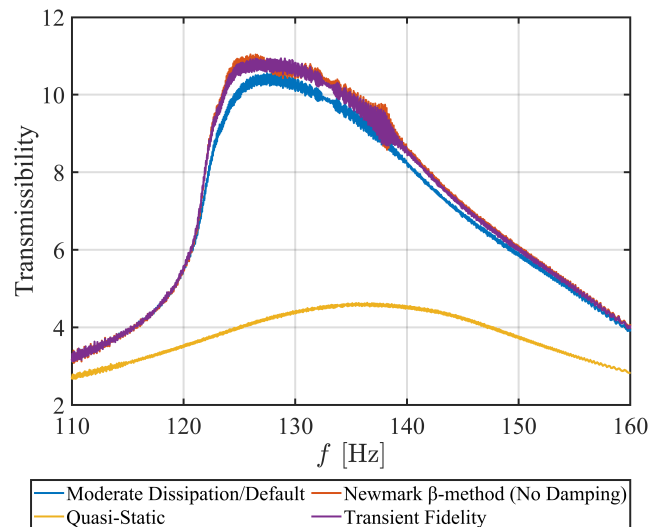
Figure B.3: Comparison of vibration response of lab-scaled simulation model ($\sigma_r = 10$ kPa, $\mu = 0.45$) for different integration schemes.

A p p e n d i x   C

2-DOF SIMULATION SENSITIVITY TO SMOOTH FRICTION MODEL

The numerical 2-DoF of simulation model utilized a smooth friction model based on the sigmoid function, $S(x)$, to address the numerical difficulties associated with the discontinuity of the Coulomb Friction model. The degree of deviation of the smooth model from the actual model can be controlled by incorporating a scaling factor, s, on the input variable, x: $S(sx)$. Fig. C.1 shows how the scaling factor impacts the accuracy of the smooth representation.
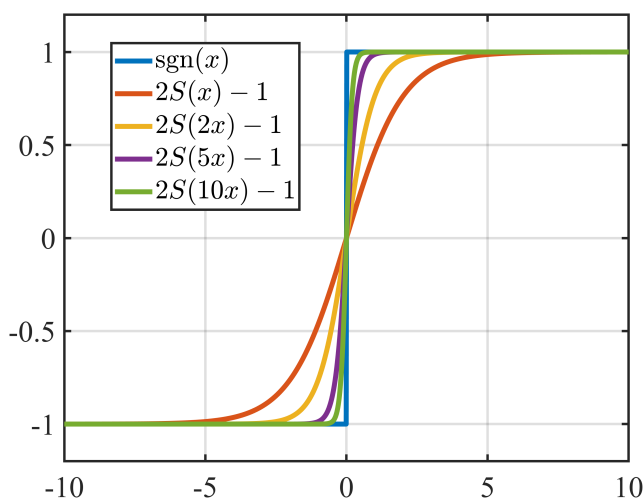
Figure C.1: Effect of scaling factor $s \in [1, 2, 5, 10]$ in representing the sign function.

The sensitivity of the 2-DoF simulation to the accuracy of the smooth friction model was studied for the correlated model described in Chapter 5, and the results are shown in Fig. C.2. In general, there is observed to be little difference in the range or variation of the response with the smooth friction scaling factor. However, beyond $s = 3$, the results start to show spurious spikes in the frequency responses. The incidence of these spikes increases both with preload for a given value of scale factor and with increasing scale factor. Because the incidence of these signals are sporadic and scale with preload, these likely indicate intermittent convergence issues with stick-slip. Since there is no observed impact on simulation accuracy, and the simulation runtime increases with scale factor, the default scale factor $s = 1$ was chosen.

(a) $s = 1$

(b) $s = 3$

(c) $s = 5$

(d) $s = 7$

(e) $s = 9$

(f) $s = 10$
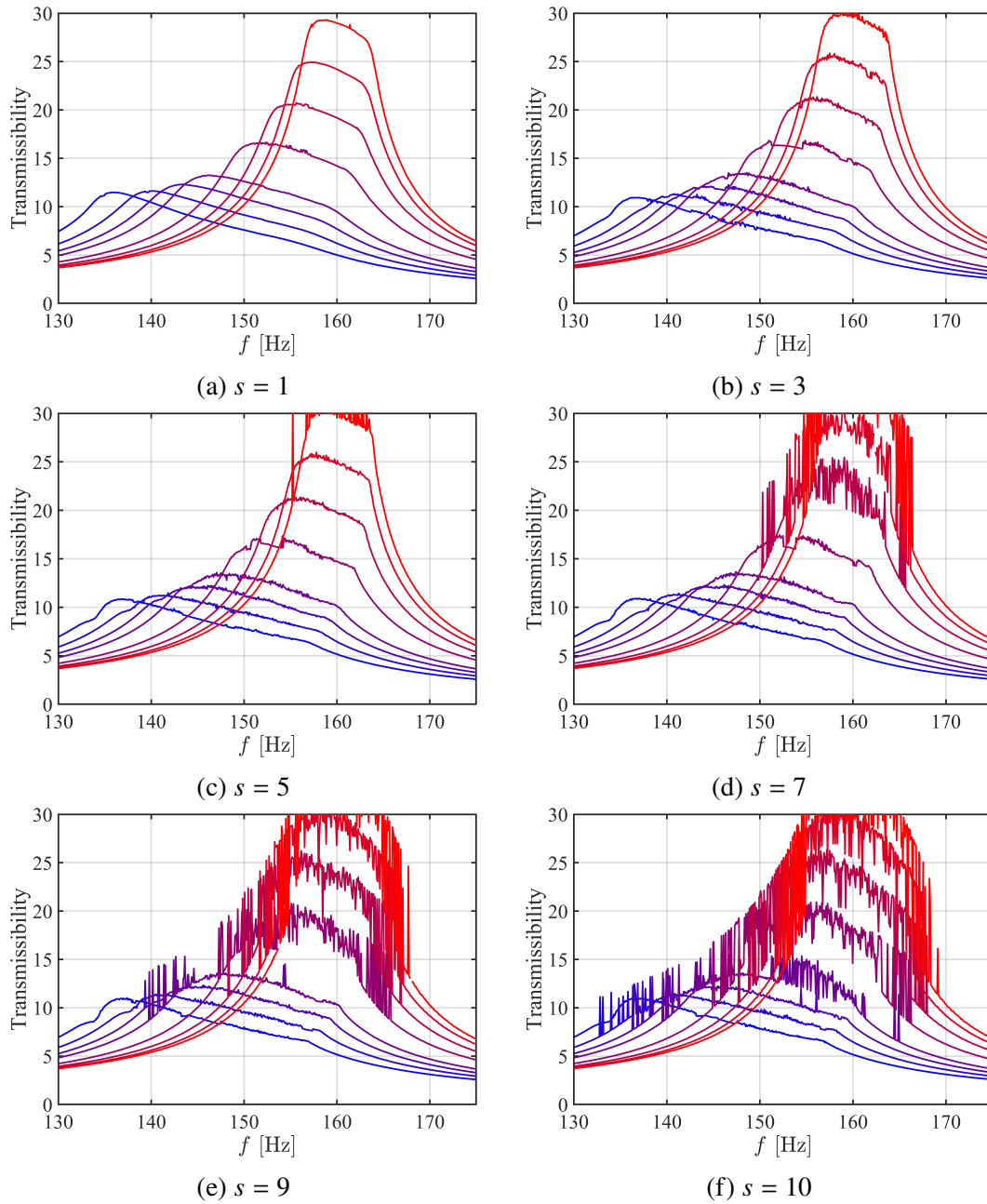
Figure C.2: Sensitivity of 2-DoF model simulation to smooth friction model scale factor, s. As s increases, the friction model increases in accuracy, but results in numerical instabilities of the overall simulation.

A p p e n d i x D

DISCUSSION ON SUITABILITY OF 3 DB DAMPING ESTIMATE FOR HIGH DAMPING

It is commonly asserted that the 3 dB method for damping estimation is only accurate for low damping values, $\zeta < 0.05$ [102]. However, in this research, vibration responses that demonstrate significantly higher attenuation have been encountered. While there are other methods of estimating the damping from frequency responses and other vibration data, the 3 dB method is an easy to implement, convenient measure that relates the response peak and the bandwidth. Thus, the 3 dB method enables useful relative comparisons between different responses, even if the damping estimate is not accurate. The utility of the damping estimate is also dependent on whether damping is over-predicted or under-predicted. In general, a conservative estimate that underpredicts damping, where the actual loads experienced are likely to be lower than predicted, is practically more useful than an over-prediction.

Another limitation with the 3 dB method is that this approach is most accurate for linear, single degree of freedom systems, whose responses demonstrate symmetry, or systems with modes that are sufficiently spaced apart. However, the wound roll damping concept demonstrates nonlinear, asymmetric responses as demonstrated by the positive skew responses at low preload. Additionally, damping can become so high that the transmissibility is nearly flat for a large frequency span, which can make it difficult to identify the resonant frequency of a highly damped configuration.

For these reasons, the general approach taken in this research to estimate damping from simulated and experimental frequency responses is to apply a curve fit to the data first, and then apply the 3 dB method to the fitted response. For this approach, if the peak response, ideally a resonant peak, has sufficiently high prominence and symmetry, i.e., for low damping, the 3 dB method is directly applied. However, for sufficiently damped responses, where the prominence of the resonant peak, if it is identifiable, or the symmetry of the response around the maximum response drops below a set threshold, the response is fitted to a Gaussian function. This approach ameliorates issues in damping estimation by providing a smooth, symmetric function that approximately captures the amplitude and bandwidth of the original data. The algorithm for this fitting procedure is shown below.

Algorithm 1 Frequency Response Curve Fitting

For a given frequency response (f, T), identify the peak response: $T_{pk} = \max(T)$.

    if T_{pk} prominence and symmetry > Threshold **then**

        Apply 3 dB method directly

    else

        Curve fit frequency response using GaussianFit(f, T)

        Apply 3 dB method to fit

    end if

Algorithm 2 GaussianFit(f, T): Fits a Gaussian function to frequency response data consisting of frequencies, f, and corresponding transmissibilities, T, in the neighborhood of the peak response.

1: For given frequency response (f, T), find the frequency corresponding to the peak response: $T_{pk} = \max(T)$, $f_{pk} = \operatorname*{argmax}_{f} T(f)$

2: Return the best fit Gaussian: $\tilde{T}(f) = a_1 \cdot e^{-\left(\frac{f - b_1}{c_1}\right)^2}$, calculated on the interval $(f_{pk} - d, f_{pk} + d) \in f$ obtained from:

$$\underset{d}{\text{maximize}} \quad \frac{d}{\text{RMSE}(T, \tilde{T}; d)}$$

$$\text{subject to} \quad \tilde{T}(f_{pk} - d) = \tilde{T}(f_{pk} + d) \leq \frac{T_{\text{pk}}}{\sqrt{2}}$$

$$\text{where} \quad \text{RMSE}(T, \tilde{T}; d) = \sqrt{\frac{1}{|d|} \int_{f_{pk} - d}^{f_{pk} + d} \left(T(x) - \tilde{T}(x)\right)^2 \, dx}$$

A question arises regarding the suitability of this method for accurately reflecting the frequency response. Note that although the frequency response plots demonstrate asymmetry and positive skew, it is important to realize that these plots do not have the same axes scales, and thus the asymmetry is exaggerated. For systems with even moderate damping, where the range of transmissibility, T, is an order of magnitude lower than the 3 dB bandwidth, Δf_{3dB}, the Gaussian fit is observed to be a good approximation to the frequency response in the neighborhood of peak response using any typical curve fitting error estimate. Here, the Root Mean Square Error (RMSE) is used in the GaussFit function (Algorithm 2).

Fig. D.1 compares the estimated damping of a 1-DoF mass-spring-damper system obtained from direct application of the 3 dB method and the approach where the frequency response is first fitted, and then the 3 dB method is applied to the fit. Observe that both approaches are relatively accurate in estimating the prescribed

damping value until $\zeta = 0.2$. Beyond $\zeta = 0.2$, the direct 3 dB method over-predicts the damping while the fitting method under-predicts. While error increases as damping increases, the fit method remains within the same order of magnitude up to relatively large damping values of $\zeta = 0.5$. Thus, the approach of first fitting the frequency response is used to provide conservative damping estimates used throughout this research. In all plots where damping is depicted with an error bar, this work adopts an additional conservative approach by assuming that the estimated damping is higher than the actual value and thus, the displayed estimate includes a lower bound error bar, derived from the error estimate in Fig. D.1.
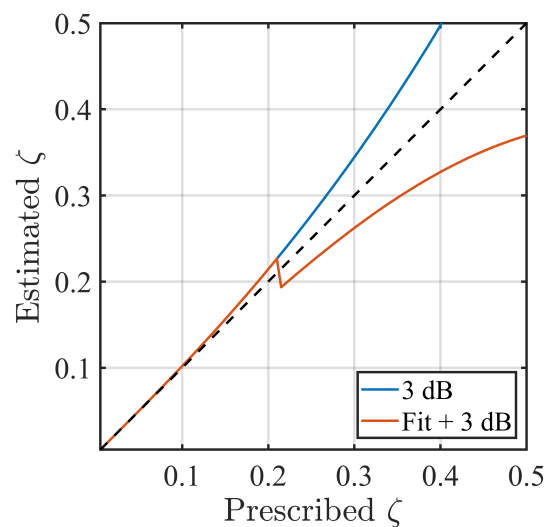
Figure D.1: Prescribed damping of a 1-DoF mass-spring-damper system $(m, k, \zeta) = (1, 1, \zeta)$ vs. damping estimated via: 1. Direct application of 3 dB estimate 2. Curve fitting, then applying 3 dB estimate on fit. After $\zeta \approx 0.2$, 3 dB method over-predicts while curve fit method under-predicts damping.

EXPERIMENTALLY MEASURED INTERFACE MECHANICAL PROPERTIES OF PRESTRESSED LAYERED SOLIDS (KAPTON)

E.1   Introduction

This body of work demonstrated that the vibration response of the wound roll damping concept is dependent on the effective mechanical properties of the coil. Both simulations and experiments indicate that the shear modulus of the coil can significantly affect the resonant frequency of the roll assembly. Additionally, the shear capacity between layers within the roll directly influences the occurrence and propagation of slip during excitation. The coil's mechanical responses to loading varies with interlayer friction forces, which are generated and controlled by the degree of preload and contact behavior between the interfaces that preload the individual layers into a prestressed, layered solid. The accuracy of simulation and numerical models depends on these properties; therefore, having models and measurements that closely approximate real behavior is crucial to obtain correlation between simulations and experiments.

There are numerous techniques available for measuring the mechanical properties of wound rolls, each with its own set of challenges and limitations. Some methods aim to measure these properties in situ from the wound roll, which has the advantage of accurately capturing the geometric configuration and boundary conditions of interest, as well as the state of stress from winding. However, a number of these approaches rely on indirect measurements, such as hardness, density, and acoustic methods, which require empirical conversions and correlations to the desired metrics [60]. While there are alternative direct in situ measurements, many of these methods ultimately focus on assessing the properties at specific layer interfaces within the wound roll, providing only single data points. For example, the core torque test and the axial press test directly measure the shear forces required to induce interlayer slip, but they can only do so at individual interfaces [45, 47].

An alternative approach is to study layered interfaces in a flat configuration rather than in the cylindrical geometry of fully wound rolls. Previous experiments, testing the mechanical response of preloaded layer interfaces, indicate several behaviors

and sensitivities of interest for the wound roll damping concept. Stack compression and bending tests reveal that moduli, recoverable deformation, and the overall force-deflection hysteresis behavior can vary significantly with the number of layers [50, 103]. Studying singular interfaces also provides valuable information, such as measurements of friction forces during slip, which can demonstrate complex behaviors that cannot be fully explained or approximated by the simple Coulomb model [104, 105]. Investigations into the frictional contact behavior between surfaces during slip highlight additional sensitives to factors such as loading rate and length scale dependence [54, 106–111].

In previous sections of this study, properties such as shear modulus and shear capacity were indirectly assessed using resonant frequency of vibration. Moreover, friction behavior was assumed to follow a Coulomb-like model. Thus, there is a gap in direct confirmation of how the shear modulus and shear capacity of the stack vary with preload prior to slip, as well as the suitability of Coulomb-like models for accurately describing the hysteretic force-displacement behavior during slip associated with the frictional damping concept. The objective of this section is to experimentally measure the mechanical properties of prestressed, layered solids that affect the performance of the wound roll damping concept with a focus on the sensitivities identified in previous studies such as dependence on number of layers and loading rates.

To do this, a mechanical shear testing device is designed in order to study both the aggregate behavior of layer stacks and frictional behavior of individual single layer interfaces through shear loading. In this section, the focus lies on the examination of Kapton layer stacks and the Kapton-Kapton interface motivated by the wound roll test sample used throughout this work. Among the existing methods and device architectures used to measure the desired tribological quantities [112], double direct shear testing (DDS) was selected. Based on this concept, the shear testing machine built consists of a shear platen with two actuators arranged in symmetric configuration that preloads a flat test sample against each side of the shear platen. The shear platen is then driven to shear the test samples, where force and displacement are recorded.

The selected double shear testing configuration offers several advantages. Firstly, having large contact areas is generally regarded to increase the sensitivity to friction forces by averaging friction force measurements over larger surfaces as compared to other point contact based tribometers [60, 113]. Moreover, unlike single shear

setups, this configuration provides a symmetric and balanced design, simplifying fixture design. And finally, in contrast to gravity-based methods such as the inclined or horizontal plane and pulley-based designs, the double shear configuration allow for driven forcing which enables more complex loading profiles and adjustable loading rates.

Several loading profiles are utilized in this study, including step velocity and constant velocity loadings, which are the most common and generally occur at fairly slow speeds. Additionally, a sinusoidal profile is included to provide data at higher loading rates. Several metrics are of interest in these experiments include the variation of shear modulus with preload, shear capacity, hysteresis behavior, and load rate sensitivity.

E.2 Experiment Setup

The chosen experimental setup, double direct shear testing (DDS), commonly referred to as shear sandwich testing, is a method typically employed for assessing the shear strength of materials and determining the coefficient of friction between surfaces (Fig. E.1). The DDS fixture used in this work consists of two double acting pneumatic cylinders that are mounted to a stainless steel support bar interacting with an aluminum shear platen (Fig. E.2). The piston of the pneumatic actuators are supported by ball bearing carriages that interface with a linear guide rail that is likewise attached to the stainless steel support. The purpose of the linear rail support is to prevent vertical deflection of the contact surfaces driven by the pneumatic cylinders in response to shearing forces applied by the movement of the shear platen.

In this implementation, a pair of identical test samples is positioned on either side of the shear platen. The test fixture then applies normal stresses through the two pneumatic cylinders to press the test samples up against an axial shear platen. The pressure setpoint of the pneumatic cylinders is controlled via an SMC ITV1050-01N2S4 electro-pneumatic digital pressure regulator (Fig. E.3).

(a) Undeformed.

(b) Deformed.
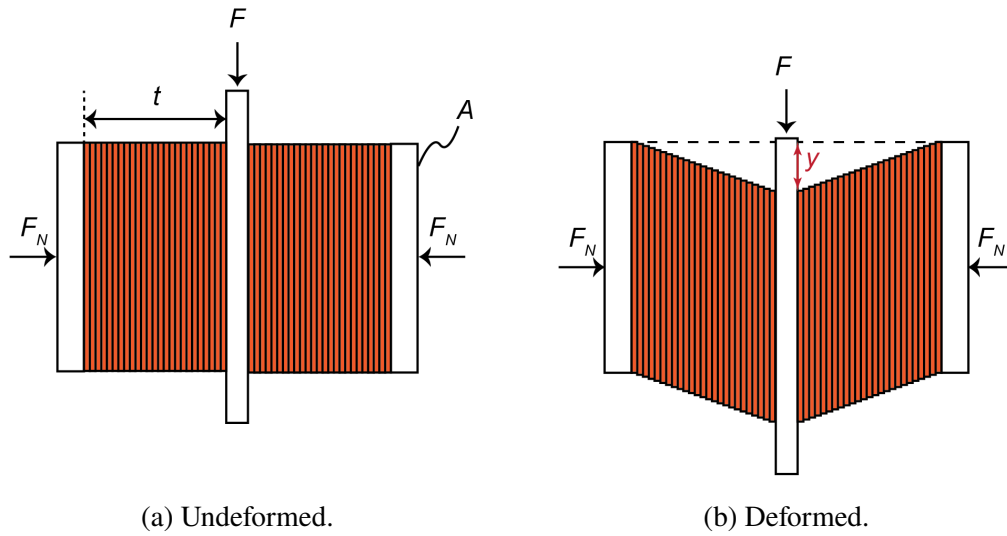
Figure E.1: Double Direct Shear schematic.

(a) Retracted pneumatic actuators.

(b) Extended pneumatic actuators.
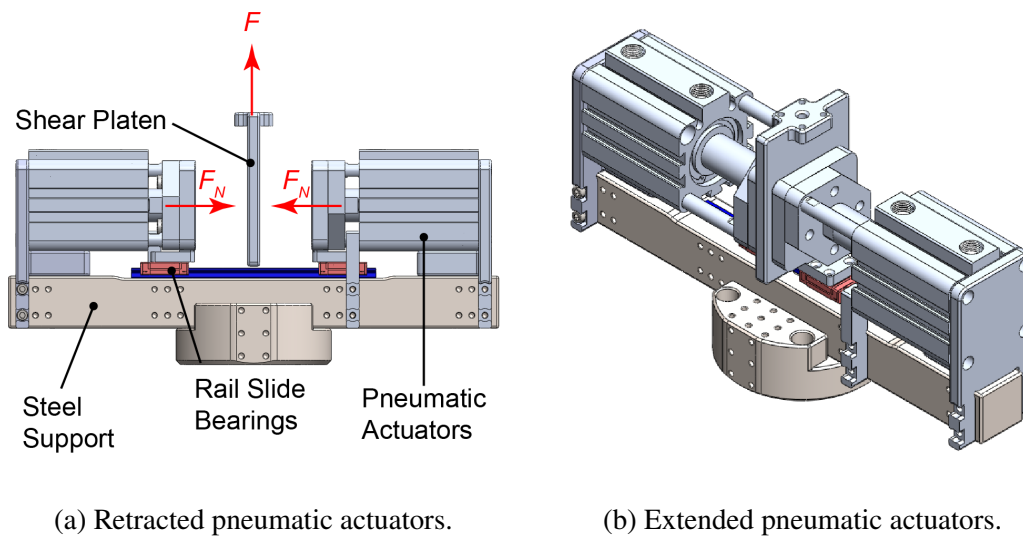
Figure E.2: Double Direct Shear testing fixture with normal preload pneumatic actuators retracted and extended.
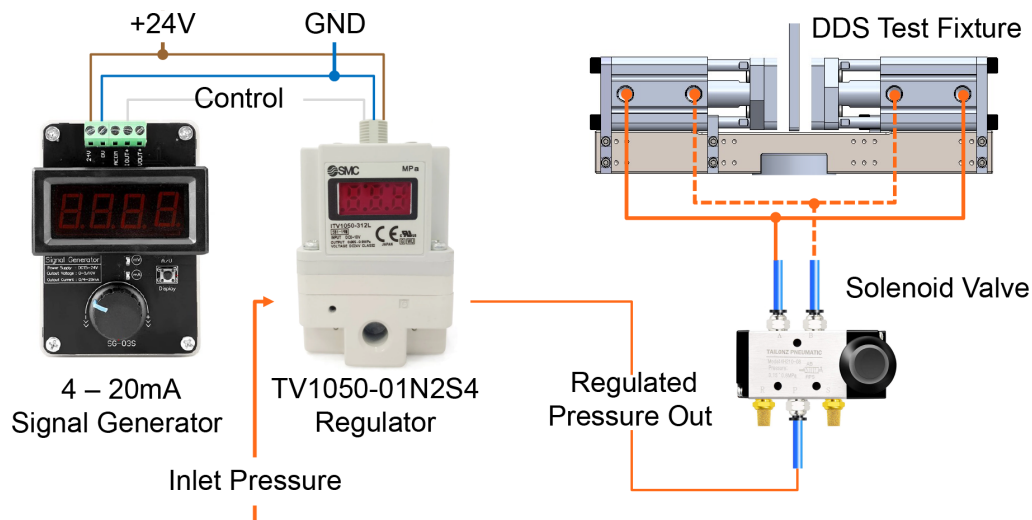
Figure E.3: Pressure regulation connection diagram for DDS test fixture.

The shear platen is connected to an actuator with a load cell and displacement sensor which measure the shear forces F and the displacement y. The actuator is then driven to apply shear loads to the test sample. The shear fixture is used with two different testing machines, which provide the shear platen actuation and measurement acquisition. The first testing machine is the Instron 5569 which is utilized for step velocity and constant velocity experiments (Fig. E.4a). Because the Instron 5569 is rate limited, with a peak velocity of approximately 8 mm/s, the Electroforce 3200 Dynamic Mechanical Analyzer (DMA) is employed as the second testing machine to support sinusoidal loading profiles at higher loading rates (Fig. E.4b). The Electroforce 3200 has a load capacity of 225 N and a frequency range of 100 – 300 Hz.

(a) Instron 5569 Universal Testing Machine.

(b) Electroforce 3200 Dynamic Mechanical Analysis (DMA) Tester.

Figure E.4: Testing machines used for measurement of mechanical properties of prestressed layered solids (not to scale).

Similar to the vibration experiment, the layer samples under test are 2 mil thick Kapton®HN sheets that are cut to match the area of the contact surfaces of the pneumatic pistons, approximately 45 mm x 45 mm. Additionally, to ensure that all slipping interfaces are Kapton-Kapton, the aluminum contacting surfaces of the DDS fixture are covered with adhesive-backed Kapton Fig. E.5.

Pneumatic contact surfaces
45 mm x 45 mm
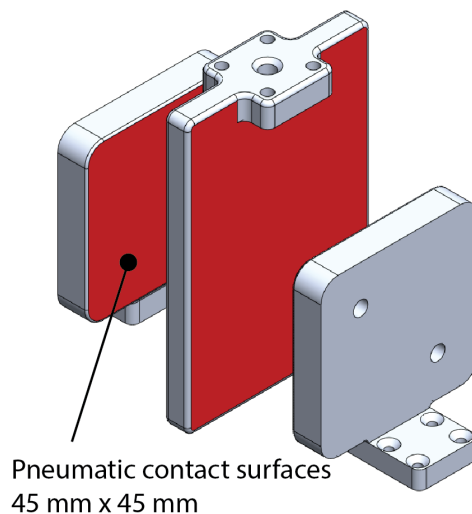
Figure E.5: Contacting surfaces of the DDS test fixture. Surfaces highlighted in red are covered with adhesive backed Kapton to ensure only Kapton-Kapton interfaces between all contact surfaces.

E.3   Shear Modulus and Shear Capacity of Preloaded Layers Prior to Slip

This work first begins by studying the mechanical response of preloaded stacks of multiple layers under shear prior to the onset of slip, as depicted in Fig. E.1 using the Instron testing machine. In these experiments, two identical stacks of layers are placed into the test fixture and preloaded with pressure, which varies for each test case. In this scheme, there is a uniform normal preload F_N applied to all layers. The shear platen is then driven at a constant, force controlled loading rate of 1 N/min from experiment initialization until large scale slip is observed. Initial, exploratory testing indicated that macro-scale slip is clearly identified by either a sudden drop in force or a sudden increase in displacement rate of the Instron actuator. The Instron is programmed to terminate the test if it detects either a force drop above 1 N threshold or a displacement beyond 1 mm. The maximum force the stack can support before the onset of macro-scale slip is defined as the shear capacity:

$$\max F\big|_{\text{prior to slip}} = F_c \tag{E.1}$$

Although the wound roll vibration experiment involved 25 layers, here significantly larger layers are considered to determine the sensitivity of the loading response to the number of layers. Fig. E.6 shows force-deflection curves for multiple repeat trials of 50 and 100 layers of Kapton under a range of different normal preloads. Note that the normal preloads F_N are converted into stresses σ_N assuming the

full contact area is active and constant (Fig. E.5) to facilitate comparisons with interlayer pressures from wound roll experiments. The force-deflection response exhibits minor initial non-linearity, which is assumed to be a consequence of effects such as fixture compliance because of the small displacement magnitude and force monotonicity up to the defined macro-scale slip event. Overall, there is a strong, approximately linear trend. From this data, the shear capacity is determined by identifying the maximum shear force before macro slip occurs (Fig. E.7), and the shear stiffness is obtained by from the slope of a linear fit of the force-deflection curves (Fig. E.8).
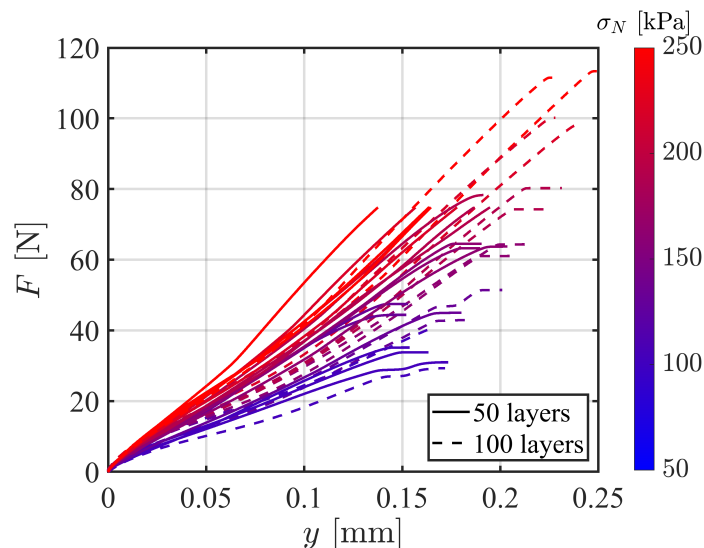
Figure E.6: Deflection vs. shear force trends for preloaded layered Kapton. Color gradient from blue to red denotes increasing applied preload. Solid lines corresponds to experiment performed with 50 layers. Dashed lines corresponds to experiment performed with 100 layers.

The macro-slip event is evident in Fig. E.6 by the abrupt transition to a horizontal trend, indicating that subsequent motion occurs at constant forces after the shear capacity is reached. Fig. E.7 shows how the shear capacity varies with applied preload from the pneumatic cylinders for the different number of layers considered in this experiment. Note that the 50-layer dataset is partially incomplete due to an oversight in the experimental procedure, where the loading profile was set too low to induce slip. Two observations are evident here. First, the shear capacity trend is approximately linear and increases with preload. Second, shear capacity does not appear to be sensitive to the number of layers in this experiment. This result is not unexpected, as the experimental setup uniformly preloads all layers in the stack.

Consequently, each layer interface should exhibit identical shear capacity regardless of the number of layers, assuming all other factors are equal. In these experiments, slip typically occurs directly at the shear platen.
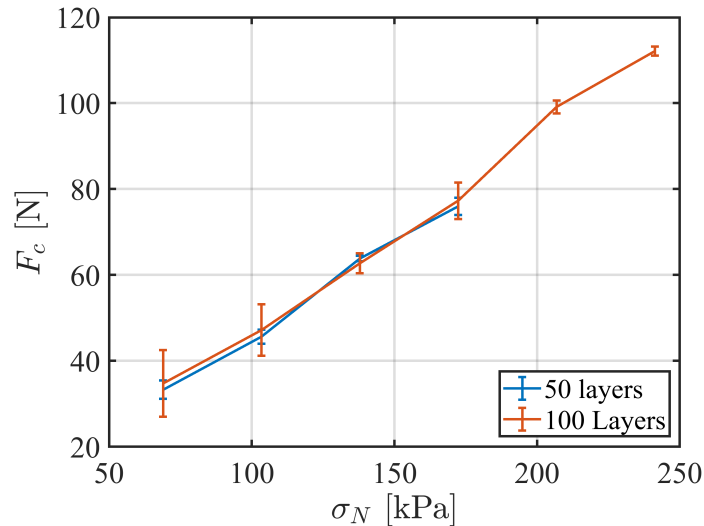
Figure E.7: Shear capacity vs. applied preload for layered Kapton. Shear capacity linearly increases with preload and is insensitive to the number of layers.

Fig. E.8 shows how the shear stiffness varies with applied preload from the pneumatic cylinders for the different number of layers considered in this experiment. Shear stiffness is observed to linearly increase with preload, as expected. Moreover, shear stiffness is observed to decrease with the number of layers. While more data would provide better indications of this trend, this is expected as shear stiffness is a length scale dependent quantity. Using the diagram in Fig. E.1a, the shear stiffness, K_s, for an object with effective shear modulus G, cross-section area A, and thickness t is given by:

$$K_s = \frac{GA}{t} \tag{E.2}$$

Under simple shear loading applied by the DDS test, increasing the number of layers increases the thickness of the assembly, which reduces stiffness.
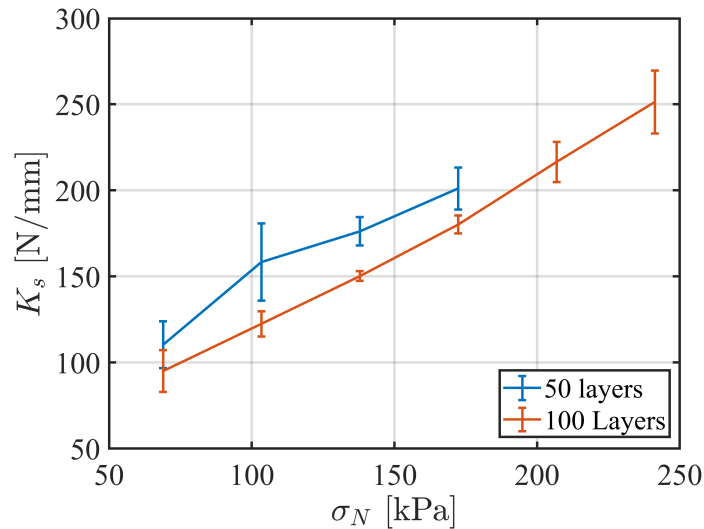
Figure E.8: Shear stiffness vs. applied preload for preloaded layered Kapton. Shear stiffness linearly increases with preload. Shear stiffness appears to reduce with number of layers.

Using Eq. E.2, a crude estimate for the shear modulus can be obtained, equivalent to taking the slope of the stress strain curve in accordance to the method listed in ASTM E143-20 [114] for the dimensions depicted in Fig. E.1a:

$$G = \frac{\tau}{\gamma} = \frac{F/A}{\Delta y/t} \tag{E.3}$$

This hinges on a significant assumption that the actual deformation of the stack linearly increases between the contact surfaces, allowing it to be approximated as simple shear. Fig. E.9 shows the variation in shear modulus with applied normal preload for different stack layers. Regarding sensitivity to number of layers, shear modulus appears to increase with the number of layers in the stack, which arises directly from the scaling with the stack thickness t. More data would be required to make conclusive statements on this trend. Under similar preloads, the estimated shear moduli are well within the range of apparent shear moduli estimated from simulations in previous chapters. However, there is an apparent underestimation of the maximum shear modulus, where the estimated ranges to approximately 10^7 Pa. One conjecture is that this discrepancy might stem from variations in boundary conditions between wound roll geometry and the flat test samples. The coil forms a continuous spiral, where any given section of the membrane is restrained by other sections of the coil, whereas the DDS test setup features unbounded, free edges (Fig. E.10). The implementation of boundary restraints has the potential to increase stiffness, and hence, estimated modulus from this approximation.
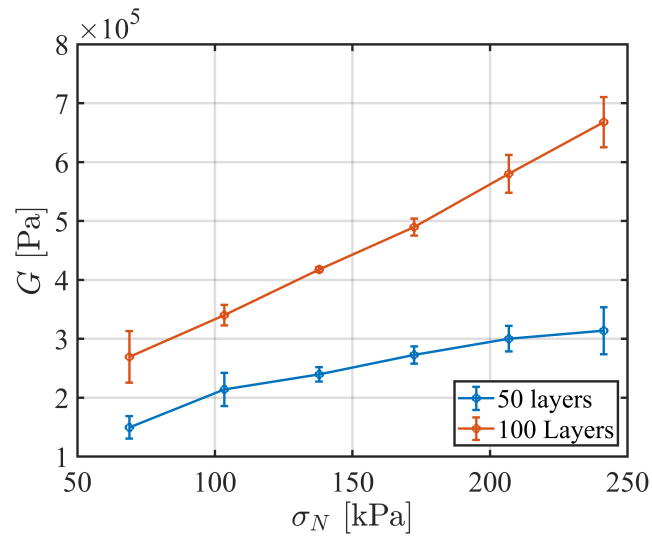
Figure E.9: Shear modulus vs. applied preload for preloaded layered Kapton. Shear modulus linearly increases with preload.
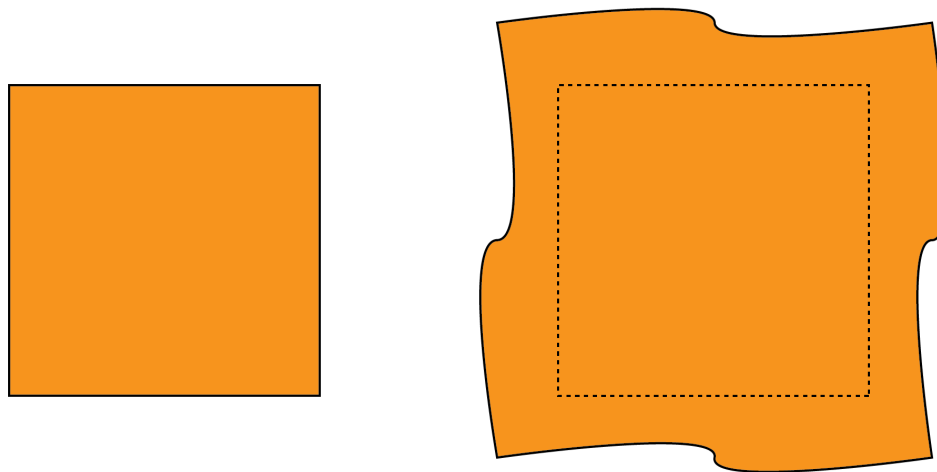
(a) Free edge boundary conditions of layer test samples in the DDS test.

(b) Constrained boundary condition typical of a given section of a wound roll layer located away from free edges.

Figure E.10: Different boundary conditions between segments in planar shear testing vs. wound roll geometry.

In general, there does not appear to be significant relevance of the sensitivity of the mechanical properties of planar, preloaded multi-layered solids undergoing shear to the performance of the wound roll damping concept. The experimentally measured shear capacity and stiffness vary more significantly with the preload than the number of layers. As such, the remainder of this work will investigate the frictional contact behavior between singular interfaces.

E.4   Interface Friction Behavior Characterization During Slip

The remainder of the experiments are focused on characterizing the friction behavior of singular interfaces during slip. The previous multi-layer experiments indicated that the shear capacity prior to macro slip is linear with preload. This suggests that testing at a single preload value is sufficient, and in this case, the maximum preload setting is chosen. For these experiments, all layer samples are removed, and the only interface is between the pneumatic contact surfaces and the shear platen, which as previously stated are both covered with Kapton to ensure a Kapton-Kapton interface similar to that of the vibration experiment (Fig. E.5).

In these experiments, the goal is to study in greater detail how the friction forces change after the previously identified macro slip occurs and to allow the slip to continue for a longer duration to observe variations. The aim is to determine whether the frictional behavior is more complex than what traditional Coulomb friction, which assumes a constant friction coefficient, can explain.

Initial Attempt Using Rate and State Framework: Step velocity Loading

There is a substantial body of work measuring and describing laboratory-derived friction laws and among these, "rate and state" (RAS) is a widely studied model [55]. Rate and state is a theoretical framework used to describe the behavior of frictional interfaces, whose popularity stems from its ability to describe experimentally measured frictional behavior under varying conditions, particularly in geological contexts such as earthquake mechanics. This framework describes how the friction forces between two surfaces depends on the slip rate and the history or "state" of the contact surfaces, which can change over time, even for constant sliding rates. Depending on the treatment, the state of the contact interface is considered as a proxy for the evolution of factors such as the contact area, macroscopic surface roughness, or microscopic asperities over a characteristic length scale. This model has been shown to be relevant not only for geological materials but also for plastics [106].

An initial attempt was made to determine whether the RAS model could accurately describe the friction behavior between Kapton. The RAS friction law provides a statement of the dynamic friction as a function of the sliding velocity V, and state θ, relative to a reference velocity V_R, the coefficient of friction at that steady reference velocity μ_R, and characteristic length scale D_R, with empirically derived constants

a and *b*, given by:

$$\mu = \mu_R + a \ln\left(\frac{V}{V_R}\right) + b \ln\left(\frac{V_R\theta}{D_R}\right) \tag{E.4}$$

The state variable θ has time dependent behavior, typically referred to as the "state evolution law", that has several model forms based on different experimental observations, but is commonly described by an exponentially decaying behavior [54, 115]. The state evolution law typically assumes a form where, for steady state sliding, $\frac{d\theta}{dt} = 0$ results in $\frac{V_R\theta}{D_R} = 1$. This results in the second term in Eq. E.4 being eliminated, allowing the empirical constants *a* and *b* to be decoupled and determined through fitting experimental data.

Step velocity profiles, alternating between steady sliding at two velocities through step changes, are commonly used in experiments for measuring rate and state friction, since they offer a controlled method to observe changes in frictional resistance following abrupt changes in sliding velocity (Fig. E.11).
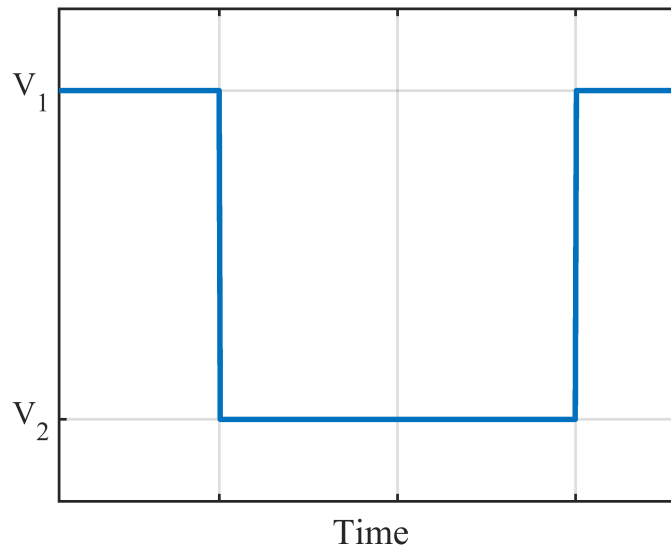
Figure E.11: Step velocity profile use to measure dynamic friction.

Fig. E.12 depicts the notional expected friction response with slip distance *y* when an interface that exhibits RAS behavior is subject to step velocity loading. The empirical constants are determined relative to the difference in the measured response between steady sliding sections.
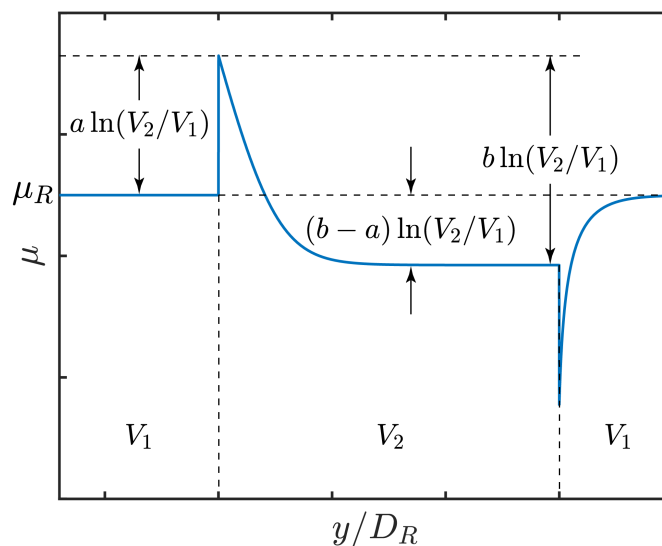
Figure E.12: Notional expected dynamic friction RAS response to step velocity profile at two steady state velocities V_1 and V_2. Relative magnitudes of measured friction coefficient between steady sliding sections used to determine the values of constants a and b.

Using this framework, a series of tests were conducted on the DDS tester with step velocity profiles, employing a range of velocities from $0.1 - 100$ µm/s, to determine whether RAS is a suitable model for describing measured friction behavior between Kapton-Kapton interface. In accordance with the typical conventions, the velocities of the step profile, (V_1, V_2), are paired such that $V_2 = 10V_1$ and velocity changes are made every 0.5 mm until the shear platen slips 3 mm in total. The force measured from the Instron is converted to friction assuming prior to the onset of slip, the normal preload can be related to the friction force according to the Coulomb Friction model (Fig. E.13):

$$\mu = \frac{F_c}{2F_N} \tag{E.5}$$
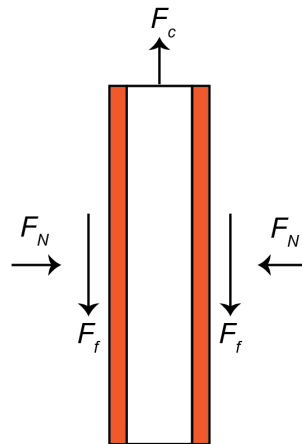
Figure E.13: Double direct shear free body diagram for single interface.

In examining the experimentally measured behaviors, it was observed that and not all behaviors matched the expected notional profile depicted in Fig. E.12. To determine whether this was possibly an effect of loading rate, an additional set of experiments was conducted by repeatedly running trials using the same step profile to assess consistency. These trials were conducted in batches of three, with the fixture reset by unloading and reloading the preload between each batch. Similar stochastic variation in responses was observed, indicating that the variability behavior was not solely determined by loading rate variation.

Fig. E.14 illustrates three distinct classifications of behaviors observed in this dataset. The behavior up to approximately 0.5 mm of slip is relatively consistent across all tests and is believed to originate from the test apparatus, such as the fixture and actuator. Therefore, this portion of the data is ignored. After 0.5 mm, the measured friction forces across all tests exhibit periodicity and relative consistency, indicating that both the steady-state and transient responses are stable. Within a given batch, the experiments demonstrated excellent run-to-run consistency, however the response is necessarily consistent from batch to batch after the fixture is reset.

In order to attempt to identify these behaviors, the RAS model was re-evaluated for different combinations of constants a and b to assess the sensitivity of the model to different terms in Eq. E.4. Fig. E.15 shows the variation in responses for alternating constants set to zero. Comparing Fig.E.14 and Fig.E.15 highlights the stochastic nature of friction, where the observed experimental behaviors encompassing all theoretical behaviors.
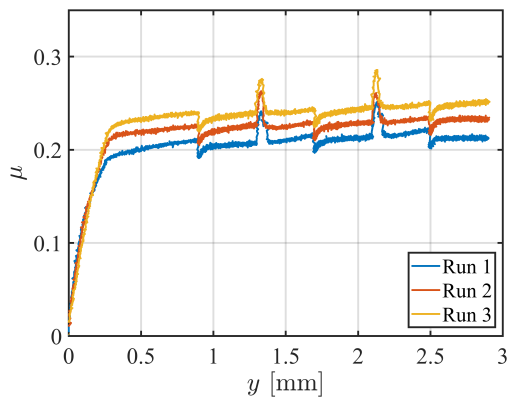
(a) Behavior 1
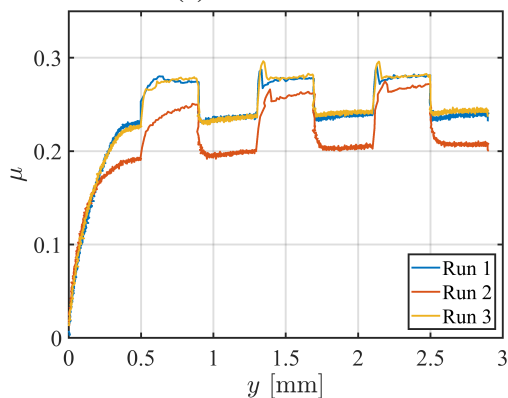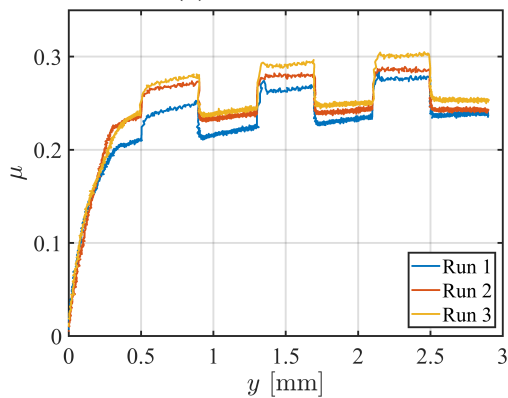
(a) $a \neq 0, b \neq 0$
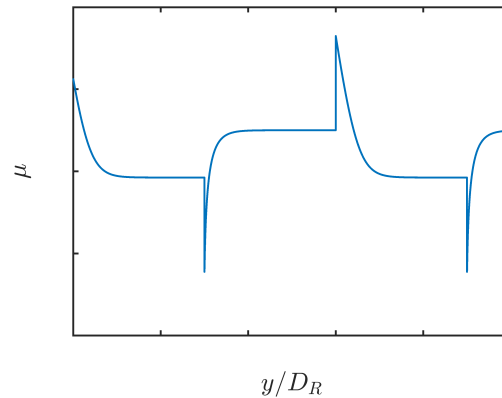
(b) Behavior 2
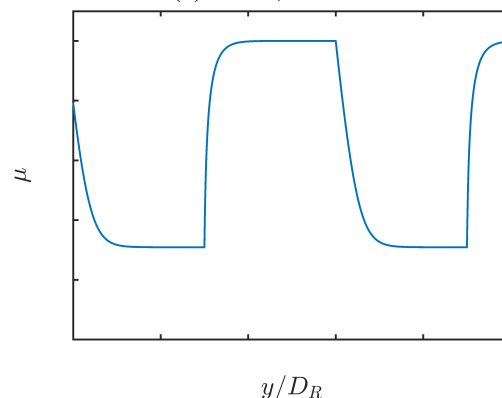
(b) $a = 0, b \neq 0$
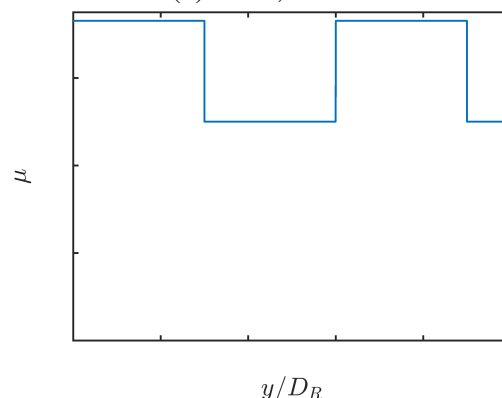
(c) Behavior 3

(c) $a \neq 0, b = 0$

Figure E.14: Example variation in experimental friction behavior response for identical experiment parameters.

Figure E.15: RAS model variation in response for different combinations of constants a and b.

The experiment results indicates that the RAS model provides an appropriate description of the measured friction behavior, but the stochastic nature of the experiment responses makes fitting a single model and translating it into simulation challenging. Given this difficulty, a qualitative evaluation of the experimental trends

was performed to assess sensitivity and impact of the observed friction behaviors.

Several observations can be made from the data in Fig. E.14. First, while the coefficient of friction does show rate dependence, the variation is relatively minor where the coefficient of friction remains well bounded between $\mu \in (0.1, 0.35)$ through all experiments with a large subset of the data clustering around the range $\mu \in (0.2, 0.3)$. Second, in general, the transient response due to state evolution decays very rapidly over very short distances, as evident by the transitions between steady state sliding. Consequently, the impact on frictional energy dissipation is minimal. This fact is evident in Fig. E.16, which plots the measured force vs. time from one experiment with a particularly exaggerated transient response, along with the estimated friction energy dissipated, E_F, calculated via:

$$E_F = \int F_c dy \tag{E.6}$$

Despite the initial overshoot in measured force during the velocity step transition, the transient response is unnoticeable in the cumulative energy dissipation plot because the force decays to the steady sliding response over a very short distance.
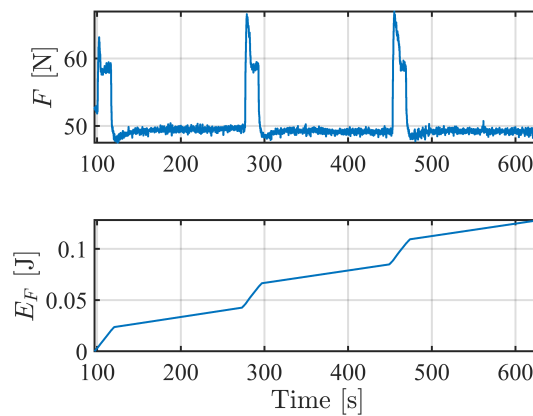
Figure E.16: Measured shear force during experiment plotted with estimated frictional energy dissipation. Despite large force transient, the effect is unnoticeable in estimated friction work done due to short active distance.

These results diminish the significance of state and time-dependent effects, while placing greater emphasis on rate dependence. Hence, the friction estimates from the steady sliding segments are isolated and depicted in Fig. E.17. Note that the error bars in the figure signify the cumulative variability observed across repeated step velocity tests, as well as tests with a shared velocity set point (Ex: Step velocity tests (V_1, V_2) at (0.1,1) and (1,10) μ m/s have a common slip rate set point at 1 μm/s).
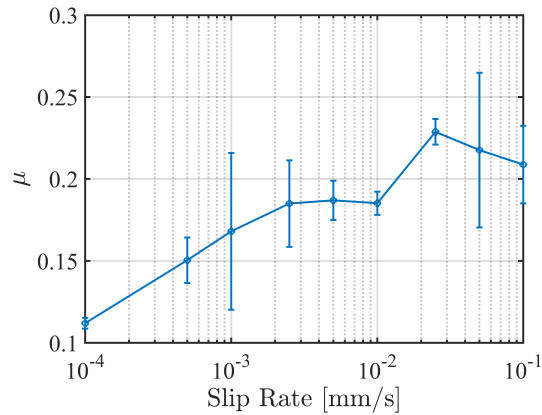
Figure E.17: Estimated coefficient of friction as a function of slip rate.

The measurements presented thus far were obtained under relatively slow sliding velocities (0.1 – 100 µm/s). The Instron 5569 can reach speeds of up to approximately 8 m/s, however, a noticeable deterioration in data quality was observed when attempting higher velocities with step velocity profiles. Fig. E.18 illustrates this effect, displaying data from two distinct step velocity profiles that share a common velocity set point at 0.5 mm/s. Apart from failing to align with any anticipated friction profiles, there is also a noticeable increased discrepancy in the measured behavior for identical sliding velocities when the loading profile involves higher velocities than presented in Fig. E.18.
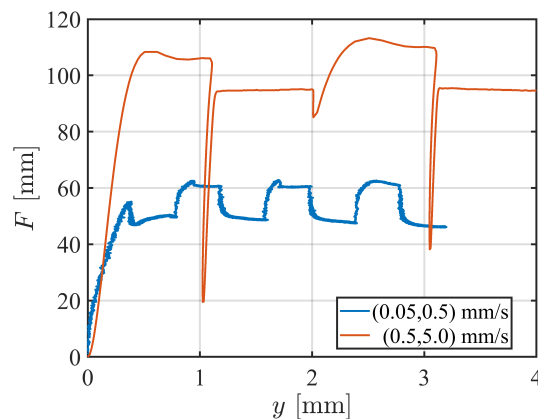
Figure E.18: Comparison in data quality between step velocity profiles using Instron 5569 testing machine. Despite sharing a common velocity set point, the measured forces deviate significantly.

Rate dependence investigation

Constant Velocity Loading

From the current set of experimental results, there are indications of rate-dependence in the friction behavior of a Kapton-Kapton slipping interface. However, there are issues when attempting to obtain consistent results from step velocity profiles at higher loading rates. The challenge lies in discerning whether these disparities originate from shortcomings in the physical experiment setup, the inherent non-smoothness of the step velocity loading profile, or if the measured responses reflect genuine phenomena arising from the complex and stochastic nature of contact. Considering the friction behavior's relative insensitivity to state, the focus of this work shifts from the RAS description towards investigating its rate dependence. Given that the most significant data was obtained from the steady sliding sections of the step velocity profiles, a logical next step is to directly test steady sliding for constant velocity loading. This simpler profile eliminates the multiple sharp transitions found in the discontinuous step velocity profile in order to help determine whether sliding rate uniquely defines the coefficient of friction at the interface of interest.

The previous experiment was repeated with a constant velocity ranging from 0.001 to 8 mm/s, overlapping with the range tested in the step velocity profile. Using a single, constant velocity enables testing at significantly higher velocities while maintaining good measurement quality. Fig. E.19 shows the constant velocity data using three trials for each test plotted together with the previous step velocity data.
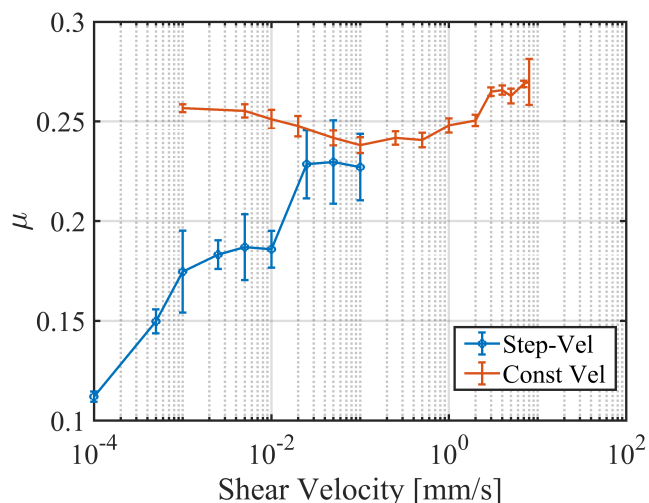
Figure E.19: Variation in friction with loading rate obtained with step velocity and constant velocity loading profiles. Friction appears approximately velocity independent when measured with constant velocity loading.

The friction measurement appears to be approximately rate-independent when loaded under constant velocity, indicating that the step velocity test profile potentially does influence the friction response.

Sinusoidal Loading

In light of the potential profile dependence noted, it is significant to highlight that none of the tested loading profiles thus far necessarily correspond to the loading conditions of wound roll vibration investigated experimentally in this research. During the experimental interlayer slip measurements conducted with the roll subjected to a sine dwell at its resonant frequency, the tracking targets exhibited periodic sinusoidal motion with an amplitude of approximately 0.02 mm. At the roll's resonant frequency of around 140 Hz, this corresponds to a velocity of roughly 20 mm/s. Because this velocity exceeds the capability of the Instron, the test setup was transferred to the Electroforce DMA.

While the Electroforce is nominally capable of excitations up to 300 Hz, it is subject to additional limitations that reduce capability. First, the Electroforce actuator is actively controlled and the closed-loop controller becomes unstable at low amplitudes, which sets a lower limit on the permissible profile amplitudes (Fig. E.20). Second, the maximum load rating for the Electroforce load cell is 225 N. This limit can easily be exceeded during high-frequency, displacement-controlled excitation due to the mass of the shear platen alone, even before considering the additional

forces required to induce slip against the clamping force from the symmetric DDS normal preload.

Given these constraints, these two constraints, it was not possible to reliably perform displacement-controlled sinusoidal loading that matches the experimentally measured profile. During initial testing and fixture bring up, a limited subset of high-frequency data was obtained, and some of this data is presented. However, controller instabilities during displacement control against high clamping preloads led to damage in multiple load cells, ultimately requiring the cessation of any further high-frequency tests. As a workaround, the desired velocity amplitude is approximated by operating at lower frequencies to stay within the load cell's force limit, while using higher amplitudes to prevent controller instability.

(a) Stable Electroforce test run. (b) Unstable Electroforce test run.
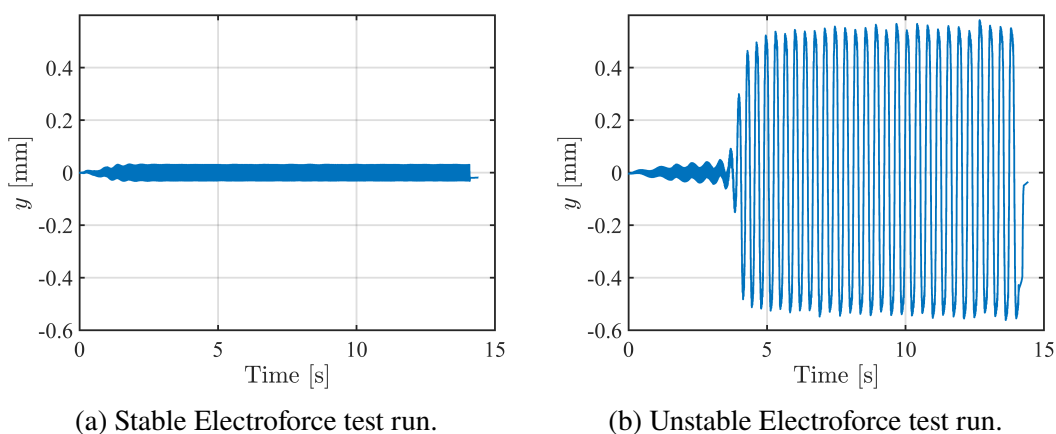
Figure E.20: Stable vs. unstable Electroforce test runs. Commanded profile: 0.03 mm amplitude sinusoidal loading at 140 Hz. A stable displacement controlled, run matching the commanded profile, was achieved in 1 out of 20 attempts.

Using the Electroforce, two sets of sinusoidal loading profiles were conducted. The first method employed force-controlled loading to demonstrate the evolution of hysteretic force-displacement behavior in friction from loading which produces minimal-to-no slip to levels where full macro-scale slip is observed. The second profile used displacement-controlled loading with large enough extents to guarantee smooth, periodic motion with sections of full slip conditions.

Fig. E.21 illustrates force-displacement data obtained using force-controlled loading, where the force set point was incrementally increased between experiments. Each figure contains the results of three trial runs for every loading profile.During cyclic loading aimed at friction dissipation, the force-displacement relationship is expected to produce hysteresis loops, allowing estimation of the energy dissipated

as heat from the enclosed area within the loop. For sufficiently low forcing, the force-displacement curve is approximately linear with virtually no dissipation, suggesting nearly fully recoverable displacement (Fig. E.21a and Fig. E.21b). As the forcing increases, the hysteresis loop becomes more pronounced, accompanied by a corresponding increase in loop area (Fig. E.21c and Fig. E.21d). The shape of the hysteresis displays an approximately smooth response, devoid of sharp transitions, unlike the exact Coulomb Friction model. These measurements offer further validation for the Coulomb friction approximations employed in simulations, such as the penalty and smoothed models, extending beyond considerations of computational efficiency.

(a) Force set point 1

(b) Force set point 2

(c) Force set point 3

(d) Force setpoint 4
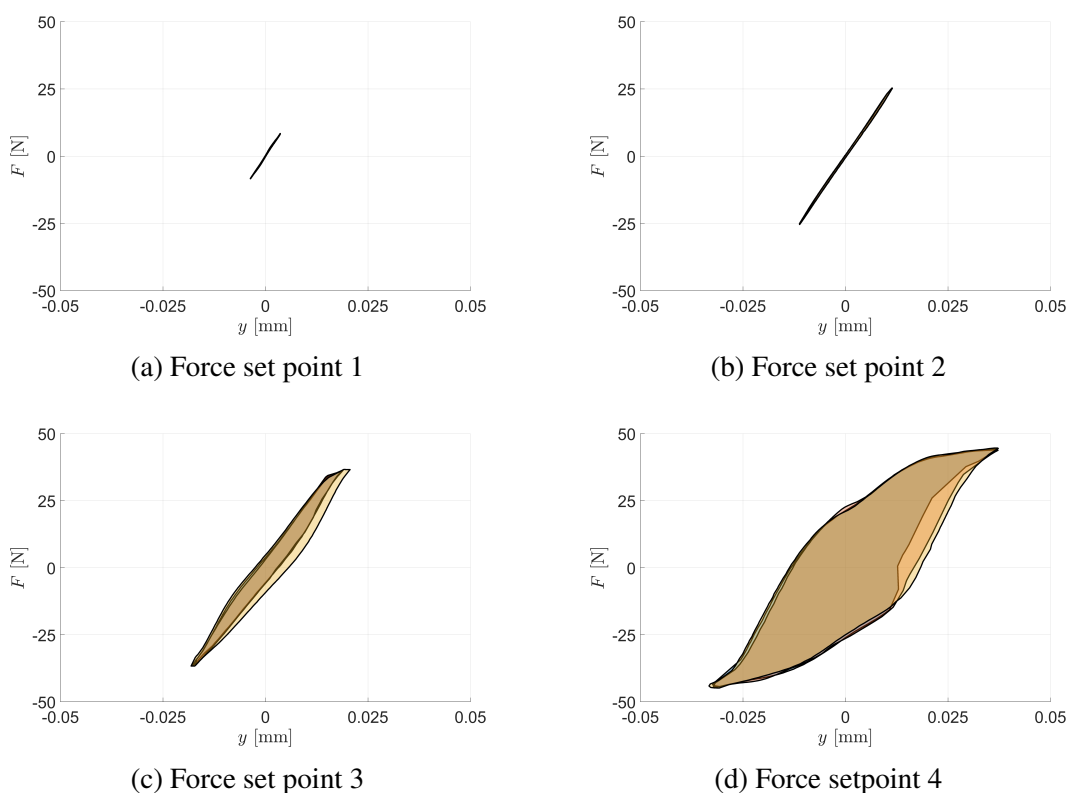
Figure E.21: Force control sinusoidal loading. Loading amplitude increases from set point 1 to 4. Hysteresis area increases with loading amplitude.

To showcase the hysteresis behavior for conditions with pronounced slip, the experiment was repeated with displacement control with significantly larger displacement amplitudes. Fig. E.22 shows the measured hysteresis for displacement-control profiles with varying normal preloads. A notable characteristic of the behaviors in these plot is the presence of longer segments of significant displacements at approximately constant, limiting force, which is the maximum recorded force in each

experiment. This suggests an overall Coulomb-like hysteresis behavior, where the constant force slipping sections are occurring at the maximum force the frictional interface can support, which is the shear capacity. Similar to the shear capacity trend observed previously, the variation in shear capacity with normal preload estimated from sinusoidal loading is observed to follow a linear trend (Fig. E.23). Therefore, testing at a single preload value is deemed adequate for gauging the rate dependence of friction through sinusoidal loading.

(a) $\sigma_N = 60$ kPa

(b) $\sigma_N = 80$ kPa

(c) $\sigma_N = 110$ kPa

(d) $\sigma_N = 140$ kPa
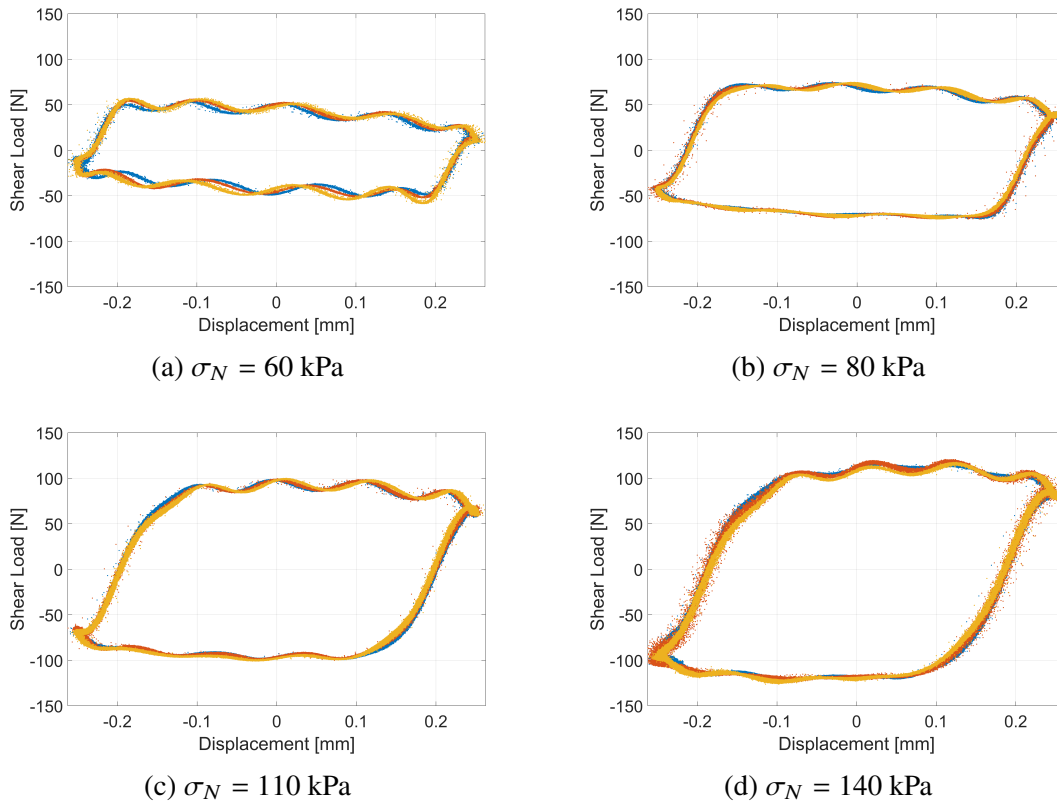
Figure E.22: Subset of displacement control sinusoidal loading at 0.25 mm amplitude showing variation in hysteresis area with applied normal preload.
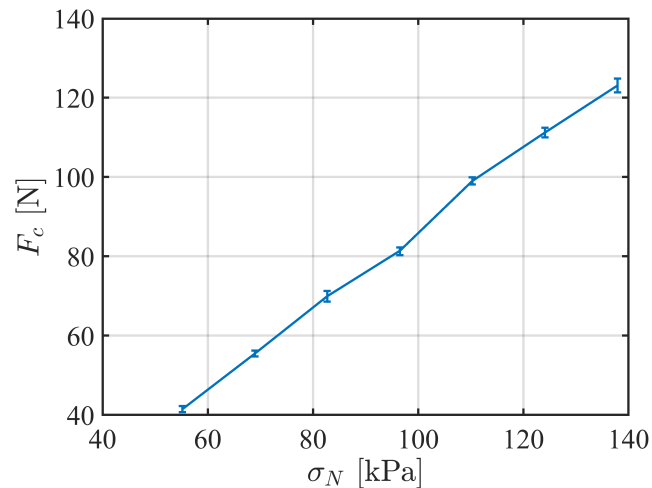
Figure E.23: Shear capacity vs. applied preload for sinusoidal loading. Shear capacity linearly increases with preload.

To explore the influence of loading rate on Kapton-Kapton friction using sinusoidal loading, a displacement-controlled profile was adopted, incorporating a maximum loading amplitude of 0.1 mm and excitation frequencies of up to 25 Hz. Fig. E.24 plot the sinusoidal data with the previous friction data obtained with the alternate loading profiles considered in this work.
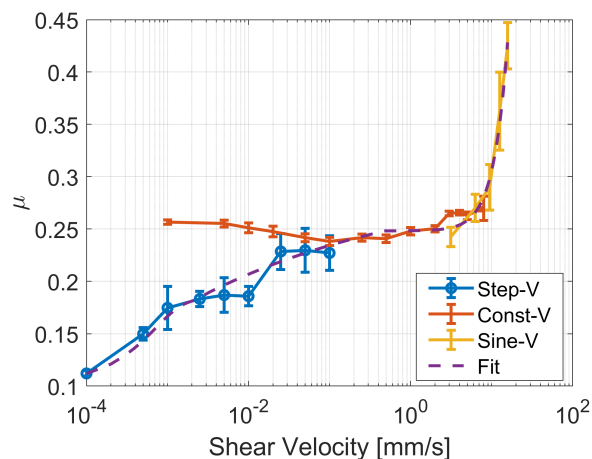
Figure E.24: Variation in friction with loading rate obtained with, step velocity, constant velocity, and sinusoidal loading profiles.

The velocities encountered by the interface during the sinusoidal loading profiles considered are observed to overlap with the velocity range covered by the constant velocity data. In the overlap region, the sinusoidal testing reports similar coefficient

of friction values ($\mu \approx 0.25$). At higher velocities beyond this range, the coefficient of friction exhibits an increase with shear rate.

E.5 Sensitivity of Wound Roll Vibration Simulations to Experimentally Measured Rate Dependent Friction

The primary objective of these experimental measurements was to obtain friction behavior data for Kapton-Kapton interfaces that could be used to define the contact behavior in simulations, in order to correlate the FEA model of the wound roll damper with experimentally measured wound roll vibration responses. Based on this data, two friction models were selected for testing. The first model, with constant friction at $\mu = 0.25$, was chosen because the constant velocity results indicated relevancy over a wide velocity range. The second model, with rate-dependent friction following the fit shown in Fig. E.24, was selected because it encompassed the measurements from all loading profiles tested. These friction models were used in the FEA simulations of the wound roll subjected to sine sweeps. Ultimately, there was no significant difference in the responses between the two models and the simulation results using either model demonstrated good correlation with the wound roll vibration experiment measurements (Fig. E.25). This suggests that the simple constant friction model was sufficient to describe the contact behavior, indicating that the response is insensitive to loading rate in this context. Therefore, the simulations in this study employ the penalty approximation to the Coulomb model, using $\mu = 0.25$ for the lab-scale simulations.

(a) FEA simulated frequency responses with constant friction model.

(b) FEA simulated frequency responses with rate-dependent friction model.

Figure E.25: Comparison between simulated and experimentally measured frequency responses for different friction models. Preload increases from blue to red.

E.6 Conclusion

In this chapter, experiments were performed to directly measure the mechanical properties of prestressed layered Kapton, encompassing measurements of shear stiffness, shear capacity, and friction under varying conditions such as preload, layer count, an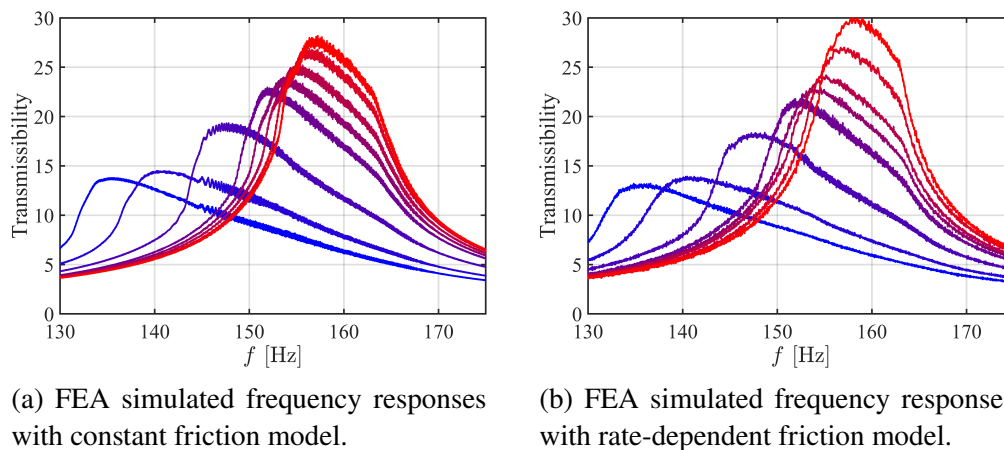d loading rates, along with analyses of hysteresis behavior. Various loading profiles including step-velocity, constant velocity, and sinusoidal velocity were employed to investigate these properties. The results indicated that while friction models such as rate and state may be appropriate for describing the complex behavior of interface contact, in this application, friction was observed to be more sensitivity to loading rate effect than state or length scale dependent effects.

Continued investigation on the sensitivity to slip rate revealed diverse friction behaviors with shear velocity across different velocity profiles. Constant velocity loading resulted in approximately constant coefficient of friction across a wide slip rate range. Aside from a limited region where the tested shear rates overlap, and the different profiles report friction values similar to the constant velocity results, step velocity testing below this range shows decreasing friction with decreasing velocity, while sine velocity testing above this range shows increasing friction with increasing velocity.

Although significant variations with loading rate were observed, attempts to develop a complex rate-dependent model did not yield substantial improvements when utilizing these models in contact definitions to correlate FEA simulations of wound roll vibration to experimental measurements over a simple constant friction model. This work justifies use of the Coulomb model as a reasonable framework for describing the friction for wound roll vibration.

Beyond providing justification for friction models used to achieve correlation, it's difficult to make any conclusive statements on frictional behavior due to a number of caveats. First, there are uncertainties regarding the influence of testing machine on results due to factors such as mechanical stiffness and the presence of active feedback control for the Electroforce in particular. Furthermore, the uniform pressure exerted by the pneumatic cylinders in the case of planar layered solids may not accurately reflect the stress distribution induced by winding in a wound roll, complicating the direct extension of findings from planar samples to wound roll geometries. Finally, the generalizability of these findings remains uncertain, requiring caution in extending claims beyond the confines of this experimental setup and its specific contact surfaces. Regardless, the outcomes of this investigation are included to

provide justification and enhance understanding and are not necessary to prove the fundamental efficacy of the wound roll damping concept.

BIBLIOGRAPHY

[1]   O. H. Amman, T. Von Kármán, and G. B Woodruff. "The failure of the Tacoma Narrows bridge". In: (1941).

[2]   A. Jenkins. "Self-oscillation". In: *Physics Reports* 525.2 (2013), pp. 167–222.

[3]   A. Larsen. "Aerodynamics of the Tacoma Narrows Bridge - 60 Years Later". In: *Structural Engineering International* 10.4 (2000), pp. 243–248. DOI: `10.2749/101686600780481356`. eprint: `https://doi.org/10.2749/101686600780481356`. URL: `https://doi.org/10.2749/101686600780481356`.

[4]   Air Accident Investigation Branch, Department of Transport. *Report on the accident to Boeing 737 400 G-OMBE near Kegworth, Leicester on 8th January 1989*. Tech. rep. London: HMSO, 1990.

[5]   NASA. *Galileo Jupiter Arrival Press Kit*. NASA Press Kit. Dec. 1995.

[6]   A. Albee et al. "Report on the loss of the Mars Polar Lander and Deep Space 2 missions". In: (2000).

[7]   Indian Space Research Organisation. *ISRO SSLV Mission Summary*. 2022. URL: `https://www.isro.gov.in/mission_SSLV_D1_summary_D2.html`.

[8]   J. J. Wijker. "Spacecraft Design Loads". In: *Spacecraft Structures* (2008), pp. 27–69.

[9]   G.S. Aglietti, G. Richardson, and P. Quill. "Launch Environment". In: *Encyclopedia of Aerospace Engineering*. Part 27. Vol. 6. John Wiley & Sons, 2010. Chap. 281. ISBN: 978-0-470-075440-05.

[10]   A. R. Timmins and R. E. Heuser. *A study of first-day space malfunctions*. Tech. rep. 1971.

[11]   C. Johnson and P. Wilke. "Protecting satellites from the dynamics of the launch environment". In: *AIAA Space 2003 Conference & Exposition*. 2003, p. 6266.

[12]   V. L. Pisacane. "Spacecraft Systems Design and Engineering". In: *Encyclopedia of Physical Science and Technology (Third Edition)*. Ed. by R. A. Meyers. Third Edition. New York: Academic Press, 2003, pp. 463–483. ISBN: 978-0-12-227410-7. DOI: `https://doi.org/10.1016/B0-12-227410-5/00888-7`. URL: `https://www.sciencedirect.com/science/article/pii/B0122274105008887`.

[13]   H. Frahm. *Device for damping vibrations of bodies, US Pat. No 989,958*. 1911.

[14] Y. Fujino et al. "Tuned Liquid Damper (TLD) for Suppressing Horizontal Motion of Structures". In: *Journal of Engineering Mechanics* 118.10 (1992), pp. 2017–2030. DOI: `10.1061/(ASCE)0733-9399(1992)118:10(2017)`.

[15] K. Chen, G. Tsampras, and Kyoungyeon Lee. "Structural connection with predetermined discrete variable friction forces". In: *Resilient Cities and Structures* 2.1 (2023), pp. 1–17.

[16] Y. Wei. *Deployable Piezoelectric Thin Shell Structures: Concepts, Characterization and Vibration Control*. California Institute of Technology, 2019.

[17] L. Foucault. *Démonstration physique du mouvement de rotation de la terre au moyen du pendule*. Editions de la librairie encyclopédique, 1951.

[18] W. Liu, G. R. Tomlinson, and J. A. Rongong. "The dynamic characterisation of disk geometry particle dampers". In: *Journal of Sound and Vibration* 280.3 (2005), pp. 849–861. ISSN: 0022-460X. DOI: `https://doi.org/10.1016/j.jsv.2003.12.047`. URL: `https://www.sciencedirect.com/science/article/pii/S0022460X04001282`.

[19] A. Kareem. *Tuned Liquid Dampers (TLDs) and Tuned Liquid Column Dampers (TLCDs) Research at NatHaz Modeling Laboratory*. URL: `https://www3.nd.edu/~nathaz/research/liquid/liq_damp.html`.

[20] T. G. Ivanco. *Compact vibration damper*. US Patent 8,672,107. 2014.

[21] D. J. Wagg. "A review of the mechanical inerter: historical context, physical realisations and nonlinear applications". In: *Nonlinear Dynamics* 104.1 (2021), pp. 13–34.

[22] N. W. Hagood and A. Von Flotow. "Damping of structural vibrations with piezoelectric materials and passive electrical networks". In: *Journal of Sound and Vibration* 146.2 (1991), pp. 243–268.

[23] J. Ormondroyd and J.P. Den Hartog. "The theory of the dynamic vibration absorber". In: *Journal of Fluids Engineering* 49.2 (1928).

[24] Alessandro Stabile et al. "A 2-collinear-DoF strut with embedded negative-resistance electromagnetic shunt dampers for spacecraft micro-vibration". In: *Smart Materials and Structures* 26.4 (2017), p. 045031.

[25] A. M. Kaynia, D. Veneziano, and J. M. Biggs. "Seismic effectiveness of tuned mass dampers". In: *Journal of the Structural Division* 107.8 (1981), pp. 1465–1484.

[26] J. Connor and S. Laflamme. "Tuned mass damper systems". In: *Structural Motion Engineering* (2014), pp. 199–278.

[27] E. Schnitzer. *Band-pass Shock and Vibration Absorbers for Application to Aircraft Landing Gear*. 3803. National Advisory Committee for Aeronautics, 1956.

[28]   A. R. Klembczyk and M. W. Mosher. "Applications of Hermetically Sealed Fluid Dampers for Low Level, Wide Bandwidth Vibration Isolation". In: *Proceedings of the 69thShock and Vibration Symposium*. 1998.

[29]   G. Housner et al. "Structural control: past, present, and future". In: *Journal of engineering mechanics* 123.9 (1997), pp. 897–971.

[30]   J. Banik and P. Hausgen. "Roll-Out Solar Arrays (ROSA): Next Generation Flexible Solar Array Technology". In: AIAA SPACE, Astronautics Forum, and Exposition. 2017. DOI: `10.2514/6.2017-5307`. eprint: `https://arc.aiaa.org/doi/pdf/10.2514/6.2017-5307`. URL: `https://arc.aiaa.org/doi/abs/10.2514/6.2017-5307`.

[31]   D. Webb et al. "Advances in starshade technology readiness for an exoplanet characterizing science mission in the 2020's". In: *Advances in Optical and Mechanical Technologies for Telescopes and Instrumentation II*. Ed. by Navarro, R. and Burge, J. H. Vol. 9912. Society of Photo-Optical Instrumentation Engineers (SPIE) Conference Series. July 2016, 99126H, 99126H. DOI: `10.1117/12.2232587`.

[32]   B.S. Gaudi et al. "The Habitable Exoplanet Observatory (HabEx) mission concept study final report". In: *arXiv preprint arXiv:2001.06683* (2020).

[33]   M. Arya, N. Lee, and S. Pellegrino. "Ultralight Structures for Space Solar Power Satellites". In: *3rd AIAA Spacecraft Structures Conference*. 2016. DOI: `10.2514/6.2016-1950`. eprint: `https://arc.aiaa.org/doi/pdf/10.2514/6.2016-1950`. URL: `https://arc.aiaa.org/doi/abs/10.2514/6.2016-1950`.

[34]   C. Lee. "Stresses and Defects in Roll Products: A Review of Stress Models and Control Techniques". In: *International Journal of Precision Engineering and Manufacturing* 19 (May 2018), pp. 781–789. DOI: `10.1007/s12541-018-0094-z`.

[35]   A. Pedivellano and S. Pellegrino. "Deployment dynamics of thin-shell space structures". In: *Journal of Spacecraft and Rockets* 59.4 (2022), pp. 1214–1227.

[36]   J. K. Good and N. Vaidyanathan. "Importance of torque capacity in predicting crepe wrinkles and starring in wound rolls". In: *International Conference on Web Handling*. 1995.

[37]   J. A. Umali, L. L. Wilson, and S. Pellegrino. "Vibration Response of Ultralight Coilable Spacecraft Structures". In: 4th AIAA Spacecraft Structures Conference. 2017. DOI: `10.2514/6.2017-1115`. eprint: `https://arc.aiaa.org/doi/pdf/10.2514/6.2017-1115`. URL: `https://arc.aiaa.org/doi/abs/10.2514/6.2017-1115`.

[38] C. Lee, H. Kang, and K. Shin. "Advanced taper tension method for the performance improvement of a roll-to-roll printing production line with a winding process". In: *International Journal of Mechanical Sciences* 59.1 (2012), pp. 61–72.

[39] S.J. Burns, R.R. Meehan, and J.C. Lambropoulos. "Strain-based formulas for stresses in profiled center-wound rolls". In: *Tappi journal* 82.7 (1999).

[40] S. Li and J. Cao. "A hybrid approach for quantifying the winding process and material effects on sheet coil deformation". In: *J. Eng. Mater. Technol.* 126.3 (2004), pp. 303–313.

[41] R. C. Benson. "A nonlinear wound roll model allowing for large deformation". In: (1995).

[42] Y. M. Lee and J. A. Wickert. "Stress field in finite width axisymmetric wound rolls". In: *J. Appl. Mech.* 69.2 (2002), pp. 130–138.

[43] J. Lee and C. Lee. "An advanced model for the numerical analysis of the radial stress in center-wound rolls". In: *International Journal of Mechanical Sciences* 105 (2016), pp. 360–368.

[44] H.C. Altmann. "Formulas for Computing Stresses in Center-Wound Rolls". In: *Tappi* 51.4 (1968), pp. 176–179.

[45] Z. Hakiel. "Nonlinear Model For Wound Roll Stresses". In: *Tappi journal* 70 (May 1987), pp. 113–117.

[46] C. Mollamahmutoglu et al. "Coupling of winding models and roll quality instruments". In: *Proceedings of the 13th International Conference on Web Handling*. Oklahoma State University, 2015.

[47] S. M. Hussain. "ROLL WINDING-CAUSES, EFFECTS AND CURES OF LOOSE CORES IN NEWSPRINT ROLLS." In: (1977).

[48] D. J. Pfeiffer. "Internal pressures in a wound roll". In: *Tappi Journal* 49.8 (1966), p. 342.

[49] D. R. Roisum. *The Mechanics of Winding*. TAPPI, 1994. ISBN: 9780898522815. URL: https://books.google.com/books?id=qjjYAAAACAAJ.

[50] P. Kaboré et al. "Modelling radial compressive modulus in wound rolls". In: *Measurement and Control* 40.7 (2007), pp. 207–210.

[51] J. D. Pfeiffer. "Compressive modulus measurement techniques". In: (1999).

[52] H. P. Yagoda. "Resolution of a core problem in wound rolls". In: (1980).

[53] R. A. Ibrahim. "Friction-induced vibration, chatter, squeal, and chaos—part I: mechanics of contact and friction". In: (1994).

[54] A. Ruina. "Slip instability and state variable friction laws". In: *Journal of Geophysical Research: Solid Earth* 88.B12 (1983), pp. 10359–10370.

[55] C. Marone. "Laboratory-derived friction laws and their application to seismic faulting". In: *Annual Review of Earth and Planetary Sciences* 26.1 (1998), pp. 643–696.

[56] G. Amontons. "De la résistance causée dans les machines, tant par les frottemens des parties qui les composent, que par la roideur des cordes qu'on y emploie, et la manière de calculer l'un et l'autre". In: *Mémoires de l'Académie Royale des Sciences* (1699). In Histoire de l'Académie Royale des Sciences, 1732, pp. 206–227.

[57] C.A. Coulomb. *Théorie des machines simples, en ayant égard de leurs parties et de la roideur des cordages*. 1st. Vol. X. 5 folded engraved plates. Paris: Moutard, Panckoucke, 1785, pp. 131–332.

[58] E. Gdoutos et al. "Development of the Deployable on-Orbit ultraLight Composite Experiment (DOLCE) for the Space Solar Power Project Demonstration Mission". In: *AIAA SCITECH 2022 Forum*. 2022, p. 1266.

[59] *DuPont™ Kapton® Summary of Properties*. Internal Document. DuPont, Wilmington, DE. 2022.

[60] J. K. Good and D. R. Roisum. *Winding: Machines, Mechanics and Measurements*. TAPPI Press, 2008. ISBN: 9781932078695. URL: `https://books.google.com/books?id=mg0Sdg8dCJwC`.

[61] W.Y. Chang, T.H. Fang, and Y.C. Lin. "Physical characteristics of polyimide films for flexible sensors". In: *Applied Physics A* 92 (2008), pp. 693–701.

[62] *The Properties of Polyimide Targets*. Tech. rep. 92. DOE/SF/19460-465. Univ. of Rochester, NY (United States). Lab. for Laser Energetics, 2002.

[63] W. He et al. "Study on Young's modulus of thin films on Kapton by microtensile testing combined with dual DIC system". In: *Surface and Coatings Technology* 308 (2016), pp. 273–279.

[64] J. Lee and C. Lee. "An advanced model for the numerical analysis of the radial stress in center-wound rolls". In: *International Journal of Mechanical Sciences* 105 (2016), pp. 360–368. ISSN: 0020-7403. DOI: `https://doi.org/10.1016/j.ijmecsci.2015.11.016`. URL: `http://www.sciencedirect.com/science/article/pii/S0020740315003938`.

[65] Tekscan. *FlexiForce Integration Guides: Best Practices in Electrical Integration*. 2020.

[66] J. Lollock. "The effect of swept sinusoidal excitation on the response of a single-degree-of-freedom oscillator". In: *43rd AIAA/ASME/ASCE/AHS/ASC Structures, Structural Dynamics, and Materials Conference*. 2002, p. 1230.

[67] N. Roy, M. Violin, and E. Cavro. "Sine sweep effect on specimen modal parameters characterization". In: *Advances in aircraft and spacecraft science* 5.2 (2018), p. 187.

[68] A. Akay. "Acoustics of friction". In: *The Journal of the Acoustical Society of America* 111.4 (2002), pp. 1525–1548.

[69] P. Torvik. "On estimating system damping from frequency response bandwidths". In: *Journal of Sound and Vibration - J SOUND VIB* 330 (Dec. 2011), pp. 6088–6097. DOI: `10.1016/j.jsv.2011.06.027`.

[70] S Ali Ashrafi and Andrew W Smyth. "Generalized masing approach to modeling hysteretic deteriorating behavior". In: *Journal of engineering mechanics* 133.5 (2007), pp. 495–505.

[71] Jian Shi and Domniki Asimaki. "From stiffness to strength: Formulation and validation of a hybrid hyperbolic nonlinear soil model for site-response analyses". In: *Bulletin of the Seismological Society of America* 107.3 (2017), pp. 1336–1355.

[72] Danilo Capecchi and Gianmarco de Felice. "Hysteretic systems with internal variables". In: *Journal of engineering mechanics* 127.9 (2001), pp. 891–898.

[73] Wilfred D Iwan. "On a class of models for the yielding behavior of continuous and composite systems". In: (1967).

[74] J.P. Den Hartog. "LXXIII. Forced vibrations with combined viscous and coulomb damping". In: *The London, Edinburgh, and Dublin Philosophical Magazine and Journal of Science* 9.59 (1930), pp. 801–817.

[75] K. Im and J. P. Avouac. "Linear stability analysis of the condition for vibration during frictional slip". In: *Journal of the Mechanics and Physics of Solids* 167 (2022), p. 104993.

[76] L. Marino, A. Cicirello, and D. A. Hills. "Displacement transmissibility of a Coulomb friction oscillator subject to joined base-wall motion". In: *Nonlinear Dynamics* 98 (2019), pp. 2595–2612.

[77] R. A. Ibrahim. "Friction-induced vibration, chatter, squeal, and chaos—part II: dynamics and modeling". In: (1994).

[78] N. Makris and M. C. Constantinou. "Analysis of Motion Resisted by Friction. I. Constant Coulomb and Linear/Coulomb Friction". In: *Journal of Structural Mechanics* 19.4 (1991), pp. 477–500.

[79] C. Pierre, A. A. Ferri, and E. H. Dowell. "Multi-harmonic analysis of dry friction damped systems using an incremental harmonic balance method". In: (1985).

[80] B. Feeny et al. "A historical review on dry friction and stick-slip phenomena". In: (1998).

[81] E. Pennestrì et al. "Review and comparison of dry friction force models". In: *Nonlinear dynamics* 83 (2016), pp. 1785–1801.

[82] R.I. Leine et al. "Stick-slip vibrations induced by alternate friction models". In: *Nonlinear dynamics* 16 (1998), pp. 41–54.

[83] T.C. Kim, T.E. Rook, and R. Singh. "Effect of smoothening functions on the frequency response of an oscillator with clearance non-linearity". In: *Journal of Sound and Vibration* 263.3 (2003), pp. 665–678.

[84] T.T. Tay, I. Mareels, and J.B. Moore. *High performance control*. Springer Science & Business Media, 2012.

[85] MathWorks. *MATLAB Parallel Computing Toolbox*. Version 9.8.0.1323502 (R2020a). MathWorks, Inc. Natick, MA, 2020.

[86] T. Glassman et al. "Starshade scaling relations". In: *Proc SPIE* 7440 (Aug. 2009). DOI: `10.1117/12.825033`.

[87] D. Webb et al. "Starshade technology development activity Milestone 6A: Verify petal shape on-orbit stability". In: *Jet Propulsion Laboratory Publications* (2021).

[88] B. R. Spence et al. "International space station (ISS) roll-out solar array (ROSA) spaceflight experiment mission and results". In: *2018 IEEE 7th World conference on photovoltaic energy conversion (WCPEC)(a Joint Conference of 45th IEEE PVSC, 28th PVSEC & 34th EU PVSEC)*. IEEE. 2018, pp. 3522–3529.

[89] M. K. Chamberlain, S. H. Kiefer, and J. Banik. "On-orbit structural dynamics performance of the roll-out solar array". In: *2018 AIAA Spacecraft Structures Conference*. 2018, p. 1942.

[90] M. Arya et al. "Demonstration of deployment accuracy of the starshade inner disk subsystem". In: *AIAA Scitech 2020 Forum*. 2020, p. 1670.

[91] N.J. Kasdin et al. "Technology demonstration of starshade manufacturing for NASA's Exoplanet mission program". In: *Space Telescopes and Instrumentation 2012: Optical, Infrared, and Millimeter Wave*. Vol. 8442. SPIE. 2012, pp. 132–147.

[92] E. R. Schwanbeck. "Advanced Solar Arrays on the ISS". In: *Association of Space Explorers (ASE) Planetary Congress 2019*. JSC-E-DAA-TN74083. 2019.

[93] Space Exploration Technologies Corp. (SpaceX). *SpaceX Falcon User's Guide*. Hawthorne, CA: Space Exploration Technologies Corp., 2023.

[94] Tom Irvine. "EQUIVALENT STATIC LOADS FOR SINE VIBRATION". In: (2006). PDF, Available at: vibrationdata.com.

[95] T. Irvine. "Damping properties of materials". In: *Magnesium* 5000.3100 (2004), pp. 10–14.

[96] G. E. Maddux et al. "Stress analysis manual". In: *Dayton: Technology Incorporated* (1969).

[97]   A. Hajimiri. *Analog: Inexact Science, Vibrant Art*. Preprint (pdf). 2023. URL: `https://chic.caltech.edu/wp-content/uploads/2023/01/Hajimiri_Analog_DRAFT012023.pdf`.

[98]   Eleftherios Gdoutos et al. "Ultralight deployable space structure prototype". In: *AIAA Scitech 2020 Forum*. 2020, p. 0692.

[99]   M. Smith. *ABAQUS/Standard User's Manual, Version 6.9*. English. United States: Dassault Systèmes Simulia Corp, 2009.

[100]   Dassault Systèmes Simulia Corp. *Abaqus User Manual: Implicit dynamic analysis using direct integration*. 2022. URL: `https://docs.software.vt.edu/abaqusv2022/English/SIMACAEANLRefMap/simaanl-c-dynamic.htm`.

[101]   H. M. Hilber, T. J. R. Hughes, and R. L. Taylor. "Improved Numerical Dissipation for Time Integration Algorithms in Structural Dynamics". In: *Earthquake Engineering and Structural Dynamics* 5 (1977), pp. 283–292.

[102]   M. J. Casiano. *Extracting Damping Ratio from Dynamic Data and Numerical Solutions*. Technical Memorandum. Huntsville, AL, United States: NASA Marshall Space Flight Center, Sept. 2016.

[103]   Samuel Poincloux et al. "Bending response of a book with internal friction". In: *Physical Review Letters* 126.21 (2021), p. 218004.

[104]   AT Mathis, Adam Ray Brink, and D Dane Quinn. *Implementation and Comparison of Advanced Friction Representations within Finite Element Models*. Tech. rep. Sandia National Lab.(SNL-NM), Albuquerque, NM (United States), 2018.

[105]   Péter Korondi. *Robot Application*. Apr. 2014. ISBN: 9789633131367.

[106]   J. H. Dieterich and B. D. Kilgore. "Direct observation of frictional contacts: New insights for state-dependent properties". In: *Pure and Applied Geophysics* 143 (1994), pp. 283–302.

[107]   SW Shaw. "On the dynamic response of a system with dry friction". In: *Journal of Sound and Vibration* 108.2 (1986), pp. 305–325.

[108]   James H Dieterich. "Modeling of rock friction: 1. Experimental results and constitutive equations". In: *Journal of Geophysical Research: Solid Earth* 84.B5 (1979), pp. 2161–2168.

[109]   M.Z. Chen et al. "The missing mechanical circuit element". In: *IEEE Circuits and Systems Magazine* 9.1 (2009), pp. 10–26. DOI: `10.1109/MCAS.2008.931738`.

[110]   Tristan Baumberger and Christiane Caroli. "Solid friction from stick–slip down to pinning and aging". In: *Advances in Physics* 55.3-4 (2006), pp. 279–348.

[111]   James R Rice, Nadia Lapusta, and K Ranjith. "Rate and state dependent friction and the stability of sliding between elastically deformable solids". In: *Journal of the Mechanics and Physics of Solids* 49.9 (2001), pp. 1865–1898.

[112]   Avraham Harnoy, Bernard Friedland, and Simon Cohn. "Modeling and measuring friction effects". In: *IEEE Control Systems Magazine* 28.6 (2008), pp. 82–91.

[113]   Pierre E Dupont and Eric P Dunlap. "Friction modeling and control in boundary lubrication". In: *1993 American Control Conference*. IEEE. 1993, pp. 1910–1915.

[114]   ASTM International. "Standard Test Method for Shear Modulus at Room Temperature". In: *ASTM E143-20* (2020).

[115]   James H Dieterich. "Time-dependent friction and the mechanics of stick-slip". In: *Pure and applied geophysics* 116 (1978), pp. 790–806.